

© 2016 Tan Huu Nguyen

COMPUTATIONAL PHASE IMAGING FOR
BIOMEDICAL APPLICATIONS

BY

TAN HUU NGUYEN

DISSERTATION

Submitted in partial fulfillment of the requirements
for the degree of Doctor of Philosophy in Electrical and Computer Engineering
in the Graduate College of the
University of Illinois at Urbana-Champaign, 2016

Urbana, Illinois

Doctoral Committee:

Associate Professor Gabriel Popescu, Chair
Professor Minh N. Do
Professor David Alexander Forsyth
Professor André Alexander Kajdacsy-Balla, University of Illinois at Chicago

ABSTRACT

When a sample is illuminated by an imaging field, its fingerprints are left on the *amplitude* and the *phase* of the emerging wave. Capturing the information of the wavefront grants us a deeper understanding of the optical properties of the sample, and of the light-matter interaction. While the amplitude information has been intensively studied, the use of the phase information has been less common. Because all detectors are sensitive to intensity, not phase, wavefront measurements are significantly more challenging. Deploying optical interferometry to measure phase through phase-intensity conversion, quantitative phase imaging (QPI) has recently gained tremendous success in material and life sciences.

The first topic of this dissertation describes our effort to develop a new QPI setup, named transmission Spatial Light Interference Microscopy (tSLIM), that uses the twisted nematic liquid-crystal (TNLC) modulators. Compared to the established SLIM technique, tSLIM is much less expensive to build than its predecessor (SLIM) while maintaining significant performance. The tSLIM system uses parallel aligned liquid-crystal (PANLC) modulators, has a slightly smaller signal-to-noise Ratio (SNR), and a more complicated model for the image formation. However, such complexity is well addressed by computing. Most importantly, tSLIM uses TNLC modulators that are popular in display LCDs. Therefore, the total cost of the system is significantly reduced.

Alongside developing new imaging modalities, we also improved current QPI imaging systems. In practice, an incident field to the sample is rarely perfectly spatially coherent, i.e., plane wave. It is generally partially coherent; i.e., it comprises of many incoherent plane waves coming from multiple directions. This illumination yields artifacts in the phase measurement results, e.g., *halo* and *phase-underestimation*. One solution is using a very bright source, e.g., a laser, which can be spatially filtered very well. However, the laser comes at the expense of speckles, which degrades image quality. Therefore, solutions purely based on physical

modeling and computations to remove these artifacts, using white-light illumination, are highly desirable. Here, using physical optics, we develop a theoretical model that accurately explains the effects of partial coherence on image information and phase information. The model is further combined with numerical processing to suppress the artifacts, and recover the correct phase information.

The third topic is devoted to applying QPI to clinical applications. Traditionally, stained tissues are used in prostate cancer diagnosis instead. The reason is that tissue samples used in diagnosis are nearly transparent under bright field inspection if unstained. Contrast-enhanced microscopy techniques, e.g., phase contrast microscopy (PC) and differential interference contrast microscopy (DIC), can render visibility of the untagged samples with high throughput. However, since these methods are intensity-based, the contrast of acquired images varies significantly from one imaging facility to another, preventing them from being used in diagnosis. Inheriting the merits of PC, SLIM produces phase maps, which measure the refractive index of label-free samples. However, the maps measured by SLIM are not affected by variation in imaging conditions, e.g., illumination, magnification, etc., allowing consistent imaging results when using SLIM across different clinical institutions. Here, we combine SLIM images with machine learning for automatic diagnosis results for prostate cancer. We focus on two diagnosis problems of automatic Gleason grading and cancer vs. non-cancer diagnosis.

Finally, we introduce a new imaging modality, named Gradient Light Interference Microscopy (GLIM), which is able to image through optically thick samples using low spatial coherence illumination. The key benefit of GLIM comes from a large numerical aperture of the condenser, which is 0.55 NA, about five times higher than that in SLIM. GLIM has an excellent depth sectioning when recording three-dimensional information of the susceptibility of the sample. We also introduce a model for the image formation of GLIM with an implication

that a simple filtering step in the transverse dimension can dramatically improve the sectioning in the axial dimension. With GLIM, one can measure accurately the surface area, volume, and dry mass of a variety of biological samples, ranging from cells that are about tens of microns thick to bovine embryos that are hundreds of microns thick.

To my Parents and my Wife

ACKNOWLEDGMENTS

I would like to express my deep gratitude to my Ph.D. dissertation adviser, Prof. Gabriel Popescu, head of the Quantitative Light Imaging (QLI) lab. He has been very supportive to me over my doctoral study with his careful guidance, insightful comments, and high expectations. I would have never been able to finish the degree without his dedicated support.

I would like to thank my Ph.D. co-adviser, Prof. Minh N. Do, who has been continuously supporting me from the first day I came to the United States for graduate study. He has given me valuable feedback and helped me tackle several challenges in my research. I owe an important debt to Minh for all of his generous support and his expectations.

I would like to acknowledge our collaborators, Dr. Andre Balla and Dr. Virgilia Macias, for their awesome tutorials and tremendous support when we were working on the automatic diagnosis problem of prostate cancer. I also learned from Dr. Tyler Ralston from Butterfly Network Inc., Dr. Catalin Chiritescu from Phi Optics Inc., and Mr. Nathan Ukrainetz from Microsoft on how to be efficient and professional in industry environments.

My appreciation goes to all members of the QLI lab. Mikhail Kandel has been working with me during many late nights on novel ideas despite his tightly packed schedule. Dr. Shamira Sridharan has always been supportive and careful in correcting my English typos. She has been a very good trainer to me on several biology materials, which I had a hard time to understand. I also enjoyed the fun time in the lab with Dr. Taewoo Kim, Hassaan Majeed, Dr. Hoa Pham, Dr. Ru Wang and Dr. Mustafa Mir. I also learned a lot from my colleagues in the Computational Imaging group, led by Prof. Minh Do, including Dr. Huy Bui, Trong Nguyen, Greg Meyer, Benjamin Chidester, and Dr. Andre Targino through fruitful conversations and their problem-solving skills.

My greatest appreciation goes to my mother. She overworked in most of her lifetime as a single mother to raise me up and give me the best possible education within her ability. Without her effort, I would have ended up as somebody completely different. My wife, Trang Vu, has been an excellent chef, saved me from most of the housework, and gave me strong encouragement during the final stage of the degree.

Finally, I would like to acknowledge funding agencies for my research, including Agilent, NSF, NIH, and EBICS. I also thank the ECE and CSE departments for their generous departmental fellowships.

TABLE OF CONTENTS

LIST OF ABBREVIATIONS.....	x
CHAPTER 1: INTRODUCTION	1
1.1 MICROSCOPY	1
1.2 QUANTITATIVE PHASE IMAGING (QPI)	3
1.3 APPLICATIONS OF QPI.....	6
1.3.1 <i>Biomedical research</i>	6
1.3.2 <i>Material sciences</i>	6
1.3.3 <i>Clinical applications</i>	7
1.3.4 <i>Tomography</i>	7
1.4 THESIS OVERVIEW.....	7
CHAPTER 2: TSLIM: DESIGN AND IMPLEMENTATION.....	9
2.1 INTRODUCTION	9
2.2 PRINCIPLE OF SLIM.....	9
2.3 OPTICAL SETUP	11
2.4 RESULTS.....	12
CHAPTER 3: QPI WITH PARTIALLY COHERENT ILLUMINATION.....	16
3.1 IMAGE FORMATION	16
3.1.1 <i>Traditional interferometry</i>	18
3.1.2 <i>Common-path interferometry</i>	18
3.2 THREE-DIMENSIONAL PARTIALLY COHERENT QPI	20
3.3 HALO AND PHASE UNDERESTIMATION ARTIFACTS.....	21
3.3.1 <i>2D case</i>	21
3.3.2 <i>Halos in 3D imaging</i>	24
3.4 SUMMARY	29
CHAPTER 4: HALO-FREE PHASE CONTRAST MICROSCOPY.....	30
4.1 INTRODUCTION	30
4.2 BACKGROUND	30
4.3 OPTICAL SETUP	33
4.4 IMAGE FORMATION AND THE HALO ARTIFACT.....	34
4.5 INVERSE PROBLEM	37
4.6 RECONSTRUCT HRPC IMAGES FROM THE INVERSED PHASE.....	37
4.7 RESULTS.....	38
4.7.1 <i>hrPC imaging of neurons</i>	38
4.7.2 <i>Thickness measurements of nanoscale topography samples</i>	39
4.7.3 <i>hfPC of biological samples</i>	41
4.7.4 <i>hfQPI imaging of cell populations</i>	42
4.7.5 <i>Cell growth study using QPI</i>	43
4.8 SUMMARY	47
CHAPTER 5: PROSTATE CANCER DIAGNOSIS USING QPI.....	49
5.1 INTRODUCTION	49
5.2 TISSUE MICRO ARRAY (TMA) DESCRIPTION	53
5.3 AUTOMATIC DIAGNOSIS FRAMEWORK	54
5.3.1 <i>Feature extraction from phase images</i>	56
5.3.2 <i>Random forest for automatic segmentation</i>	57
5.4 AUTOMATIC GLEASON GRADING.....	60
5.5 CANCER VS. NON-CANCER CLASSIFICATION	63

5.6	SUMMARY	68
CHAPTER 6: GRADIENT LIGHT INTERFERENCE MICROSCOPY (GLIM).....		69
6.1	INTRODUCTION	69
6.2	OPTICAL SETUP AND IMAGING PRINCIPLE	72
6.3	QPI USING GLIM.....	74
6.4	SINGLE CELL TOMOGRAPHY USING GLIM	74
6.5	GLIM FOR EMBRYO TOMOGRAPHY.....	77
6.6	SUMMARY	79
CHAPTER 7: CONCLUSION		81
APPENDIX A: SUPPLEMENTAL INFORMATION FOR CHAPTER 3.....		83
A.1	EXTRACTING THE CROSS-CORRELATION FUNCTION FROM INTERFERENCE FRINGES.....	83
A.2	CONVERGENCE OF THE 3D IDEAL PHASE TO 2D IDEAL PHASE.....	83
A.3	DERIVATION FOR THE FORMULA OF THE 3D MEASURED PHASE.....	84
A.4	DERIVATION FOR THE EXPRESSION OF $\Gamma_{i,io}$	85
A.5	DERIVATION FOR THE EXPRESSION OF $\Gamma_{s,io}$	85
A.6	DERIVATION FOR THE EXPRESSION OF $\Gamma_{i,so}$	86
APPENDIX B: SUPPLEMENTAL INFORMATION FOR CHAPTER 4.....		88
B.1	CHARACTERIZING THE FUNCTIONS $\Gamma_i, h_o,$ AND h_s	88
B.2	EXTRACTING FOUR TERMS OF EQ. (4.1)	89
B.3	PROOF OF EQ. (4.2).....	91
B.4	SOLVING FOR THE OPTIMAL PHASE OF INTEREST	92
B.5	HALO-REMOVAL PERFORMANCE EVALUATION.....	93
B.6	PERFORMANCE COMPARISON BETWEEN QPI, TQPI AND HFQPI	94
B.7	AUTOMATIC CELL SEGMENTATION FOR 20X HeLa CELL IMAGES.....	95
APPENDIX C: SUPPLEMENTAL INFORMATION FOR CHAPTER 5.....		97
C.1	TRAINING THE TEXTON DICTIONARY	97
C.2	RANDOM FOREST CLASSIFIER FOR PIXEL CLASSIFICATION	98
C.3	POST-PROCESSING OF THE SEGMENTATION RESULTS.....	100
C.4	GLM NET FOR BASAL VS. NON-BASAL CLASSIFICATION	101
C.5	FEATURES FOR GLEASON GRADE 3 VS. GLEASON GRADE 4 CLASSIFICATION	105
APPENDIX D: SUPPLEMENTAL INFORMATION FOR CHAPTER 6.....		107
D.1	EXTRACTING PHASE GRADIENT FROM INTENSITY IMAGE	107
D.2	SLM CALIBRATION PROCEDURE	107
D.3	2D IMAGE FORMATION IN GLIM	109
D.4	3D IMAGE FORMATION IN GLIM	110
D.5	DEPTH SECTIONING IMPROVEMENT OF GLIM WITH SPATIAL FILTERING.....	114
D.6	3D AUTOMATIC SEGMENTATION OF THE HeLa CELL WITH GLIM.....	116
D.7	DRYMASS MEASUREMENT USING GLIM	117
D.8	TIME-LAPSE MEASURING RESULTS FOR DRY MASS, SURFACE AREA, VOLUME AND SPHERICITY OF HeLa CELLS.....	118
REFERENCES.....		121

LIST OF ABBREVIATIONS

1D, 2D, 3D	one, two, three dimensional
BF	bright field
BPH	benign prostatic hyperplasia
CCD	charge-coupled device
CPCTR	co-operative prostate cancer tissue resource
CUDA	computed unified device architecture
DHM	digital holographic microscopy
DIC	differential interference contrast
DPM	diffraction phase microscopy
DM	dry mass
DMD	dry mass density
DRIMAPS	digitally recorded interference microscopy with automatic phase shifting
FLD	Fisher linear discriminant
FOV	field of view
FPM	Fourier phase microscopy
GLIM	Gradient Light Interference Microscopy
H&E	hematoxylin and eosin
HGPIN	high-grade prostatic intraepithelial neoplasia
HPM	Hilbert phase microscopy
hfPC	halo-free phase contrast
hfSLIM	halo-free spatial light interference microscopy

OPL	optical path length
OQM	optical quadrature microscopy
OTF	optical transfer function
PA-LC	parallel aligned-liquid crystal
PC	phase contrast
pcQPI	partially coherent quantitative phase imaging
PSF	point spread function
QPI	quantitative phase imaging
QWLSI	quadriwave lateral shearing interferometry
RBC	red blood cell
RF	random forest
ROI	region of interest
SLIM	spatial light interference microscopy
SLM	spatial light modulator
SNR	signal-to-noise ratio
SVM	support vector machine
tSLIM	thresholded Spatial Light Interference Microscopy
TMA	tissue micro-array
TNLC	twisted nematic liquid-crystal
tQPI	thresholded quantitative phase imaging
tSLIM	transmission Spatial Light Interference Microscopy
WDT	white-light diffraction tomography

CHAPTER 1: INTRODUCTION

1.1 Microscopy

Starting as a cloth merchant at the age of 16, Antonie van Leeuwenhoek (1632-1723), a Dutch lens maker also known as “the Father of Microbiology”, nurtured his passion for grinding and polishing lenses with the first objective of identifying thread counts. Quickly afterward, he built a microscope with magnification far exceeding other competitors available at the time [1]. His curiosity also made him the first person in history to discover a whole new world of existing microscopic lives. Leeuwenhoek used his miniature microscope to look at bacteria, spermatozoa etc., and wrote letters to the Royal Society to describe his observations [2]. These letters marked a new area of microbiology study and modern microscopy. However, the optical resolution of a microscope, the smallest observable size of an object, was not well understood until more than one hundred years after, when Ernst Abbe (1840-1905), a German physicist, published a paper establishing the resolution limit in 1873 [3]. Alongside resolution, *contrast* is also a major challenge in the development of early microscopy. Many living cells are optically thin and transparent, essentially “phase objects”. Low absorbance makes them barely detectable to the conventional microscopy inspection (for example, see Figure 1.1(a)).

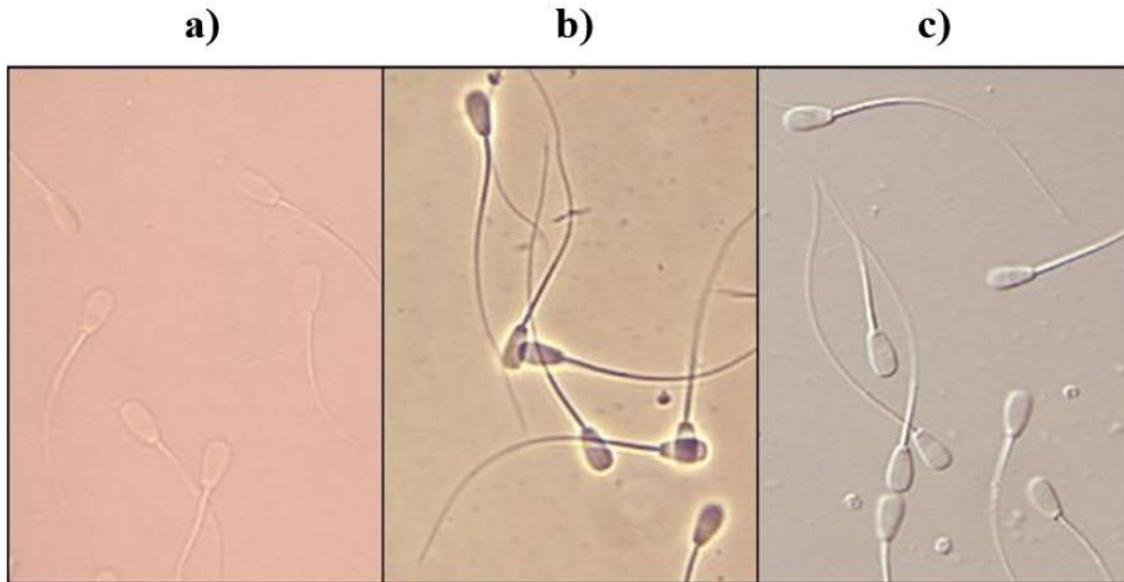


Figure 1.1 Imaging sperms under different microscopy modalities. (a) BF microscopy. (b) PC microscopy. (c) DIC microscopy. (Adapted from:

<http://www.vivo.colostate.edu/hbooks/pathphys/reprod/semeneval/motility.html>).

Understanding this phenomenon, a Dutch physicist named F. Zernike (1888-1966) invented the first phase contrast microscope [4], which maps minute phase shifts into intensity modulations, measurable to optical detectors such as human eyes and cameras (for example, see Figure 1.1(b)). Zernike understood that the total field emanating from the sample consists of two components: a strong incident field and a much weaker field shifted by a quarter of a wavelength. To maximize the interference contrast, he proposed a modification in the optical setup to attenuate the strong incident field, and further retard or advance it by another quarter wavelength. This change makes the two fields oscillate either in-phase or out-of-phase, rendering the maximum contrast on the interference image. The invention earned Zernike a Nobel prize in physics in 1953. Other contrast-enhanced microscopy techniques were also introduced including the DIC microscopy [5], first invented by David Smith in 1955. The contrast in DIC is sensitive to the directional gradient of the phase instead of the phase itself. The key benefit of DIC compared to PC is the ability to use spatially incoherent illumination,

allowing it to have higher resolution and better depth sectioning. Although these methods represent significant advancements in microscopy, their outputs are still qualitative.

1.2 Quantitative phase imaging (QPI)

In 1948, Dennis Gabor (1900-1979), a Hungarian-British physicist, introduced *holography*, a process in which the sample field from an object is recorded on a holographic plate [6]. Such recording allowed reconstruction of an unreal image of an object without its physical presence. However, holography did not gain much attention at the time due to a lack of coherent light sources. Thanks to the introduction of lasers as new prominent sources, holography gained more popularity after 1960 [7]. Advancements in digital image sensors and digital holography allowed recording holograms on the charged-coupled devices (CCDs), instead of the photorefractive materials, and reconstructing the wavefronts with high quality. Later on, scientific-grade CCDs and complementary metal-oxide-semiconductor (CMOS) sensors become widely available at reasonable prices. These factors converted holography into an emerging field, quantitative phase imaging (QPI) [8]. At the moment, QPI has become a popular tool in biomedical research including mass transport [9, 10], cell growth [11, 12], cell structures and dynamics [13, 14], tomography [15, 16], and topography [17]. It has also been recently expanded to clinical applications [18, 19] and material sciences [8, 20].

When light travels through phase objects such as cells or tissues, its wavefront is deformed due to variation in the optical path length. The amount of deformation depends on the refractive index of the samples compared to that of the surrounding medium. More specifically, the quantity of interest QPI is the phase, $\phi(\mathbf{r}_\perp)$, defined as $\phi(\mathbf{r}_\perp) = \beta_o \Delta n(\mathbf{r}_\perp) h(\mathbf{r}_\perp)$. Here, β_o is the central wavenumber of the illumination, $\Delta n(\mathbf{r}_\perp)$, and $h(\mathbf{r}_\perp)$ are the refractive index difference and the thickness sample, respectively. $\mathbf{r}_\perp = (x, y)$ is

the lateral coordinate of the location of interest in the field of view (FOV). For classification purposes, QPI can be divided into non-interferometer and interferometry groups.

The non-interferometer group needs only one intensity field to measure the phase. For example, the quadriwave lateral shearing interferometry (QWLSI) [21] method uses modified Hartmann masks [22] to convert local wavefront variations into local displacements of focal spots of micro-lenses, placed right before the imaging sensor. However, the effective resolution of QWLSI, which is physically constrained by the size of the microlens, is worse than the diffraction limit. Computation-based methods, such as the transport of intensity (TIE) [23, 24], use a relation between the phase and intensity of the sample field at each pixel. The relation allows extracting the Laplacian of the phase from intensity measurements using multiple images acquired at different axial depths, ultimately reducing the axial resolution of the system.

The interferometry group, on the other hand, requires two fields, a reference one, U_r , and an imaging one, U_t . The phase is extracted through their temporal cross-correlation function, evaluated over several optical cycles. There are several ways to partition methods in this group. The following classification criteria are used: traditional vs. common-path, off-axis vs. in-line, phase-shifting vs. single-shot, and white-light vs. laser illumination.

The first classifier relates to how the reference field is generated. In traditional interferometry, it is identical to the illumination field, carrying no sample information. Methods following this principle include digital holographic microscopy (DHM) [25-27], Hilbert phase microscopy [28], digitally recorded interference microscopy with automatic phase shifting (DRIMAPS) [29], and optical quadrature microscopy (OQM) [30], etc. Meanwhile, in the common-path group, the reference field is derived by spatially filtering the sample field. Examples of these methods include Fourier phase microscopy [31], spatial light interference microscopy (SLIM) [32, 33], and diffraction phase microscopy [20, 34], etc. Although

coherence artifacts, e.g. halo and phase underestimation, are less for traditional interferometry setups [35], they are often affected by mechanical vibration and ambient noise. Frequent calibration and laser illumination are also needed to maximize the contrast of the interference image. However, speckles from the laser significantly degrade the image quality [36]. Meanwhile, the common-path interferometry setups are extremely stable to ambient noise and mechanical vibration [20]. The geometry significantly simplifies the optical setup by eliminating extra stabilizing equipment. Also, white-light illumination [37] can be used to suppress the speckles to reach the optical diffraction limit and achieve high sensitivity. More importantly, common-path methods can be directly deployed to commercially available microscopes as add-on modules. Unfortunately, they are more sensitive to the spatial coherence of the illumination, which may result in halo artifacts [22, 38].

Phase-shifting interferometry, e.g. SLIM [32], FPM [14], combines different frames obtained from multiple *temporal* phase modulations, at least three frames, to produce a phase map. On the other hand, single-shot interferometry methods, e.g. DPM [20], HPM [28], provide a phase map directly from a single intensity image. Therefore, it is often used in studying high-speed dynamics at the cost of lower spatial resolution, compared to phase-shifting interferometry.

Most conventional DHM methods use off-axis illumination, causing a higher noise floor compared to that of on-axis geometries.

Another way to sort QPI systems is by using the figures of merit. Performance of a QPI system is characterized by four different factors: (a) acquisition rate, (b) transverse resolution (c) spatial phase sensitivity and (d) temporal phase sensitivity, see Chapter 2 in Ref. [8]. The fastest acquisition rate is given by single-shot methods [39], [40] with possible transverse resolution loss (from the theoretical limit). Phase-shifting methods [32, 33], in contrast, retain this limit at the cost of lower frame rate. However, even with phase-shifting method, the

theoretical resolution limit can hardly be achieved in practice due to speckle, as a result of high temporal coherence of laser illumination sources [36, 41]. Despite potentially being useful in some applications, speckle is a detrimental factor to the spatial phase sensitivity. Fortunately, white-light methods [34, 39, 42, 43] can remove these speckles almost completely due to an extremely short coherence length (typically in the order of 1 micron). Hence, spatial phase sensitivity is best with white-light methods. Finally, the temporal phase sensitivity attains its maximum performance with common-path methods [32, 37].

1.3 Applications of QPI

In recent years, QPI has emerged as a promising tool to several fields of study [10, 12, 18, 44-66]. Below are some examples.

1.3.1 Biomedical research

QPI methods were used to quantify cell growth [12], cell motility [44], dry mass [45, 46], response to drug delivery [47], red blood cell (RBC) dynamics [48-51, 67-71], blood testing [52, 53], metastatic cell studies [55], arthropod imaging [59], and detecting microorganisms in food [72]. Researchers have been using QPI to characterize neural network formation [10, 54], measure intracellular transport [10, 55, 56], investigate cytoskeleton dynamics [49, 57], and image cell structures [58]. Recently, it has been extended to imaging large samples, e.g., arthropods [59] and tissue [60].

1.3.2 Material sciences

Thanks to the high sensitivity to changes in the optical path length, QPI has also been used in material sciences to measure the axial expansion of the palladium micro-disks during hydrogen exposure [61], monitor photochemical etching [62] and semiconductor etching [63], study the evaporation processes of micro-droplets [64] and image fast moving air-water mixer flows

[73]. Combining with pattern recognition, Zhou et al. used QPI to detect wafer defects as small as 20 nm [65].

1.3.3 Clinical applications

Standard health care can benefit from the merits of QPI. In [18], Wang et al. reported for the first time, the use of the phase measured by QPI to classify benign vs. cancerous areas in a dataset of 11 prostate biopsies. Sridharan et al. proposed using QPI to improve the prediction of prostate cancer recurrence [19], [74]. Majeed et al. [66] found that breast cancer diagnosis results using QPI images have good agreement with those using H&E stained images.

1.3.4 Tomography

Recent advancements in QPI marked significant achievements in tomography when several groups extended QPI to fully reconstruct the three-dimensional (3D) susceptibility of the sample using deconvolution, e.g., [15, 43, 58]. Synthetic aperture imaging methods that combine multiple recordings at different incident angles were also introduced [75-77]. However, high computational complexity and strong storage demands are still major bottlenecks preventing these techniques from being widely applicable.

1.4 Thesis overview

The main topic of this dissertation is improving QPI using computational tools. We show how to use computational tools to extend capabilities of QPI into clinical applications. Chapter 2 covers the design and implementation of a transmission SLIM (tSLIM) system using the twisted nematic liquid-crystal (TNLC) spatial light modulator (SLM). tSLIM offers comparable image quality compared to the traditional SLIM. However, it is more cost-effective. Chapter 3 shows a detailed analysis of the effects of spatial coherence, both two-dimensional (2D) and 3D, to common-path QPI. We show that the partial coherence of the illumination causes both the halo artifact and the phase-underestimation to the phase

measurement. Based on this analysis, we propose a computational method to reverse these phenomena and recover the correct phase results in Chapter 4. We show that this correction can also be applied to phase-contrast (PC) to remove the halo artifact in the widely used PC microscopy. Chapter 5 demonstrates a combination between QPI and machine learning to obtain high throughput automatic diagnosis of prostate cancer. The framework is evaluated on a large dataset from a tissue micro array (TMA), consisting of more than 300 cores, one core per person. Chapter 6 shows our most recent work on developing a new microscopy technique, named Gradient Light Interference Microscopy (GLIM), an expansion of the differential interference contrast (DIC) microscopy. The key benefit of GLIM is an ability to use low spatially coherent light, allowing it to have excellent depth sectioning and transverse resolution, even for optically thick samples that are up to hundreds of microns thick. To obtain tomography information, we suggest a simple filtering method that is effective in both computational and storage costs. Chapter 7 concludes this dissertation with key contributions of these works.

CHAPTER 2: tSLIM: DESIGN AND IMPLEMENTATION

2.1 Introduction

The SLIM method, first introduced in [32], is a common-path, phase-shifting QPI method that uses white-light illumination to obtain speckle-free phase information with sub-nanometer noise level at optical diffraction resolution. SLIM possesses a depth-sectioning of about 1.2 microns thanks to an extremely short temporal coherence length of white light illumination. It also has an excellent temporal sensitivity due to common-path geometry. In contrast to the method of transport of intensity Equation (TIE) [23], SLIM has no assumption on the imaging field and has a better axial sectioning. From an application standpoint, many other QPI methods require dedicated microscopes while the SLIM system is an add-on module. The traditional SLIM system comes with a PAN-SLM with very high diffraction efficiency (more than 90%) that performs *phase-only* modulation. However, the high cost of these SLMs is the biggest bottleneck in popularizing the method. To alleviate this issue, we propose to use the TNLC-SLM as an alternative. In [33], we demonstrated a tSLIM system using a transmission TNLC-SLM (Holoeye Inc.) with competitive sensitivity. In the next section, we briefly recap the working principles of both SLIM methods with emphasis on the difference between the two systems. Interest readers are referred to [33] for more details.

2.2 Principle of SLIM

Both SLIM and transmission SLIM have the same principles. Consider a phase object with transmittance $T(\mathbf{r}_\perp) = \exp[i\phi(\mathbf{r}_\perp)]$, where \mathbf{r}_\perp is the coordinate of interest in the sample plane, and $\phi(\mathbf{r}_\perp)$ the quantity of interest. Under coherent illumination, the sample field at the output

port of the microscope relates to the transmittance as $U_p(\mathbf{r}_\perp) = cT(\mathbf{r}_\perp)$ for some constant c that depends on the amplitude of the incident. Because of this constant, the phase can be extracted up to an offset as $\phi(\mathbf{r}_\perp) = \arg[T(\mathbf{r}_\perp)]$. Unfortunately, direct intensity measurement only gives $I_p(\mathbf{r}_\perp) = |U_p(\mathbf{r}_\perp)|^2 = |c|^2$, not the phase of interest. To extract $\phi(\mathbf{r}_\perp)$, the SLIM method [32] decomposes U_p into a non-scattered component U_o and a scattered component U_s such that $U_p(\mathbf{r}_\perp) = U_o + U_s(\mathbf{r}_\perp) = U_o \left\{ 1 + \beta(\mathbf{r}_\perp) \exp[i\Delta\phi(\mathbf{r}_\perp)] \right\}$, where $\beta(\mathbf{r}_\perp) = |U_s(\mathbf{r}_\perp)|/|U_o|$, and $\Delta\phi(\mathbf{r}_\perp) = \arg[U_s(\mathbf{r}_\perp)] - \arg[U_o]$. Here, the plane wave U_o is obtained by spatially averaging $U_p(\mathbf{r}_\perp)$. Therefore, it does not vary as a function of the transverse coordinate \mathbf{r}_\perp . Given both $\beta(\mathbf{r}_\perp)$ and $\Delta\phi(\mathbf{r}_\perp)$, the phase of interest can be extracted as

$$\phi(\mathbf{r}_\perp) = \tan^{-1} \left(\frac{\beta(\mathbf{r}_\perp) \sin[\Delta\phi(\mathbf{r}_\perp)]}{1 + \beta(\mathbf{r}_\perp) \cos[\Delta\phi(\mathbf{r}_\perp)]} \right). \quad (2.1)$$

To solve $\beta(\mathbf{r}_\perp)$ and $\Delta\phi(\mathbf{r}_\perp)$, four combinations of U_o and $U_s(\mathbf{r}_\perp)$ are generated with recorded intensities for the interference. Let a_i be the relative weights of the two fields for the i^{th} combination. The corresponding intensity of the combined field is given by:

$$\begin{aligned} I(\mathbf{r}_\perp; a_i) &= |a_i U_o + U_s(\mathbf{r}_\perp)|^2 \\ &= |a_i|^2 |U_o|^2 + |U_s(\mathbf{r}_\perp)|^2 + a_i^* U_o^* U_s(\mathbf{r}_\perp) + a_i U_o U_s^*(\mathbf{r}_\perp), \end{aligned} \quad (2.2)$$

where $i = 1, 2, 3, 4$. Note that for each transverse coordinate \mathbf{r}_\perp , there are four linear equations provided by Eq. (2.2), enough to solve for four unknowns $|U_o|^2, |U_s|^2, U_o U_s^*, U_s U_o^*$. Using solutions of these unknowns, one can compute $\beta(\mathbf{r}_\perp) = \sqrt{|U_s(\mathbf{r}_\perp)|^2 / |U_o|^2}$,

$\Delta\phi(\mathbf{r}_\perp) = \arg[U_s(\mathbf{r}_\perp)U_o^*]$. These quantities are afterward substituted into Eq. (2.2) to compute $\phi(\mathbf{r}_\perp)$.

In SLIM, a PAN-SLM was used which generates four phase-only modulation $0, \pi/2, \pi,$ and $3\pi/2$, corresponding to $a_1 = 1, a_2 = i, a_3 = -1,$ and $a_4 = -i$. In tSLIM, the TNLC-SLM performs both phase-modulation and *amplitude-modulation*. Therefore, the quantities a_i 's are four different complex numbers, which can be determined using a calibration procedure described in [33].

2.3 Optical setup

Figure 2.1 shows the optical setup of the tSLIM system, which is similar to that of the SLIM except that the reflective PAN-SLM of SLIM is replaced by a transmission TNLC-SLM. First, the sample field U_p is relayed to the output port of a PC microscope. Then, the lens L_1 performs a spatial Fourier transform to generate \tilde{U}_p at its back focal plane. On this plane, \tilde{U}_p is split into two non-overlapping components, \tilde{U}_o and \tilde{U}_s . Here, \tilde{U}_o matches the phase ring of the objective and the phase annulus of the condenser. \tilde{U}_s covers the rest of the aperture of the objective, after excluding \tilde{U}_o . The TNLC-SLM generates a modulating ring matching this phase annulus, with a modulating coefficient of a_i on \tilde{U}_o . The second lens L_2 performs another Fourier transform on each field, and yields $a_i U_o + U_s$. The camera captures the intensity of this new total field as $I(\mathbf{r}_\perp; a_i) = |a_i U_o + U_s(\mathbf{r}_\perp)|^2$. To solve for the phase map $\phi(\mathbf{r}_\perp)$, one needs four intensity images corresponding to four coefficients a_i 's.

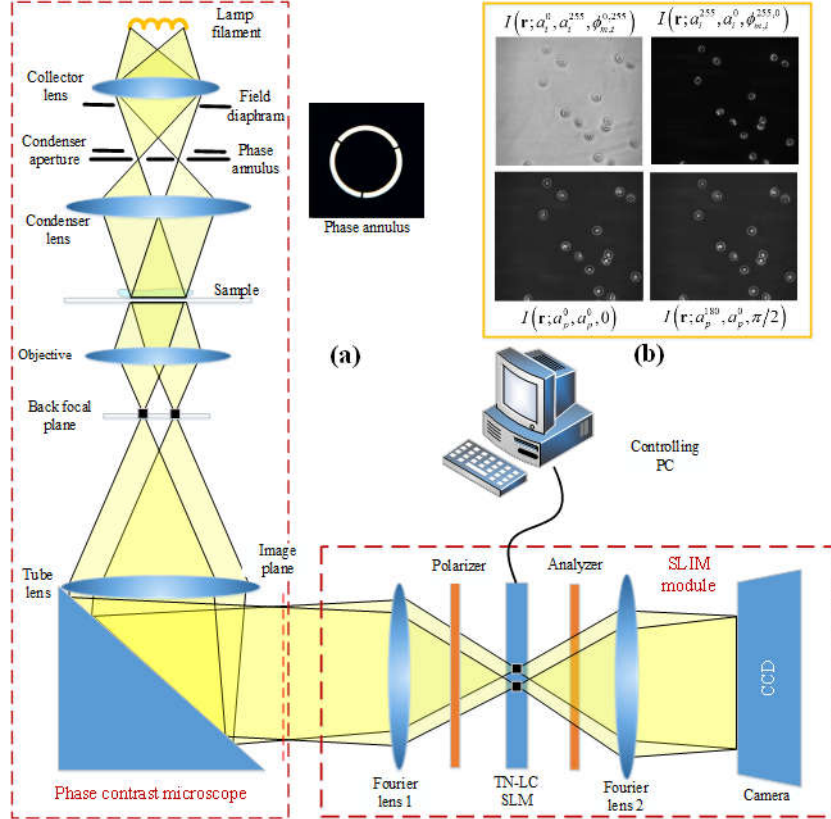


Figure 2.1 Optical setup of tSLIM. (a) The sample field from an inverted Nikon Ti-E microscope with a $40\times/0.95$ NA objective is spatially Fourier transformed by the Fourier lens L_1 onto the surface of a TNLC-SLM (LC 2002, Holoeye Inc.). This SLM introduces four different modulations to the Fourier transform, \tilde{U}_o and \tilde{U}_s . The Fourier lens L_2 performs an inverted Fourier transform on these fields so that they can interfere on the LCD. (b) Four recorded intensity frames at four different modulations. The field of view is approximately $200\times 200\mu\text{m}^2$.

2.4 Results

To determine the accuracy of our method, we image polystyrene spherical micro-beads (CAT #19814, Polysciences Inc.) with a diameter of $2\mu\text{m} \pm 5\%$ and a refractive index value of $n = 1.5962$, evaluated the central wavelength. The beads are suspended in immersion oil (Zeiss Inc.), $n = 1.518$. Figure 2.2(a) shows an image of two beads with a thickness cross-section displayed in Figure 2.2(b). Clearly, the maximum thickness measured is very close to the known diameter of the bead, which tells that tSLIM provides accurate thickness measurement. To quantify the spatial phase sensitivity of our

system, we image the optical path length variation of a background area, shown in Figure 2.2(c). The blue profile in Figure 2.2(d) shows a histogram of OPL variation over the FOV, with a standard deviation of $\sigma_s = 0.99$ nm, which is also the spatial sensitivity of the system. Another important characteristic of a QPI system is the temporal stability. To quantify this metric, a series of 284 frames of the background is recorded over 30 seconds. Next, a temporal average is subtracted to each frame to remove common mode noise [8]. An average value of 1.33 nm is found for the standard deviation of the temporal OPL variation at each pixel, evaluated over 284 resulting images. The red curve in Figure 2.2(d) shows a histogram of the temporal OPL variation. Apparently, tSLIM has a comparative temporal sensitivity to the white-light DPM [37] (1.1 nm temporally) but lower than the SLIM setup using a PAN-SLM [32] (0.28 nm spatially and 0.029 nm temporally). Apart from pristine optics and alignment quality, lower spatial and temporal sensitivity in tSLIM can be explained by a lower diffraction efficiency, 55% for TNLC-SLMs (LC2002, Holoeye Inc.)

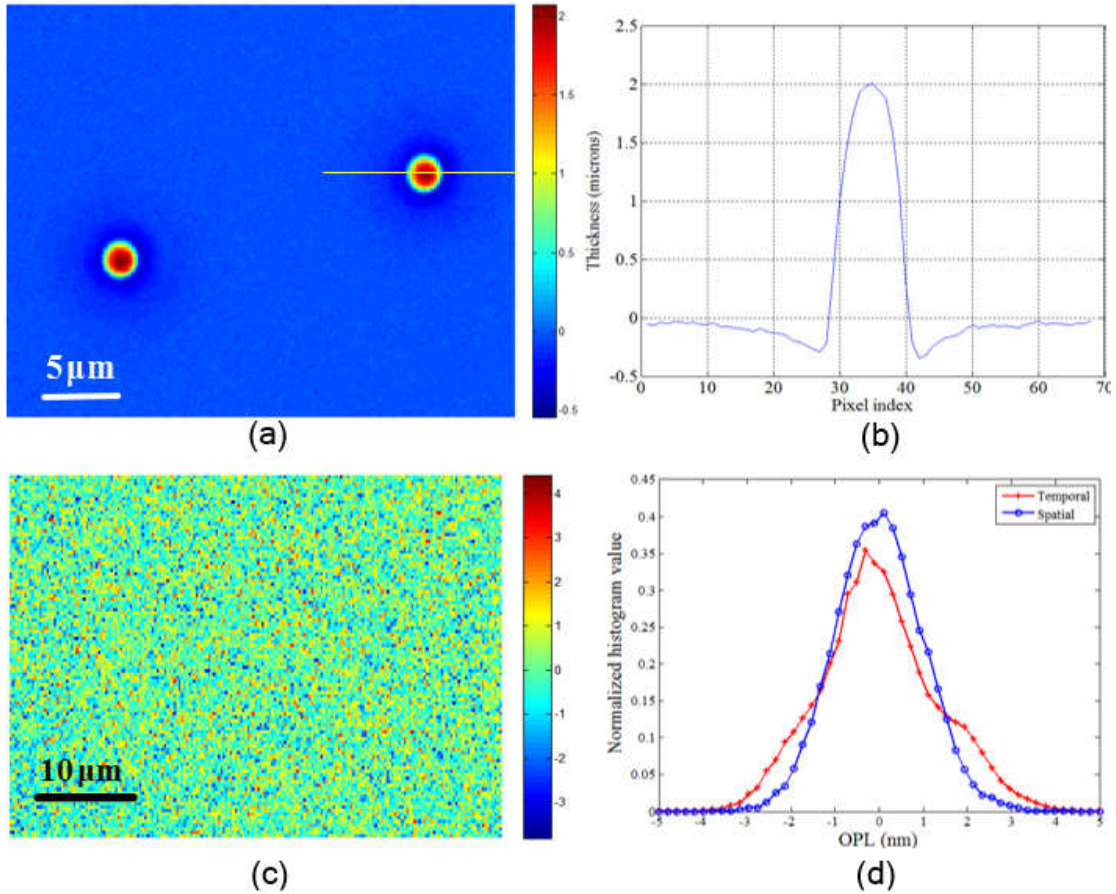


Figure 2.2 (a) Thickness map (in microns) of two $2\text{-}\mu\text{m}$ polystyrene micro-beads. (b) Cross-section along the line profile in (a). (c) Quantitative optical path length (OPL) map of a background region in a single frame. The unit is in nanometers. (d) Blue: Histogram of optical path length in the few of view shown in (c) (standard deviation $\sigma_s = 0.99\text{ nm}$). Red: Histogram of optical path length at a single pixel across 284 frames (standard deviation $\sigma_t = 1.33\text{ nm}$).

Finally, we show experimental results with human cancer cervical epithelial (HeLa) cells. The cells were placed in a 35 mm glass-bottom dish and kept at 37°C in the incubator to develop to a sufficient confluence. Then, a glass cap is applied on the top to prevent evaporation during imaging. Figure 2.3 shows phase contrast images next to transmission SLIM images at two different planes at $z = 0\text{ }\mu\text{m}$ and $z = 1.8\text{ }\mu\text{m}$. Note that tSLIM images suffer from the halo effects similar to the PC microscopy. This effect is due to spatial coherence of the illumination, which will be covered in detail in the next section.

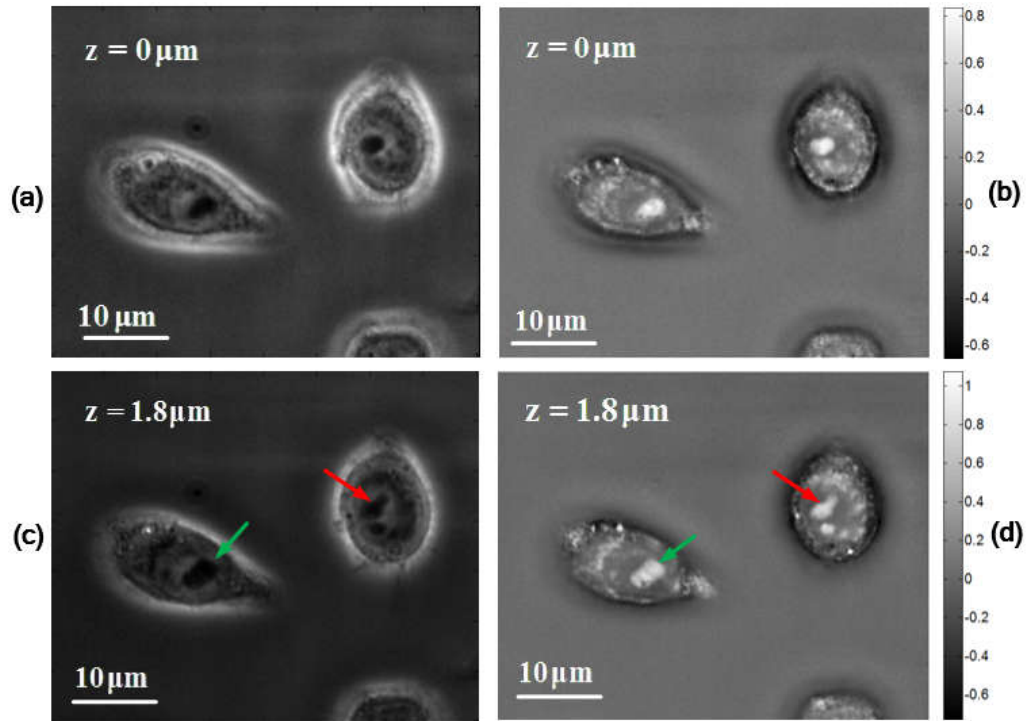


Figure 2.3 Phase contrast (left) and transmission SLIM (right) comparison. (a), (b) Phase contrast and SLIM images of two HeLa cells at $z = 0\mu\text{m}$. (c), (d) Phase contrast and SLIM images of the HeLa cells at $z = 1.8\mu\text{m}$.

The green arrows point to the location of nucleoli. The color bars are phase values in radians.

CHAPTER 3: QPI WITH PARTIALLY COHERENT ILLUMINATION

3.1 Image formation

In this chapter, we consider the effect of the spatial coherence of the illumination on QPI measurements. Recall that in Chapter 2, when describing the relationship between the sample field U_p and the sample transmittance, T , we have assumed that $U_p(\mathbf{r}_\perp) = cT(\mathbf{r}_\perp)$ for some constant c . However, this assumption is only valid when the illumination is spatially coherent or at least, when the coherence area [78] is larger than the field of view. In the most general settings, we have $U_p(\mathbf{r}_\perp, t) = U_i(\mathbf{r}_\perp, t)T(\mathbf{r}_\perp)$, where $U_i(\mathbf{r}_\perp, t)$ is the time-varying incident field. When the incident field U_i is not smooth enough over the scale of FOV, which happens when the illumination is only partially spatially coherent [35], the effects of the incident field cannot be ignored. Here, we consider cases when $U_i(\mathbf{r}_\perp, t)$ cannot be well approximated by such constant c . Moreover, we only consider QPI methods that belong to the interferometry family. The effect of spatial coherence on the non-interferometry QPI method is outside the scope of this thesis and had been studied elsewhere, e.g., [24, 79, 80]. Interferometry setups require two fields: the sample field, U_p , and a reference field, U_r . The measurable phase quantity of these systems is

$$\phi_m(\mathbf{r}_\perp) = \arg[\Gamma_{p,r}(\mathbf{r}_\perp, \mathbf{r}_\perp, 0)], \quad (3.1)$$

where $\Gamma_{p,r}(\mathbf{r}_\perp, \mathbf{r}_\perp, 0) = \langle \mathbf{U}_p(\mathbf{r}_\perp, t) \mathbf{U}_r^*(\mathbf{r}_\perp, t) \rangle_t$ is the temporal cross-correlation between these two fields, evaluated at zero-delay, $\tau = 0$. Depending on how the reference field, U_r , is generated, the interferometry family can be divided into two subgroups: *traditional*

interferometry and *common-path* interferometry (see Figure 3.1 for a schematic). Next, we study the effect of spatial coherence in details for each subgroup.

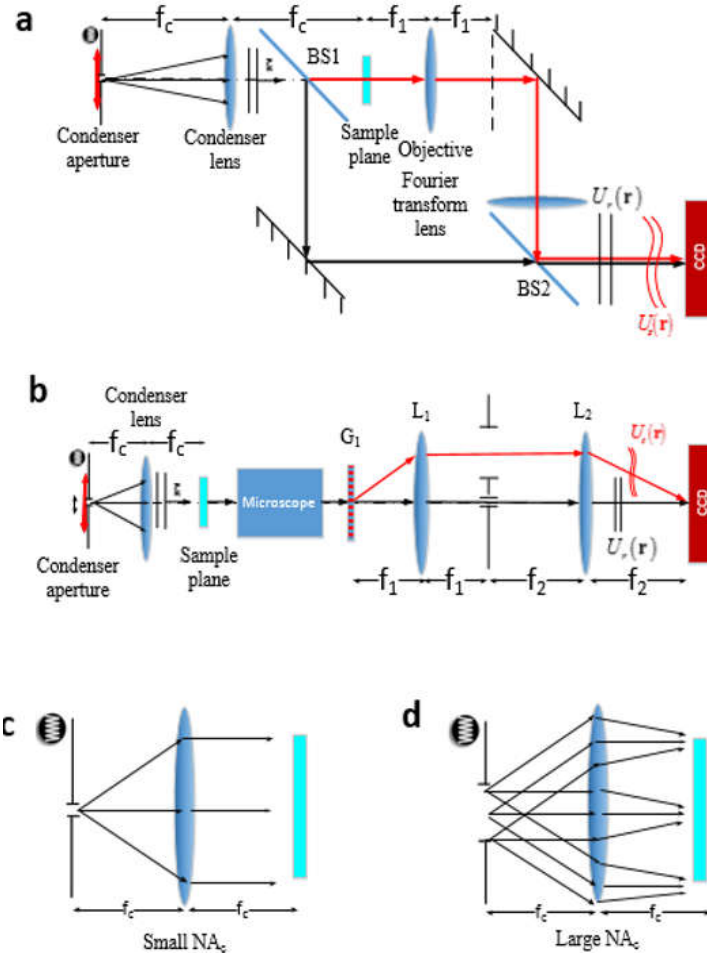


Figure 3.1 Interferometry QPI methods. (a) *Traditional* interferometry: the illumination field, U_i , is split into two components. The first one goes through the sample to generate the sample field, U_p . The other serves as the reference field, U_r . Then, they interfere with each other at the CCD plane. (b) *Common-path* interferometry: the sample field, U_p , is relayed to the output port of the microscope. Afterward, the reference field, U_r , is derived by spatially filtering the sample field, U_p , using a physical pinhole placed at the back Fourier plane of the lens L_1 . The first order diffraction pattern generated by a grating G_1 is used as the sample field, U_p , at the detector plane. (c) A low numerical aperture of the condenser, NA_{con} , increases the spatial coherence of the illumination field. (d) High NA_{con} reduces the spatial coherence.

3.1.1 Traditional interferometry

In traditional interferometry, Figure 3.1(a), the reference field is a copy of the illumination, i.e., $U_r = U_i$. Again, the sample field is $U_p(\mathbf{r}_\perp, t) = U_i(\mathbf{r}_\perp, t)T(\mathbf{r}_\perp)$. Hence,

$$\Gamma_{p,r}(\mathbf{r}_\perp, \mathbf{r}_\perp, 0) = T(\mathbf{r}_\perp) \left\langle \mathbf{U}_i(\mathbf{r}_\perp, t) \mathbf{U}_i^*(\mathbf{r}_\perp, t) \right\rangle_t = T(\mathbf{r}_\perp) I_i(\mathbf{r}_\perp), \quad (3.2)$$

where $I_i(\mathbf{r}_\perp) = \left\langle |U_i(\mathbf{r}_\perp, t)|^2 \right\rangle_t$ is the intensity of the incident field. Since $I_i(\mathbf{r}_\perp)$ is a positive quantity, the measured phase, $\phi_m(\mathbf{r}_\perp) = \arg[\Gamma_{p,r}(\mathbf{r}_\perp, \mathbf{r}_\perp, 0)] = \arg[T(\mathbf{r}_\perp)]$, is identical with the phase of interest, $\phi(\mathbf{r}_\perp) = \arg[T(\mathbf{r}_\perp)]$. Therefore, traditional interferometry QPI measurements can be performed accurately regardless of the spatial coherence of the illumination, as long as the reference and illumination fields are identical. There is also no halo and phase reduction phenomenon associated.

3.1.2 Common-path interferometry

Next, let us consider the case when the reference field U_r is derived by spatially filtering the sample field U_s via, for example, passing the central portion of its Fourier transform through a small physical pinhole (see Figure 3.1(b)). Denoting the spatial filtering kernel characterizing this operation by $h_o(\mathbf{r}_\perp)$, the reference field can be written in an explicit form as

$$\mathbf{U}_r(\mathbf{r}; \omega) = \mathbf{U}_i(\mathbf{r}; \omega) \circledast_{\mathbf{r}_\perp} h_o(\mathbf{r}), \quad (3.3)$$

where $\circledast_{\mathbf{r}_\perp}$ is the two-dimensional convolution operator. In this case, the temporal cross-correlation function becomes

$$\begin{aligned}
\Gamma_{p,r}(\mathbf{r}_\perp, \mathbf{r}'_\perp, 0) &= \langle \mathbf{U}_p(\mathbf{r}_\perp, t) \mathbf{U}_r^*(\mathbf{r}'_\perp, t) \rangle_t \\
&= \left\langle \mathbf{U}_i(\mathbf{r}_\perp, t) T(\mathbf{r}_\perp) \left\{ [\mathbf{U}_i T] \odot_{\mathbf{r}_\perp} h_o \right\}^*(\mathbf{r}'_\perp) \right\rangle_t \\
&= T(\mathbf{r}_\perp) \int \langle \mathbf{U}_i(\mathbf{r}_\perp, t) \mathbf{U}_i^*(\mathbf{r}'_\perp, t) \rangle_t h_o^*(\mathbf{r}_\perp - \mathbf{r}'_\perp) T^*(\mathbf{r}'_\perp) d^2 \mathbf{r}'_\perp \\
&= T(\mathbf{r}_\perp) \int \Gamma_i(\mathbf{r}_\perp, \mathbf{r}'_\perp, 0) h_o^*(\mathbf{r}_\perp - \mathbf{r}'_\perp) T^*(\mathbf{r}'_\perp) d^2 \mathbf{r}'_\perp,
\end{aligned} \tag{3.4}$$

where $\Gamma_i(\mathbf{r}_\perp, \mathbf{r}'_\perp, 0)$ is the mutual intensity function [78] of the illumination, which, under statistical homogeneity, becomes $\Gamma_i(\mathbf{r}_\perp, \mathbf{r}'_\perp, 0) = \Gamma_i(\mathbf{r}_\perp - \mathbf{r}'_\perp, 0)$, a function of the variable difference. Then, Eq. (3.4) becomes

$$\begin{aligned}
\Gamma_{p,r}(\mathbf{r}_\perp, \mathbf{r}'_\perp, 0) &= T(\mathbf{r}_\perp) \int \Gamma_i(\mathbf{r}_\perp - \mathbf{r}'_\perp) h_o^*(\mathbf{r}_\perp - \mathbf{r}'_\perp) T^*(\mathbf{r}'_\perp) d^2 \mathbf{r}'_\perp \\
&= T(\mathbf{r}_\perp) \left[T \odot_{\mathbf{r}_\perp} h \right]^*(\mathbf{r}_\perp),
\end{aligned} \tag{3.5}$$

where we have defined a new quantity, $h(\mathbf{r}_\perp) = \Gamma_i^*(\mathbf{r}_\perp, 0) h_o(\mathbf{r}_\perp)$. Equation (3.5) establishes a relationship between the measurable quantity in QPI, $\Gamma_{p,r}(\mathbf{r}_\perp, \mathbf{r}'_\perp, 0)$, and the transmission function of the object, T . When: 1) the illuminating field U_i is spatially partially coherent and characterized by the correlation function, $\Gamma_i(\mathbf{r}_\perp, 0)$, and 2) the reference field U_r is obtained by blurring the sample field via a kernel $h_o(\mathbf{r}_\perp)$. As a side note, expanding the condenser aperture of the illumination decreases the degree of coherence for the illumination; i.e., Γ_i becomes narrower and vice versa. In contrast to the previous case, now the measurable quantity, $\Gamma_{p,r}(\mathbf{r}_\perp, \mathbf{r}'_\perp, 0)$, is no longer just the transmission function $T(\mathbf{r}_\perp)$, multiplied by a positive quantity. In this case, the measured phase, ϕ_m , differs from the expected value. More specifically,

$$\phi_m(\mathbf{r}_\perp) = \phi(\mathbf{r}_\perp) - \arg \left[\left(T \odot_{\mathbf{r}_\perp} h \right) (\mathbf{r}_\perp) \right]. \tag{3.6}$$

Equation (3.6) is the key result of this section and [35]. It will be later used to explain the halo and the phase underestimation effects.

3.2 Three-dimensional partially coherent QPI

The sample is usually scanned in the axial dimension in tomography applications. For each axial coordinate, z , a different transverse phase image $\phi_m(\mathbf{r}_\perp, z)$ is measured. However, for optically thick specimens, the transverse transmission function $T(\mathbf{r}_\perp)$ is not sufficient to characterize the samples. Also, the phase of interest $\phi(\mathbf{r}_\perp)$ is not well defined [38]. In this section, we study the effects of spatial coherence of 3D weakly scattering samples, characterized by a susceptibility function $\chi(\mathbf{r})$. Here, $\mathbf{r} = (\mathbf{r}_\perp, z)$ is the 3D coordinate for a point of interest. This section summarizes results in our recent publication [38]. For simplicity, we only present main results with emphasis spent on the difference between the two cases. The measured phase in 3D speaks

$$\phi(\mathbf{r}) \approx \varphi(\mathbf{r}) - \varphi(\mathbf{r}) \odot_{\mathbf{r}} h_i(\mathbf{r}) = \varphi(\mathbf{r}) \odot_{\mathbf{r}} [\delta^{(3)}(\mathbf{r}) - h_i(\mathbf{r})], \quad (3.7)$$

where $\odot_{\mathbf{r}}$ is the 3D convolution operator. The phase $\varphi(\mathbf{r})$ is the “ideal” phase in 3D, expected with perfectly coherent illumination, and $h_i(\mathbf{r})$ is a generalization of the 2D mutual intensity function of the illumination, $\Gamma_i(\mathbf{r})$. However, the kernel $h_i(\mathbf{r})$, in spite of being a function of \mathbf{r} , only performs filtering in the transverse coordinate, \mathbf{r}_\perp , since $h_i(\mathbf{r}) = [\Gamma_i(\mathbf{r}_\perp) / \int \Gamma_i(\mathbf{r}'_\perp) d^2 \mathbf{r}'_\perp] \delta(z)$. Again, $\Gamma_i(\mathbf{r}_\perp)$ is the mutual intensity function of the illumination, evaluated at the image plane. Next, $\delta^{(3)}$ represents the 3D Dirac delta-function. Apparently, Eq. (3.7) is very similar to Eq. (3.6). Both of them tell that our 3D measurement $\phi(\mathbf{r})$ is also a high-pass filtered version of an ideal phase, $\varphi(\mathbf{r})$. The “ideal” phase, $\varphi(\mathbf{r})$, is a function of the sample susceptibility in 3D instead of the sample transmission. It is defined as

$$\varphi(\mathbf{r}) = [\beta_o / (2\bar{n})] \left[\chi \odot_{\mathbf{r}} \mathfrak{S}_{\mathbf{k}_\perp}^{-1} \left(e^{i(q-\bar{n}\beta_o)z} \right) \right](\mathbf{r}), \quad (3.8)$$

where β_o is the central wavenumber in free-space, \bar{n} is the spatially averaged refractive index, and q is the axial component relating with the transverse wavevector, \mathbf{k}_\perp , through the dispersion relation $q = \sqrt{\beta_o^2 - k_\perp^2}$. This ideal phase is a generalization of the 2D phase of interest, $\phi(\mathbf{r}_\perp)$. We show its convergence to the 2D phase of interest when the sample is thin and well-focused in Appendix A, Section A.2. We give a short proof for Eq. (3.7) in Appendix A, Section A.3.

3.3 Halo and phase underestimation artifacts

3.3.1 2D case

Equation (3.6) indicates that the measured phase at each point in the FOV depends on that at neighboring points, which is the result of the convolution with the kernel, $h(\mathbf{r}_\perp)$. It is physically insightful to discuss two asymptotic cases: i) extremely narrow h , i.e. $h_o(\mathbf{r}_\perp) \rightarrow \delta^{(2)}(\mathbf{r}_\perp)$ and ii) and extremely broad h , i.e. $h_o(\mathbf{r}_\perp) \approx \text{const}$. The first case happens when the illumination field is completely spatially incoherent, which results in a kernel h much narrower than the transmission T . Consequently, $(T \odot_{\mathbf{r}_\perp} h)(\mathbf{r}_\perp) \rightarrow T(\mathbf{r}_\perp)$, and the measured phase vanishes,

$$\phi_m^{\text{incoh}}(\mathbf{r}) \approx 0. \quad (3.9)$$

Thus, Eq. (3.9) establishes the impossibility of measuring any phase information using spatially incoherent light, even when the spatial filter used to render the reference field U_r is perfectly closed, i.e., $h_o(\mathbf{r}_\perp) \approx \text{const}$. By contrast, if the illumination field is perfectly coherent, $\Gamma_i(\mathbf{r}_\perp - \mathbf{r}'_\perp) \approx \text{const} \forall \mathbf{r}_\perp, \mathbf{r}'_\perp$, and, also, if the spatial filtering is perfect, $h_o(\mathbf{r}_\perp) \approx \text{const}$, the kernel $h(\mathbf{r}_\perp)$ becomes much broader than the object function $T(\mathbf{r}_\perp)$. In this case, we have $(T \odot_{\mathbf{r}_\perp} h)(\mathbf{r}_\perp) \approx \text{const}$, which gives an accurate measurement,

$$\phi_m^{\text{coh}}(\mathbf{r}_\perp) = \phi(\mathbf{r}_\perp). \quad (3.10)$$

All situations of experimental relevance exist between the two extreme cases of complete coherence and complete incoherence, described by Eqs. (3.9) and (3.10), respectively. When the coherence area of the illumination field is comparable to the size of the object of interest, the measured phase map misses the low frequencies contained in the function $(T \otimes_{r_{\perp}} h)$. This artifact is well known as the “halo effect” in phase contrast microscopy.

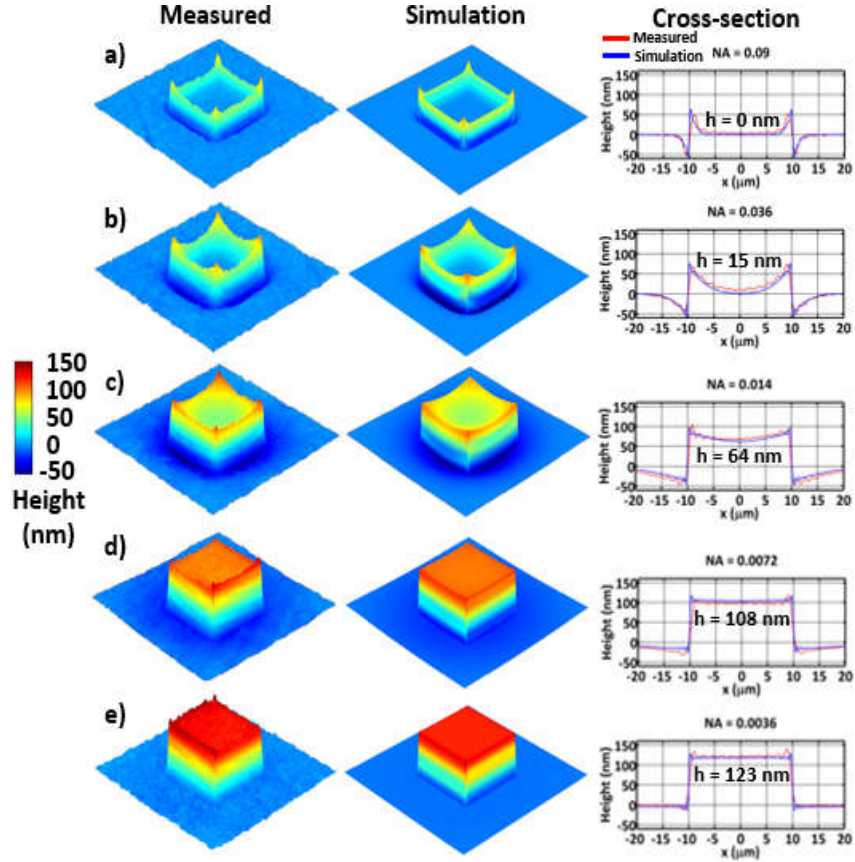


Figure 3.2 Comparison between measured and calculated profiles for quartz pillars, as described in text. The

NA_{con} values are decreasing from (a) to (e), as shown above each topography profile.

To justify our model, we show a comparison between experimental measurements and our theoretical prediction using the formulae derived above. Our analyses were performed using DPM (Figure 3.1(b)) set up with various values of the condenser numerical aperture, NA_{con} . More details about the optical setup and procedure for obtaining the correlation

function, $\Gamma_{p,r}(\mathbf{r}_\perp, \mathbf{r}_\perp, 0)$, from the interference pattern, can be found in [40]. A brief description of this step is given in Appendix A, Section A.1. For this experiment, transparent quartz micropillars were fabricated with known dimensions to serve as control samples. A 1" quartz wafer was patterned using SPR 511a positive photoresist and transferred to the quartz substrate by etching in a reactive ion etcher (RIE) using a CF₄ (Freon 14) plasma, resulting in square micropillars of various widths and a height of 123 nm, measured by the Alpha Step IQ Profilometer. The refractive index of quartz used in the simulation was 1.545 at the center wavelength of the source of 574 nm. This central wavelength is measured experimentally [81]. We obtained the phase maps and their topography associated with 5, 10, 20, and 40 μm width pillars.

Figure 3.2 and Figure 3.3 show a comparison between our theoretical predictions and experimental measurements taken using DPM. To model the effects of spatial coherence on QPI measurements, calculations based on Eq. (3.6) were performed in MATLAB for the case of monochromatic light at the central wavelength. In our calculations, the DPM pinhole filter was assumed to be perfect, i.e., $h_o(\mathbf{r}_\perp) \approx \text{const}$, which is a good approximation when using a 10 μm pinhole under the current DPM configuration [81]. The spatial power spectrum associated with the condenser aperture is approximated very well by a Gaussian function (see inset on the top-right corner of Figure 3.3). Clearly, our calculation predicts very well the phase reduction under partially coherent illumination. Furthermore, the model also accurately describes artifacts in the measured topography, i.e., the halos commonly observed in QPI and phase contrast microscopy [8, 81]. Notice that opening up the condenser aperture reduces the spatial coherence to the point where only edges of the pillar appear in the phase image, which matches the theoretical prediction. However, using smaller pinholes for spatially filtering the illumination light results in increasingly accurate phase and topography measurement, as

summarized in Figure 3.3. In other words, as the coherence area increases, the halo diminishes, and the height map converges to the ground truth.

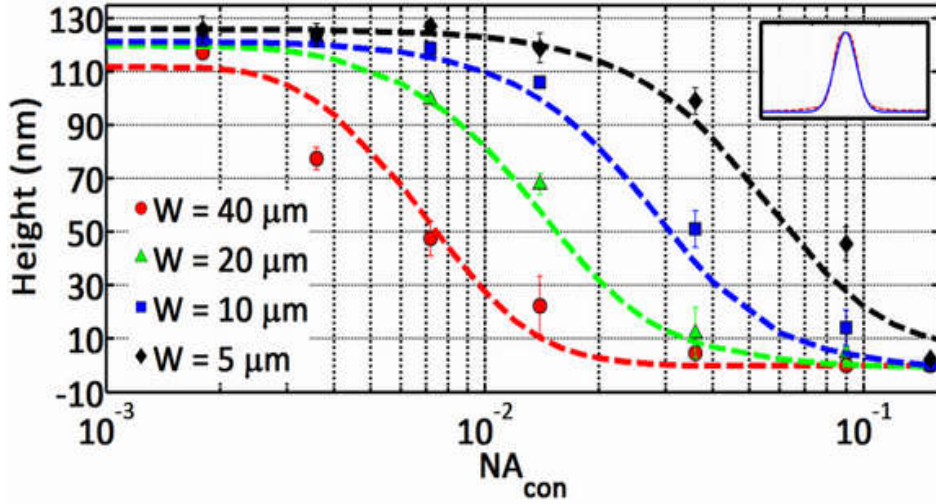


Figure 3.3 Comparison between measured (markers) and calculated (Eq. (3.6)) pillar height values (lines) vs. NA_{con} for four different pillars. The inset shows the fit of the condenser aperture with a Gaussian function.

3.3.2 Halos in 3D imaging

Similar to the 2D case, the 3D phase measurement also suffers from the halo and phase underestimation artifacts. The explanations for these phenomena are the same in both cases. However, since $h_i(\mathbf{r}) = \left[\Gamma_i(\mathbf{r}_\perp) / \int \Gamma_i(\mathbf{r}'_\perp) d^2 \mathbf{r}'_\perp \right] \delta(z)$, it follows directly that the halo effect does not change along the axial dimension and not affected by defocusing. Again, the quartz pillars were to verify our model. We obtained DPM phase measurements, $\phi(\mathbf{r})$, at several z-steps and with different values of NA_{con} . The step size is set to $0.57 \mu m$, about 4.6 times the pillar's thickness. For each value of NA_{con} , z-values in the range of $[-12.5, 12.5] \mu m$ from the central sample plane were acquired. Figure 3.4(b), 3.4(d), and 3.4(f) show our measurements and simulation results for $\phi(\mathbf{r})$ at different z-positions with $NA_{con} = 0.0072$. Clearly, the simulation has an excellent agreement with the experiments as shown in the Figure 3.4 (a), (c), and (e).

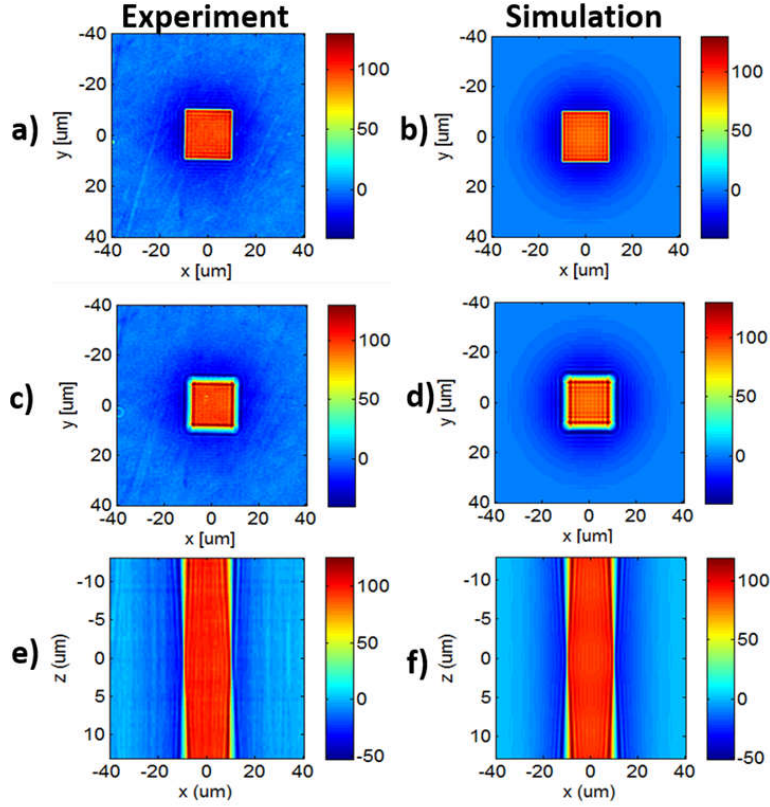


Figure 3.4 Experimental (left) and simulated (right) thickness measurements in nanometers for 3D pcQPI imaging of a 20 μm width, 123 nm thick micro-pillar at $NA_{con} = 0.0072$. (a) and (b) show the thickness recovered from $\phi(\mathbf{r}_{\perp})$ at the sample plane. (c) and (d) are thickness measurements at +10 μm from the sample plane. (e) and (f) show the x-z cross-section for the thickness measurements at $y = 0.0 \mu\text{m}$. The halo and phase reduction can be seen for all these z-steps.

Figure 3.5 shows experimental and simulated cross-sectional profiles for the thickness measurements at different values of NA_{con} at the sample plane and +10 μm from it. The height profiles confirm that, as the sample is scanned through focus, the object blurs but the halo remains unchanged. In our simulation, we use a Gaussian profile for the spatial power spectrum of the illumination, $\tilde{\Gamma}_i(\mathbf{k}_{\perp})$, with a standard deviation of $\beta_o NA_{con}$. Good agreement between the simulated and measured profiles can be seen at the sample plane in Figure 3.5(a) and (b). However, at $z = +10 \mu\text{m}$ from the sample plane, in Figure 3.5(c) and (d), the simulation

exhibits more significant modulation (“ringing”) than the experiment. This phenomenon can be attributed to various smoothing effects in the optical setup and the fact that our simulation is based on monochromatic light, while in the actual experiment, the illumination has a finite bandwidth around this frequency. Therefore, the diffraction ringing is washed out in experiments due to the combination of different diffraction kernels at various optical frequencies.

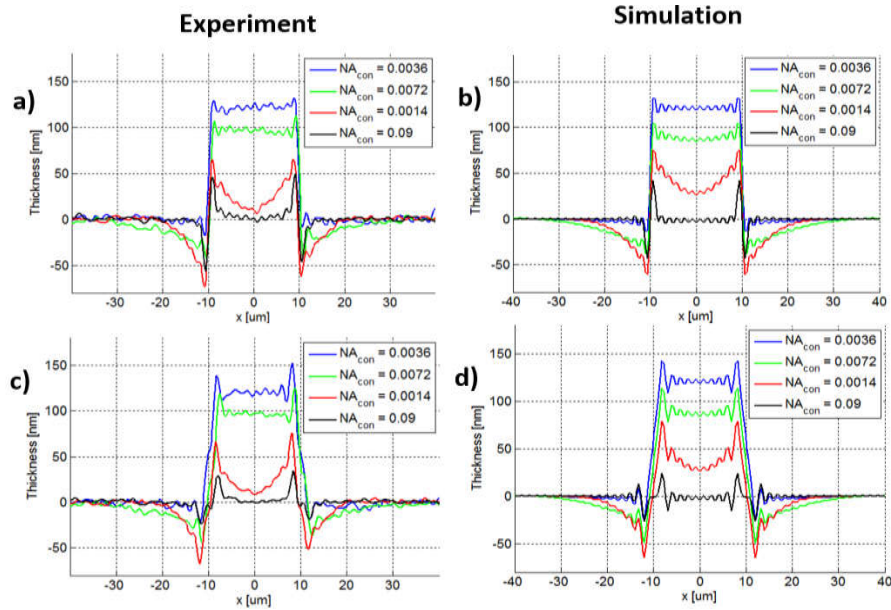


Figure 3.5 Comparison between the experimental and simulated profiles for 123 nm quartz pillars for different values of NA_{con} at the plane of sample (a), (b) and at 10.0 μm from the sample plane (c) and (d).

Figure 3.6 illustrates the independence of defocusing, which is due to the low-pass filtering performed by the microscope objective, and the halo effect, which is the result of low spatial coherence. Figure 3.6(a) shows three different x-z cross-sections of the phase measurement $\phi(x, y = 0, z)$ for three different values of NA_{con} . The phase underestimation and halo effects can be seen in the second and the third cases. To get an insight into how these effects vary vs. the depth z , we take the 1D Fourier transform $|\tilde{\phi}(k_x, y = 0, z)|$ of the cross-sections at $z = 0.0 \mu\text{m}$ and $z = 15.0 \mu\text{m}$. We first find regions in the spatial spectra that are

affected by the halo only, defocusing only or both. From Eq. (3.7), it can be seen that the band-pass kernel $\left[\delta^{(3)}(\mathbf{r}) - h_i(\mathbf{r})\right]$ acts as a high-pass filter, suppressing low-frequency components of the ideal phase $\varphi(\mathbf{r})$. Hence, the spatial frequency domain can be divided into two regions. Region 1 is only affected by the defocusing and the frequency spectrum of the object $\tilde{\chi}$. Region 2 is affected by all factors, including defocusing, low-frequency suppression and $\tilde{\chi}$. It is clear from Figure 3.6(b) that for each z-position, the amplitude spectra in region 1 are almost identical for each value of NA_{con} , indicating that the spatial coherence only affects the low-frequency range of the measured phase. Defocusing and depth sectioning only relate to the numerical aperture of the objective, NA_{obj} . Figure 3.6(c)-(e) show amplitude spectra for the three different values of z at $NA_{con} = 0.0036, 0.0072,$ and 0.014 respectively. Note that the spectra are almost the same for region 2 for all three values of z, indicating that the low-frequency suppression due to the spatial coherence kernel $\left[\delta^{(3)}(\mathbf{r}) - h_i(\mathbf{r})\right]$ is essentially invariant to the depth z.

Next, we expand our analysis to a thick, weakly scattering sample using simulation. Figure 3.7(a) shows x-y and x-z cross-sections of a simulated squared micropillar of dimension $30 \times 30 \times 25 \mu\text{m}^3$, where $25 \mu\text{m}$ is the thickness. The simulated pillar has a refractive index value of 1.01. The surrounding media has the refractive index of 1.00. Using the central wavelength of $0.574 \mu\text{m}$, the total phase shift generated by this pillar is 2.19 rad. As a side note, we have intentionally chosen the thickness and the refractive index so that the total phase shift is less than 2π to avoid any possible phase wrapping. Figure 3.7(b) shows one x-z and three x-y cross-sections of the ideal phase, $\varphi(\mathbf{r})$, using its formula given in Eq. (3.7). The x-z one is evaluated through the center of the pillar at the plane $y = 0 \mu\text{m}$. The x-y ones are

evaluated at three different planes $z = 0, z = -10, z = 20 \mu\text{m}$, denoted in the x-z cross-section. A total phase shift of 2.19 rad can be observed in all three x-y cross-sections with different amounts of defocusing. Figure 3.7(c) shows the x-z cross-sections of the measured phase under different numerical apertures of the condenser $NA_{con} = 0.0036, 0.0072, \text{ and } 0.014$ respectively. Dashed black rectangles denote the regions corresponding to the location of the pillar. Obviously, the halo and phase under-estimation get worse at larger values of NA_{con} . These effects are decoupled from the defocusing as discussed in the previous section. The code for our simulation can be obtained at: https://github.com/thnguyn2/3D_halo_modeling.git.

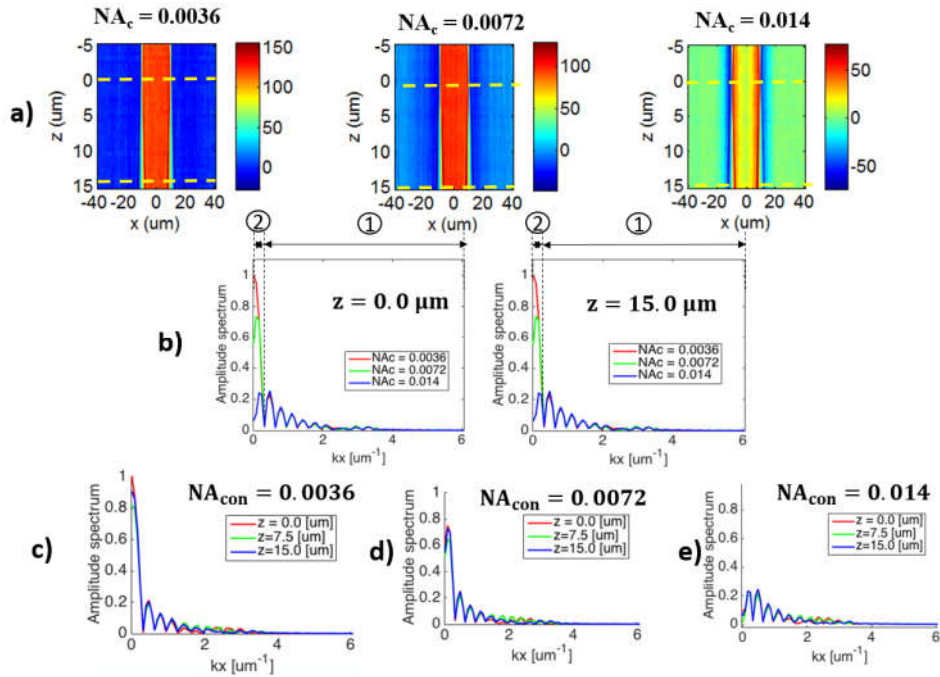


Figure 3.6 (a) Three different x-z cross-sections for three different values of NA_{con} . (b) Amplitude spectrum at $z = 0.0 \mu\text{m}$ and $z = 15.0 \mu\text{m}$. (c)-(e) Amplitude spectra for three different values of z at $NA_{con} = 0.0036, 0.0072$ and 0.014 , respectively.

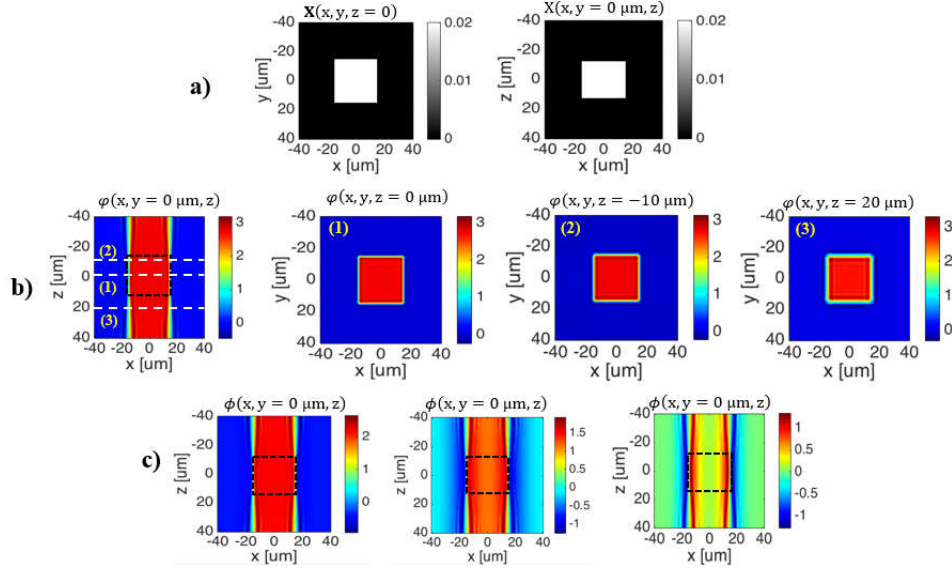


Figure 3.7 (a) x-y and x-z cross-sections of a simulated micro-pillar of dimensions $30 \times 30 \times 25 \mu\text{m}^3$. (b) One x-z and three x-y cross-sections of the “ideal” phase, $\varphi(\mathbf{r})$. The dashed rectangle denotes the locations of the pillar. The next three cross-sections are evaluated at three different planes $z = 0.0, -10.0, 20 \mu\text{m}$, denoted by the white lines in the x-z cross-section, respectively. (c) x-z cross-sections of the measured phase, $\phi(\mathbf{r})$, evaluated at three different values of NA_{con} , namely 0.0036, 0.0072 and 0.014.

3.4 Summary

This chapter presented a quantitative description and a mathematical model for the role of spatial coherence in QPI for both common-path and non-common-path configurations. The developed model explains the presence of the halo effect and the observed reduction in measured phase values. In the next chapter, we demonstrate how this model can be used to correct for these phenomena and remove the halo in the well-known phase contrast microscopy.

CHAPTER 4: HALO-FREE PHASE CONTRAST MICROSCOPY

4.1 Introduction

The phase contrast (PC) method is one of the most impactful developments in the four-century long history of microscopy. It allows for intrinsic, nondestructive contrast of transparent specimens, such as live cells. However, PC is plagued by the *halo* artifact, a result of insufficient spatial coherence in the illumination field, which limits its applicability. We present a new approach for retrieving halo-free phase contrast microscopy (hfPC) images by upgrading the conventional PC microscope with an external interferometric module, which generates sufficient data for reversing the halo artifact. Measuring four independent intensity images, our approach first measures haloed phase maps of the sample. We solve for the halo-free sample transmission function by using a physical model of the image formation under partial spatial coherence developed in Chapter 3. Using this halo-free sample transmission, we can numerically generate artifact-free PC images. Furthermore, this transmission can be further used to obtain quantitative information about the sample, e.g., the thickness with known refractive indices, dry mass of live cells during their cycles. The approach is applicable not only to SLIM but also to other common-path methods, e.g., DPM [20] and FPM [31]. We tested our hfPC method on various control samples, e.g., beads and pillars, and validated its potential for biological investigation by imaging live HeLa cells, red blood cells, and neurons.

4.2 Background

Despite its 400-year history, light microscopy continues to be the most common tool in biomedicine [82]. Between the two most important characteristics of a microscopic image, *resolution* and *contrast*, it is improving the latter that has driven most of the technology

development in the light microscopy field. Once Abbe, in 1873, described *diffraction* as the ultimate limit of the far-field optical resolution, researchers focused mostly on approaching this theoretical limit rather than exceeding it [3]. This dogma remained unchallenged until the 1990s when the nonlinear optical interaction with the sample proved to be a feasible approach for breaking the diffraction limit with far-field optics [83].

Contrast, on the other hand, has not been proven to be bound by a universal physical law. Unlike the resolution, which is a property entirely of the optical system, the contrast depends on both the instrument and the object of interest (see, e.g., vol. 2 in Ref. [84]). The main challenge identified early on was to generate images of appreciable contrast when the specimen of interest is transparent. Since such objects, including most live cells, do not absorb or scatter visible light significantly and because all photo-detectors, including the retina, only respond to power, the resulting intensity distribution across the image is uniform, i.e., the image lacks contrast. This class of transparent specimens is referred to as *phase objects*, pointing to the fact that they only modulate the phase of the incident field and not its amplitude or irradiance (see Chapter 4 in Ref. [8]).

In the second part of the 19th century, a solution to this problem was developed in the form of tagging the structure of interest with stains or fluorophores, thus, converting the phase specimens into an *amplitude objects*. This approach enjoys the benefit of *specificity*, i.e., the capability of tagging and, thus, imaging only a particular structure of the interest. As a result, these methods of exogenous contrast have become broadly adopted. For example, imaging stained biopsied tissue has been the gold standard in clinical pathology for a century. Also, fluorescence microscopy is the most common form of microscopy in cell biology [85]. However, adding external chemicals to the specimens under investigation is likely to affect its natural structure and function. The fluorescence excitation light, often in the UV range, has been proven toxic to the live cells. In addition to phototoxicity, *photobleaching*, i.e., the

irreversible conformational change of a fluorophore that results in fluorescence quenching [86], is also a major limitation. Photobleaching typically reduces the interval of continuous imaging to only a few minutes.

In response to these challenges, phase contrast (PC) microscopy was developed by Zernike in the 1930s as a method of intrinsic contrast [87]. Zernike's idea was based on the fundamental understanding of an image as an interferogram, a concept put forward earlier by Abbe [3]. The innovation in PC is as powerful as it is simple: introducing a $\pi/2$ phase between the incident and the scattered components of the image field. Suddenly, fine details from within the live, unlabeled cells become visible with high contrast. As a result, PC is now widely used to visualize cells virtually in all biology laboratories. The significant contrast improvement was achieved by treating the microscope as a massively parallel interferometer, in which the incident field acts as the common reference field for all points in the field of view (see Chapter 8 in Ref. [88]). Clearly, unlike common bright field microscopy, PC requires a spatially coherent illumination field. However, strong spatial filtering necessary to boost the coherence of the light emitted by the microscope lamp comes at the expense of power loss. Thus, current commercial microscopes sacrifice spatial coherence to maintain practical levels of illumination power. As a result, the incident light carries a range of \mathbf{k} -vectors, instead of just one, which means that the reference of the interference at the image plane is not perfectly flat, but contains spatial structure. The resulting PC image exhibits an artifact, especially at the edges of the object. This artifact, known as the *halo*, has plagued PC ever since its conception, i.e., for more than eight decades.

4.3 Optical setup

Our imaging system consists of a phase-contrast microscope outfitted with an external phase-shifting module. As shown in Fig. 4.1(a), this unit is a re-purposed spatial light interference microscopy (SLIM) module [32] (CellVista SLIM Pro, Phi Optics, Inc.), designed for quantitative phase imaging. The total field, U_t , emanating from the sample is magnified and replicated in both amplitude and phase at the output port of the microscope. U_t is then polarized by polarizer P_1 and Fourier transformed by the lens L_2 at its back focal plane. At this plane, U_t is decomposed into the incident field (DC field), U_o , and a scattered component (AC field), U_s , which are spatially separated. Thus, the spatial Fourier transform of the DC field \tilde{U}_o is overlaid with the condenser annulus and the phase ring of the objective. The spatial Fourier transform of the AC component \tilde{U}_s covers the rest of the aperture. A spatial light modulator (SLM), placed at this plane, generates phase-shifting rings to further retard the phase of the DC field in increments of $\pi/2$, which becomes $e^{in\pi/2}\tilde{U}_o$, $n = 0, 1, 2, 3$, while leaving the AC field unmodified. Finally, the lens L_2 performs another Fourier transform to form the total field, $U_t = e^{in\pi/2}U_o + U_s$, at the camera plane. The camera captures four intensity images, $I(\mathbf{r}; n\pi/2) = |e^{in\pi/2}U_o + U_s|^2(\mathbf{r})$, and streams them to a computer to extract phase and amplitude information. Three different objectives with different magnifications, 20x/0.3NA, 40x/0.75NA, and 63x/1.4NA (oil immersed), were used in this work.

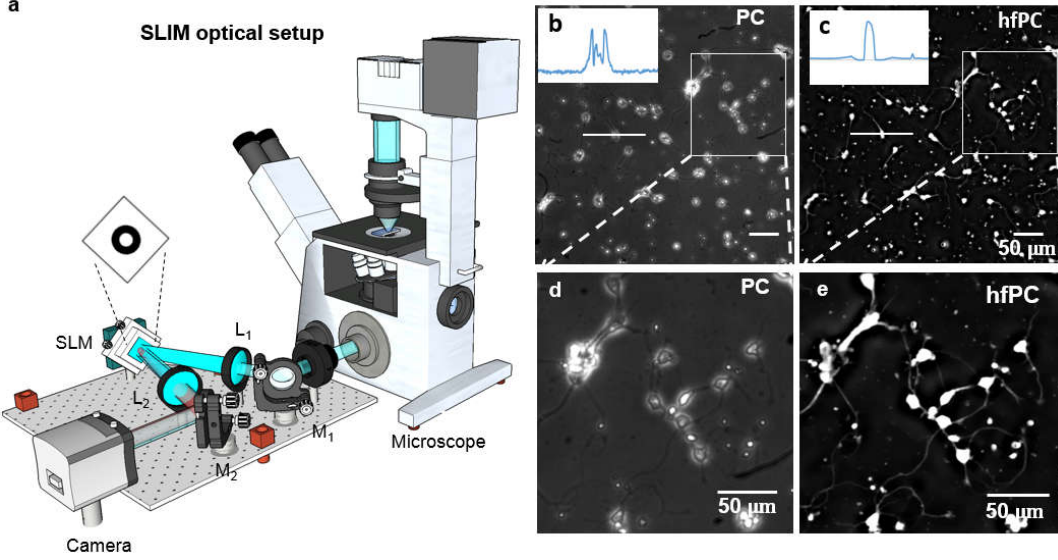


Figure 4.1 Optical setup. (a) The SLIM add-on module uses a 4-f system and a SLM coupled to the output port of a phase-contrast microscope. A camera is placed at the output of the module to record the interference intensity. Post-processing is performed on a computer to recover the phase quantity of interest. (b) Positive PC image of mouse neurons imaged using a 20x/0.3 NA objective. (c) Positive hfPC image. (d), (e), Zoomed-in image of the regions boxed by the rectangle in (b) and (c), respectively.

4.4 Image formation and the Halo artifact

Let T be the sample transmission and U_i be the illumination field. The total field emerging from the sample can be written as $U_t = TU_i$. The incident and scattered fields are, respectively, $U_o = (U_i \odot_r h_o)$, and $U_s = (U_i \odot_r h_s)$, with \odot_r the 2D spatial convolution operator, h_o the Fourier transform of the illumination “ring” pupil, and h_s the Fourier transform of the entire pupil minus the “ring”. The corresponding frequency-domain (transfer) functions are $\tilde{h}_o(\mathbf{k}) = \left\{ \Pi \left[k / (\beta_o NA_{\text{ring,max}}) \right] - \Pi \left[k / (\beta_o NA_{\text{ring,min}}) \right] \right\}$, and $\tilde{h}_s(\mathbf{k}) = \Pi \left[k / (\beta_o NA_o) \right] - \tilde{h}_o$, where $\Pi(\cdot)$ is the disk function defined as $\Pi(r) = 1$ if $r \leq 1$ and 0, otherwise. $NA_{\text{ring,min}}$ and $NA_{\text{ring,max}}$ are two numerical apertures corresponding to the inner and outer radii of the objective phase ring, $\beta_o = \omega_o / c$ is the wavenumber in vacuum, ω_o the angular frequency, and c the

speed of light in the vacuum. Clearly, \tilde{h}_o is a band-pass filter, i.e., it retains all spatial frequencies in $[\beta_o NA_{\text{ring,min}}, \beta_o NA_{\text{ring,max}}]$. The function \tilde{h}_s is also a band-pass filter, covering the rest of the spatial bandwidth, i.e., $\tilde{h}_o + \tilde{h}_s = \Pi[k/(\beta_o NA_o)]$, where NA_o is the numerical aperture of the objective. These functions are calculated using experimentally measured parameters of the SLIM system; see Appendix B, Section B.1. The intensity is given by

$$\begin{aligned} I(\mathbf{r}; n\pi/2) &= \left\langle \left| i^n U_o(\mathbf{r}) + U_s(\mathbf{r}) \right|^2 \right\rangle_t \\ &= I_1(\mathbf{r}) + I_2(\mathbf{r}) + i^n C_3(\mathbf{r}) + (-i)^n C_4(\mathbf{r}) \end{aligned} \quad (4.1)$$

where $I_1 = \langle U_o U_o^* \rangle_t$, $I_2 = \langle U_s U_s^* \rangle_t$, $C_3 = \langle U_o U_s^* \rangle_t$, $C_4 = \langle U_s U_o^* \rangle_t = C_3^*$. See Appendix B, Section B.1, for a derivation and Refs. [78, 89] for more detail. I_1, I_2 are the intensities of the incident field and the scattered field, respectively, while C_3 is the temporal cross-correlation function of the two fields at zero temporal delays, $\tau = 0$ [90]. The closed-form formulas for these quantities under partially coherent illumination are given in Appendix B, Section B.2. By the Cauchy-Schwarz inequality for inner products, we have $C_3 C_4 \leq I_1 I_2$. An equality holds in the temporal domain when $U_s(t) = c U_o(t), \forall t$, or $\tilde{U}_s(\omega) = c \tilde{U}_o(\omega), \forall \omega$, the optical frequency. Combining with the definitions of U_o and U_s , we have $[(U_i T) \odot_r \tilde{h}_s](\mathbf{r}, \omega) = c [(U_i T) \odot_r h_o](\mathbf{r}, \omega)$, which is satisfied when the filtering operations are not dependent on the optical frequency ω , i.e., $h_s(\mathbf{r}, \omega) = h_s(\mathbf{r})$ and $h_o(\mathbf{r}, \omega) = h_o(\mathbf{r})$. Assuming this condition is satisfied, hence, $C_3 C_4 = I_1 I_2$, and using the four intensity images, one can solve for I_1, I_2, C_3, C_4 explicitly (see Appendix B, Section B.2). Summing the solutions for I_1 and C_4 gives (see Section B.3 of Appendix B for derivation)

$$\begin{aligned}
J_1(\mathbf{r}) &= I_1(\mathbf{r}) + C_4(\mathbf{r}) \\
&\approx \left\{ T(\mathbf{r}) \left[T \circledast_{\mathbf{r}} (\Gamma_i h_o^*) \right]^*(\mathbf{r}) \right\}
\end{aligned} \tag{4.2}$$

where

$$\begin{aligned}
I_1 &= \iint d^2\mathbf{r}_1 d^2\mathbf{r}_2 \Gamma_i(\mathbf{r}_1 - \mathbf{r}_2) T(\mathbf{r}_1) T^*(\mathbf{r}_2) h_o(\mathbf{r} - \mathbf{r}_1) h_o^*(\mathbf{r} - \mathbf{r}_2), \\
C_4 &= \iint d^2\mathbf{r}_1 d^2\mathbf{r}_2 \Gamma_i(\mathbf{r}_1 - \mathbf{r}_2) T(\mathbf{r}_1) T^*(\mathbf{r}_2) h_s(\mathbf{r} - \mathbf{r}_1) h_o^*(\mathbf{r} - \mathbf{r}_2).
\end{aligned} \tag{4.3}$$

In Eq. (4.3), Γ_i is the mutual intensity of the illumination at the sample plane. Our goal is to solve for the sample transmission T when J_1 is known. For a phase object with transmission $T(\mathbf{r}) = e^{i\phi(\mathbf{r})}$, taking the arguments on both sides of Eq. (4.2), we obtain the expression for the experimentally measured phase as

$$\begin{aligned}
\phi_m(\mathbf{r}) &= \arg[J_1(\mathbf{r})] \\
&= \phi(\mathbf{r}) - \arg \left[e^{i\phi} \circledast_{\mathbf{r}} (\Gamma_i h_o^*) \right](\mathbf{r}),
\end{aligned} \tag{4.4}$$

Clearly, the effects of phase underestimation and ‘‘halo effect’’ in phase contrast microscopy can be seen directly from Eq. (4.4). Qualitatively, this effect results in the appearance of bright regions circumscribing dark objects or vice versa (depending on the type of phase contrast). The effect not only increases the complexity of applications such as cell tracking [91], automatic cell-segmentation [92], and automatic mitosis detection [93], but also diminishes direct correspondence between observed intensity images and the optical phase difference generated by the specimen. Several methods have been proposed to suppress these effects and make PC a quantitative technique. Optical solutions include using a special microscope objective equipped with an apodized phase plate [94]. Computational ones perform post-correction on raw PC images. In [95, 96], Yin et al. modeled the image formation process in PC and suggested solving for a halo-free PC image by solving an optimization problem with a l_1 -sparse prior on the expected solution.

4.5 Inverse problem

To obtain the correct $\phi(\mathbf{r})$ from the measured $J_1(\mathbf{r})$, we solve for $\phi^\dagger(\mathbf{r})$, the optimal phase, using the following constrained optimization problem:

$$\phi^\dagger(\mathbf{r}) = \arg \min_{\phi} \left\{ \left\| \phi_m(\mathbf{r}) - \phi(\mathbf{r}) + \arg \left[e^{i\phi(\mathbf{r})} \odot_{\mathbf{r}} (\Gamma_i h_o^*) \right] (\mathbf{r}) \right\|_2^2 + \lambda TV(\phi) \right\}, \quad (4.5)$$

In Eq. (4.5), $TV(\phi) = \int d^2\mathbf{r} \sqrt{(\partial\phi/\partial x)^2(\mathbf{r}) + (\partial\phi/\partial y)^2(\mathbf{r})}$, is the total variational term [97, 98], which suppresses the effect of noise and enforces the sparsity assumption on the gradation of the reconstruction. $\|\cdot\|_2$ denotes the l_2 -norm. The parameter λ is a trade-off factor that balances the measurement error and the TV term. The problem is solved using the limited-memory Broyden-Fletcher-Goldfarb-Shanno algorithm with *box* constraints (L-BFGS-B) [99-101], enforcing the solved phase to satisfy the non-negative constraint at each pixel, i.e., $\phi(\mathbf{r}) \geq 0$. More details on the source code and post-processing steps can be found in Appendix B, Section B.4. After this inversion, we can then numerically reconstruct both halo-free phase contrast images (hfPC) as well as halo-free quantitative phase images (hfQPI) as shown below

4.6 Reconstruct hrPC images from the inversed phase

Given the halo-free phase map $\phi^\dagger(\mathbf{r})$ and the halo-free sample transmission $T^\dagger(\mathbf{r}) = \exp[i\phi^\dagger(\mathbf{r})]$ obtained by solving the optimization problem, the hfPC intensity image can be computed easily. Practically, a conventional PC optical setup comes with a ring illumination annulus, that is sufficiently thick, to increase the illumination power and, therefore, boost the acquisition signal-to-noise ratio. However, this type of illumination is not necessary in order to compute the hfPC images from the sample transmission $T^\dagger(\mathbf{r})$. Instead, a pin-hole illumination can be used, i.e., $\tilde{\Gamma}_i(\mathbf{k}) = \delta^{(2)}(\mathbf{k})$, which means only the transverse

spatial frequency $\mathbf{k} = 0$ propagates through the system. Using Eq. (B.3) with $n = 1$ for the positive PC image, we obtain the positive hfPC image as

$$I_{halo-free}(\mathbf{r}) = I(\mathbf{r}; \pi/2) = \left[\left[(e^{i\mathbf{k}\cdot\mathbf{r}T}) \odot_{\mathbf{r}} (h_s + i^n h_o) \right] \right]^2(\mathbf{r}). \quad (4.6)$$

Here, the kernels h_o and h_s can be obtained from their respective Fourier transforms $\tilde{h}_o(\mathbf{k})$ and $\tilde{h}_s(\mathbf{k})$. Since the support of the phase ring of the objective needs to be matched the illumination annulus in PC microscopy, we can obtain these function as $\tilde{h}_o(\mathbf{k}) = 1(\mathbf{k} = \mathbf{0})$ and $\tilde{h}_s(\mathbf{k}) = \Pi[k/(\beta_o NA_o)] - \tilde{h}_o(\mathbf{k})$. Here, the function $1(x)$ is the Kronecker delta function, taking the value of 1 of $x = 0$ and 0, otherwise.

4.7 Results

4.7.1 hrPC imaging of neurons

Using this approach, we illustrate the halo removal in Zernike's phase contrast images of mouse neurons. Figure 4.1(b)-(c) show positive and negative phase contrast images of neurons using a 20x/0.3 NA objective. From the four QPI images, the halo-free phase map ϕ^\dagger is obtained by solving Eq. (4.5). This quantitative phase map is used to calculate the halo-free phase contrast (PC) image (see the Section 4.6, for details). These halo-free PC (hfPC) images are equivalent to what would be measured with an infinitely thin ring of illumination. Figure 4.1(d) shows the positive hfPC image. Images of zoomed-in regions from Figs. 4.1(b)-(c) are shown in Figs. 4.1(d)-(e), respectively. A formation of a neural network can be observed in this region from the halo-free positive phase contrast image, without the typical artifacts associated with phase contrast. The line profiles in Figs. 4.1(b)-(c) show how the negative values commonly associated with halos disappeared as a result of our method.

4.7.2 Thickness measurements of nanoscale topography samples

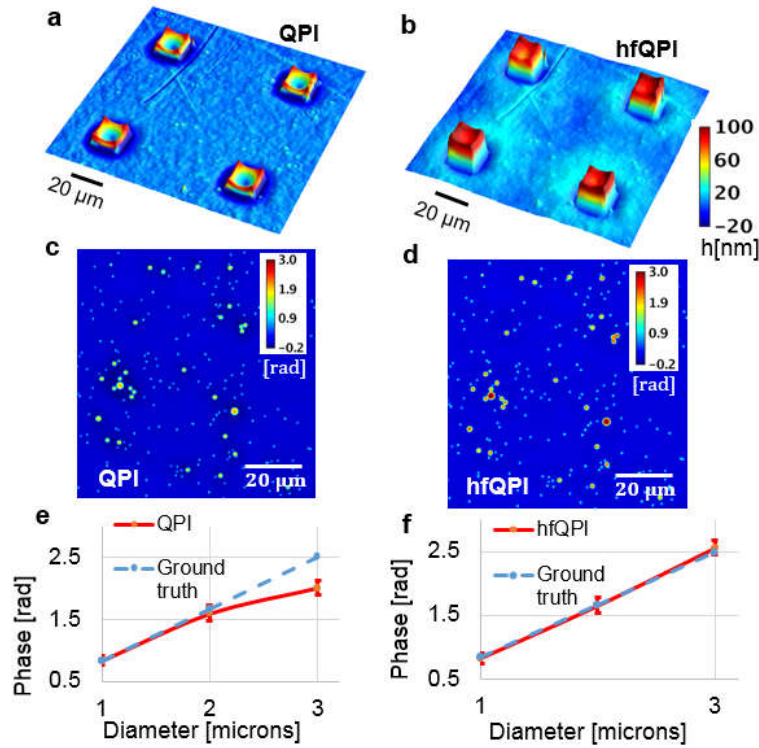


Figure 4.2 (a) Input height surface map of four quartz micro-pillars that are 20 μm wide and 80-nm high measured using a 20x/0.3 NA objective. The unit is nm. (b) The halo-free surface map of (a). (c) Measured phase map of a mixture of 1, 2 and 3-μm polystyrene beads image under the same setup. Note that the halo affects the small beads less than the large beads. (d) Halo-free version of (c). (e), (f), Diameter profiles for different sizes of the beads for (c) and (d), respectively. Dashed lines are expected ground truth profiles.

The hfQPI can be used to provide highly accurate topography measurements at the nanoscale. In order to demonstrate that halo-free images can be used to profile quantitatively transparent samples, we measured the thickness of quartz micro-pillar samples. The pillars are square, 10, 20 and 40-μm wide and 80-nm thick, as verified by the Alpha-Step IQ Profilometer. Figure 4.2(a) shows the thickness profile measured by QPI using a 20x/0.3 NA phase contrast objective of 20-μm wide pillars. The thickness is obtained from the phase measurement ϕ_m using $h(\mathbf{r}) = (2\pi/\lambda)(n_{\text{quartz}} - n_{\text{air}})\phi_m$, where the refractive indices of quartz and air are $n_{\text{quartz}} = 1.545$ and $n_{\text{air}} = 1$ at a mean wavelength of $\lambda = 574$ nm. The hfQPI image, $\phi^\dagger(\mathbf{r})$, is

obtained using Eq. (4.5) and converted into the thickness map as shown in Fig. 4.2(b). It can be seen that the negative thickness area surrounding the pillars in Fig. 4.2(a) is eliminated in Fig. 4.2(b). Also, the thickness of the reconstructed pillars converges to our expected value of 80 nm. To test the limits of our method, we applied it to a variety of pillar sizes, using different magnifications. The performance of the reconstruction algorithm is characterized by dividing the area under the height profile through the center of the pillar to the expected area under perfect reconstruction, i.e., without the halo (see Appendix B, Section B.5).

We validated our method further by removing the halo from images of a mixture of polystyrene microbeads (Polysciences Inc.) with 3 different diameters ($1\mu\text{m}, 2\mu\text{m}, 3\mu\text{m}$) $\pm 5\%$ of refractive index 1.59. The beads were mixed in ethanol before being dispersed onto the surface of a cover glass and exposed to air for drying out for 15 minutes. At that point, immersion oil (Zeiss) with a refractive index of 1.518 was applied and a cover slip placed on top of the oil droplet to flatten it. Figure 4.2(c) & (d) show the original QPI phase map of the beads and the reconstructed phase map, respectively. From these images, for each diameter, the mean and standard deviation of the phase are extracted from 5 beads in the field of view. The phase values are then compared with the theoretical phase of $\phi_{\text{bead,max}} = (2\pi/\lambda)(n_{\text{bead}} - n_{\text{oil}})d_{\text{beads}}$, where d_{beads} are their known diameters. The measured vs. calculated phase values are displayed in Figs. 4.2(e) & (f). In Fig. 4.2(e), we show the measured phase values obtained from the original QPI image, while Fig. 4.2(f) shows the hfQPI image. It can be seen that the hfQPI phase matches very well the expected phase values across all dimensions of the beads.

4.7.3 hfPC of biological samples

We further tested our method on red blood cells. Figure 4.3(a) shows the original QPI image and Fig. 4.3(b) is the hfQPI image. Their phase cross-sections through 4 different cells are illustrated in Figs. 4.3(c)-(d), respectively. Using $n_{PBS} = 1.334$, $n_{hemoglobin} = 1.402$ [102], the phase values of 1.82 ± 0.14 radians from profiles in Fig. 4.3(d) estimate the thickness of these cells to be $2.2 \pm 0.17 \mu\text{m}$, which falls within the normally expected range [103].

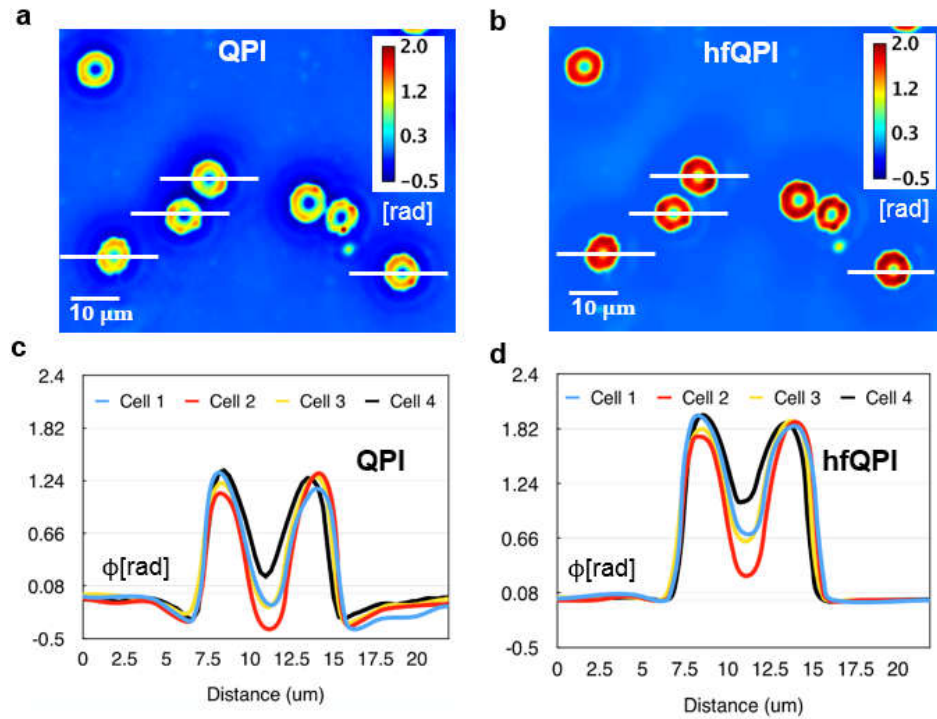


Figure 4.3 Halo removal of red blood cells. (a) & (b) Original QPI image and hfQPI image version of the same red blood cell sample measured under 40x/0.75 NA. (c) & (d) Phase profiles of several red-blood cells selected in (a) and (b), respectively.

Our halo correction method is applicable to a broad range of specimens, objective numerical apertures, and magnifications. For example, Fig. 4.4(a), (c) show fibroblasts and neurons imaged at 20x / 0.65 NA, respectively. Figure 4.4(e) shows HeLa cells at 40x / 0.75 NA and Fig. 4.4(g) neurons at 63x / 1.4 NA. Corresponding hfQPI images are shown in Fig. 4.4 (b), (d), (f), (h), respectively. For all cases, the halo is suppressed while maintaining the details in the original QPI, e.g., cell bodies, dendrites, axons and their terminals, etc., which

indicates that our method is scale invariant and universally applicable. The effects of halo correction can be accessed quantitatively by investigating the histogram of phase values (see the Appendix B, Section B.6)

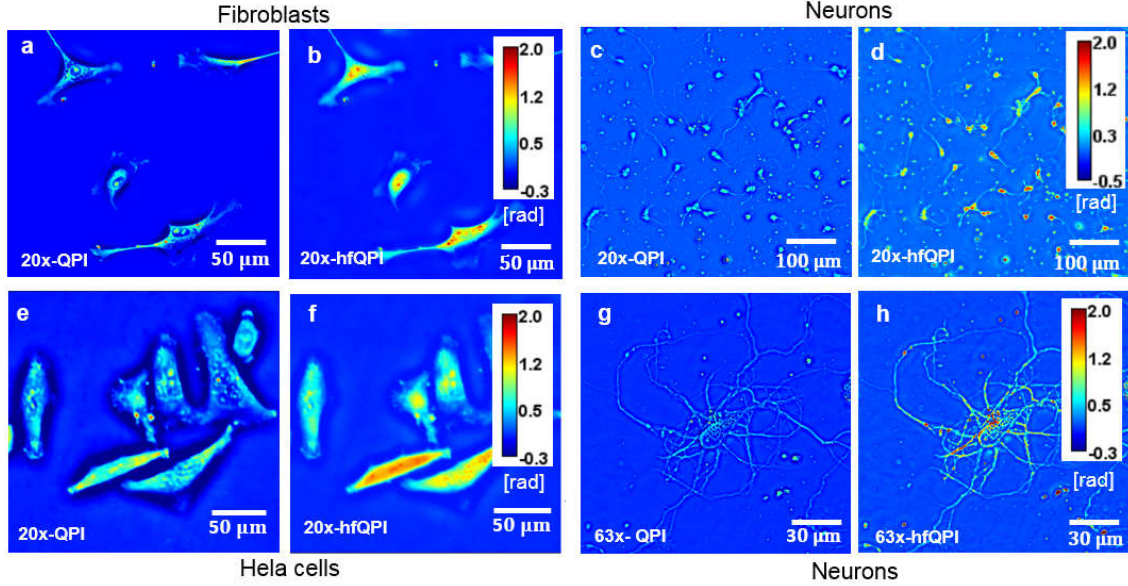


Figure 4.4 Original QPI and hfQPI images of different samples at different magnifications, as indicated.

4.7.4 hfQPI imaging of cell populations

Based on the quantitative phase information, we can successfully analyze entire cell populations and study their growth. With the halo artifact suppressed, automatic cell segmentation can be performed very efficiently. In the past, often image segmentation methods that relied on thresholding of the local intensity were confused by the negative values of the halo [95, 104, 105]. We show that hfQPI images can offer very accurate segmentation results for HeLa cells with only a few processing steps required. Here, we imaged a 30% confluence HeLa cell culture over 33 hours. A large field of view (FOV), $10.875 \times 8.125 \text{ mm}^2$, consisting of 25×25 individual frames (1392×1040 pixels each), was imaged with a $20\times / 0.3$ NA objective and a spatial sampling of $3.2 \text{ pixels}/\mu\text{m}$. Figure 4.5(a) shows stitched images of all HeLa at the first time step $t = 0$ minutes. The halo-removal procedure was applied to all images to obtain the corresponding hfQPI phase maps. The cells were segmented from the

hfQPI as described in Appendix B, Section B.7. It takes approximately 1.5 hours to segment the cells in all the 65,000 frames. All binary maps resulting from the segmentation are stitched together for each time step and shown in Fig. 4.5(b). Figures 4.5(c) & (d) show cell boundaries overlaid on the hfQPI images for the two regions indicated by the boxes in Figs. 4.5(a) & (b), respectively. It can be seen clearly that automatically detected cell boundaries align very well with the true boundaries of the cells from the phase image.

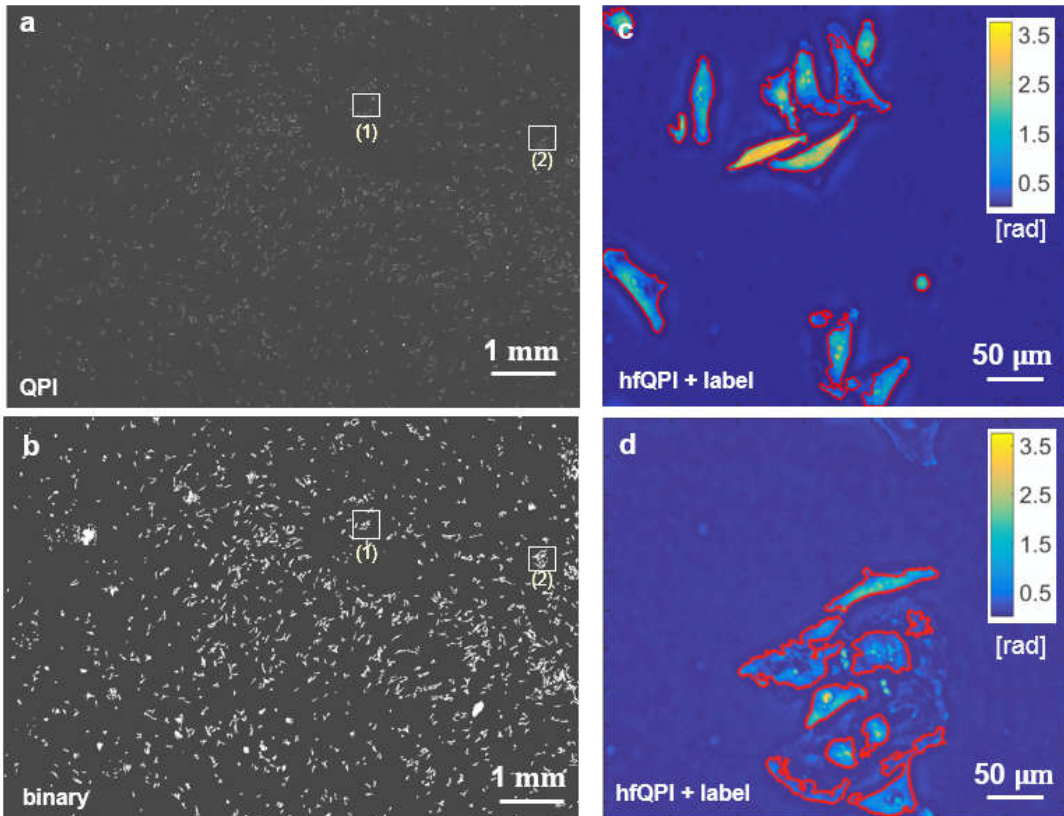


Figure 4.5 Automatic cell segmentation. (a) Stitching results of hfQPI images over a large FOV. (b) Stitching results of automatic binary segmentation. (c) & (d) Segmentation results overlaid on the hfQPI images of zoomed-in regions (1) & (2) in (a) & (b), respectively.

4.7.5 Cell growth study using QPI

In his seminal paper [106], Barer established that the dry mass density $\rho(\mathbf{r})$ is proportional to the optical phase ϕ , following the relation $\rho = \lambda\phi/(2\pi\gamma)$, where λ is the central wavelength

of the illumination and $\gamma \approx 0.2 \text{ ml/g}$ is the refractive index increment. We used this relation to determine the total dry mass of each single cell by integrating over its area. Figure 4.6(a) shows the relative dry mass of a HeLa parent cells (green curve) and that of its two daughter cells (red and blue curves) over 35 hours with a time step of 32 minutes.

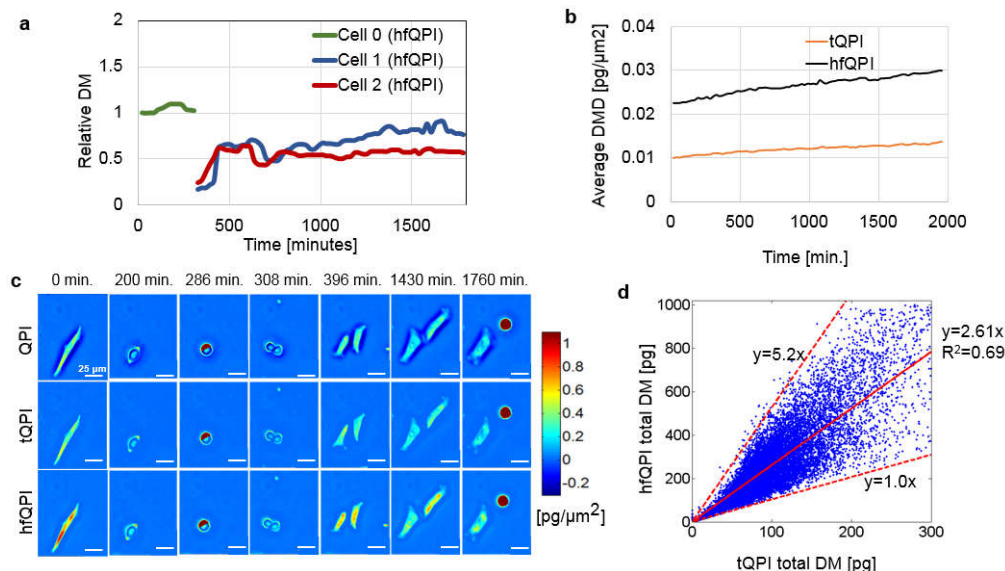


Figure 4.6 HeLa cell mass measurement. (a) Different growth curves from a parent and two daughter HeLa cells measured using a 20x/0.3 NA objective over 32.6 hours. Each growth curve shows the total dry mass of a single HeLa cell over time. When the parent cell divides, two new curves are generated for the daughter cells. (b) Measured averaged dry mass densities obtained from the tQPI images and the hfQPI images over time. (c) Each row shows seven measurements of the dry mass density at different time points in (a). The first row contains the raw QPI images. The middle row shows tQPI images. The bottom row is for hfQPI images. (d) Scatter plot of the total dry mass of all several cells obtained from tQPI images (horizontal axis) and the hfQPI images (vertical axis) using automatic segmentation. The lines show the maximum slope, minimum slope and fitted slope using linear regression relations between these two quantities.

The dry mass values are normalized to the initial mass of the parent cell at time $t=0$ minutes to obtain the relative dry mass change. These data are obtained from raw dry mass after being smoothed over time using a window size of three frames. Figure 4.6(b) shows the average dry mass densities computed over the full field of view as a function of time. This quantity is obtained by dividing the total mass of all cells by the total area covered, for each

time point. The red profile is the average dry mass density calculated using raw QPI images thresholding out the negative phase values while the blue one is obtained using the hfQPI images. It can be seen that the ratio of these two densities is approximately 2.5 throughout the entire time lapse. Figure 4.6(c) illustrates original QPI images, thresholded QPI (tQPI) images and hfQPI images of these cells at different time points. The correlation between the dry mass obtained from tQPI and hfQPI images is shown in Figure 4.6(d). Each point in this scatter plot corresponds to a single cell at one time-step. The horizontal coordinate is the total dry mass from the tQPI images while the vertical one is the total dry mass from the halo-free images. All dry mass values below 25 pg and above 500 pg from the tQPI images are eliminated from the analysis to reduce errors due to debris. It can be seen that the dry mass obtained from hfQPI and tQPI images can be described by a linear relation $\Delta M_{hfSLIM} = \alpha \Delta M_{tSLIM}$ with $1.0 \leq \alpha \leq 5.2$ and a standard deviation value of 0.82. The reason for α not being a constant can be explained using Fig. 4.6(c). Each column of this figure corresponds to a different time in a cell cycle. It can be seen that the effect of the halo is not the same at all times. While the halo can be seen clearly when the cell is in interphase (e.g. $t=0$ minute, $t=396$ minutes, and $t=430$ minutes), the halo almost disappears when the cell balls up during mitosis ($t=1760$ minutes). The halo-removal correction works on all of these cases. However, the amount of correction applied to cells in the interphase is larger than that in mitosis. For $t=1760$ minutes, the mitotic HeLa cells before and after correction are very similar to each other. Therefore, the total dry mass from the halo-free QPI image and that from the tQPI image will have $\alpha \approx 1$. In contrast, in column 1 of Fig. 4.6(c), the corrected QPI image gives a phase value approximately twice that in the tQPI image. As a result, this case will give a ratio $\alpha \geq 2$. Using linear regression fitting, we obtain $\alpha = 2.61 \pm 0.82$ and the R^2 coefficient of 0.69. This fitting slope only varies slightly over different regions. For example, $\alpha = 2.53 \pm 0.81$, 2.64 ± 0.83 , 2.69 ± 0.80 , when the original mass from tQPI is in $[0,100]$, $[100,200]$, $[200,300]$ pg, respectively.

Finally, we analyzed the dry mass distribution of each cell. Figures 4.7(a) & (b) show maps consisting of dry mass histograms over 88 time points (one column per time point). The cells were segmented automatically. All regions with areas less than 5,000 pixels ($488.28 \mu\text{m}^2$) are excluded from the analysis to lower the error due to small debris. Figure 4.7(a) is obtained from tQPI images, while Fig. 4.7(b) is from hfQPI images. Each histogram consists of 200 bins. It can be seen that, over time, the total number of counts increases due to continuous cell division. The cells become more diverse in dry mass, resulting in a broadening of the histogram distribution toward the areas of larger and smaller dry masses. Figures 4.7(c) & (d) are normalized versions of Figs. 7 (a) & (b), respectively, to the number of cells at each time point. Therefore, they are equivalent to the probability density distribution of the single cell dry mass at each time. The mean and standard deviation of the cell dry mass of Figs. 4.7(c) & (d) are shown in Figs. 4.7 (e) & (f), respectively. It can be seen that although there is more variation in the population, the average values of the dry mass only slightly reduce for the tQPI and essentially stay constant for the hfQPI over time. The standard deviation values are approximately the same over time for both cases.

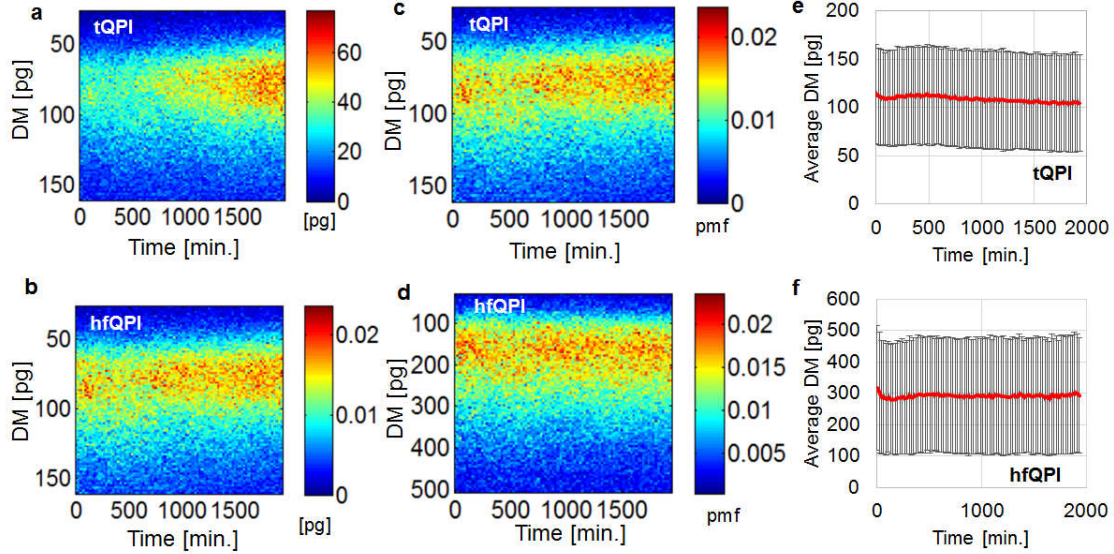


Figure 4.7 (a) & (b) Total dry mass histogram of all cells in the FOV obtained from the tQPI and hfQPI images over time, respectively. Each column corresponds to one time-step. Each row corresponds to bin of the dry mass histogram. (c) & (d) Normalized version of (a) & (b) to the number of cells, respectively. Therefore, they show the probability mass function of a single cell. (e) & (f) The mean and the standard deviation of the mass over time obtained from tQPI and hfQPI images, respectively. DM: single cell dry mass.

4.8 Summary

In this chapter, we introduced a new method to remove the halo artifact from the classical phase contrast microscopy. Our method combines highly sensitive light interferometry, theoretical optics, and computational algorithms. Our approach is able not only to correct for this artifact but also to produce quantitatively the phase value introduced by the object, which is valuable in studying various problems, such as nanoscale profilometry of materials and quantitative cell biology. We tested our method on various control nanofabricated samples as well as biological samples e.g. neurons, red blood cells, and HeLa cells under different magnifications. Our results showed that the dry mass of HeLa cells can be obtained directly from hfQPI images without the need to scan through the full volume of the cell. By scanning very large fields of view over a period of 35 hours and combining with an algorithm for automatic cell segmentation, the dry mass density distribution for the whole population was obtained easily

and quickly. Interestingly, we found that the relative dry mass obtained directly from tQPI images and that from the hfQPI images are strongly correlated with a linear proportionality constant of 2.6. Therefore, one can obtain a good estimate for the growth curve directly from tQPI images. However, for high accuracy, hfQPI must be used instead. We anticipate that various studies of cell functions using phase contrast microscopy can benefit from these results.

As a label-free method, PC microscopy can be applied to imaging live cells nondestructively over broad time scales. This ability is not limited by photobleaching and phototoxicity commonly associated with fluorescence microscopy. At the same time, PC lacks specificity. Therefore, we envision that PC and fluorescence techniques will co-exist and corroborate the advantages of specificity and noninvasiveness. It is particularly valuable that our optical system operates on the same optical path as the fluorescence channels, which makes combining the two channels very practical.

CHAPTER 5: PROSTATE CANCER DIAGNOSIS USING QPI

5.1 Introduction

Prostate cancer is the second leading cause of cancer-related death among men in the United States [107, 108], after lung cancer. In 2015, 220,800 men were diagnosed with prostate cancer, accounting for 26% of the total number of new cancer cases, and 27,540 men are projected to eventually die from the disease [108]. Prostate health is evaluated using different formats including a detailed medical interview, a physical examination with digital rectal examination (DRE), or a prostate-specific antigen (PSA) blood test. Abnormal DRE results or PSA levels above the normal value of 4 ng/ml might lead to a prostate biopsy to confirm whether these abnormalities are due to cancer [109]. The excised tissue samples are fixed using formalin and then embedded in paraffin wax, which is sectioned into thin slices using a microtome. These sections are then deparaffinized and stained with hematoxylin and eosin (H&E) dye for microscopic examination by the pathologist. If the pathologist suspects the presence of cancer, based on the absence of the myoepithelial or basal cell layer, cancer severity is assessed using the Gleason grading system [110, 111]. The Gleason score is the sum of two Gleason grades corresponding to the two most prominent disease patterns present in the examined tissue. The Gleason grade, which typically ranges from 3 to 5, measures the degree of glandular separation and, thus, cancer aggressiveness. The glands in Gleason grade 3 carcinoma are smaller and more closely packed than in normal prostate, resulting in a reduced separation between them. In Gleason grade 4, the glands display fusion, sometimes creating what appears as large glands containing multiple lumens, also known as the *cribriform* pattern. In Gleason grade 5, glands are very poorly differentiated with sheets of epithelial cells seen in the stroma, which is connected with poor disease outcome. Although the Gleason grading system has undergone a

few revisions since it was first established, it continues to remain a strong prognostic indicator. The Gleason score is linked to several clinical endpoints, including progression to metastatic disease and patient survival [112]. It also influences the treatment decisions made by the physician [113]. Accurate discrimination between Gleason grade 3 and 4 is critical as it triggers the switch between active surveillance and aggressive treatment [114].

Although the diagnosis of prostate biopsies by a trained pathologist is currently considered to be the “gold standard”, the technique suffers from several shortcomings. First, for Gleason grading, the samples are stained using hematoxylin and eosin (H&E), aiming to target different components in the prostate biopsies, e.g., nuclei, cytoplasm, nucleoli. The protein-rich regions, basic in nature, are stained pink while the acid-rich regions become blue. Other markers with better specificity have also been developed [115-117]. The need for using these markers stems from the fact that many biopsies are nearly transparent under bright-field microscopy inspection. Therefore, exogenous factors must be introduced to enhance the contrast. This process takes time, requires expertise and sacrifices the intrinsic properties of the sample. Furthermore, the staining poses a significant challenge for improving the throughput of the system using modern computing algorithms. An experienced pathologist can handle the variations in the concentration of the dye, staining skill, and color balance. However, it requires additional processing and assumptions before inputting to a computer to automate the process. Significant effort has been spent to produce reliable automatic Gleason grading based on the histological H&E images. Such efforts can be divided into two categories: classification-based and segmentation-based techniques. Methods in the first group use various features from stained images to produce Gleason scores without the need for image segmentation. These features include textures from H&E images [118] and multi-spectra images [119]. Methods in the second group produce a Gleason score in two stages. In the first stage, label maps of the biopsies are produced from the H&E images. Then, morphological

features are extracted from these maps. Finally, subsequent classifiers are deployed to produce the final Gleason grade. Naik et al. [120] build statistical models of the likelihood for the class of a pixel given its color and location in the training set. In [121], Nguyen et al. use the (L, a, b) color space and various constraints on the relative arrangements of tissue region sections to refine the segmentation map. To achieve automatic histology, variables, such as exposure time, magnification, illumination spectra, dye concentration, must all be the same, which may be impractical. Furthermore, there is no universal agreement on how the stained image should be normalized and what the correct normalization should be [122].

Understanding these obstacles, several groups have tried to do diagnosis from label-free slices. Muller et al. [123] used the optical attenuation coefficient measured using needle-based optical coherence tomography (OCT) as a tool for detection of prostate cancer. They showed that the optical attenuation coefficient was significantly higher in malignant tissue compared to benign prostate tissue. Uttam et al. [124] used optical path length information to quantify the depth-resolved density alteration of the nuclear architecture as a tool for early prediction of cancer progression. Spectroscopy methods have also been used to examine the biochemical information of the tissue at a molecular level for different pathologies in vitro. In Ref. [125], the authors demonstrate the use of Raman spectroscopy to differentiate between benign samples, benign prostatic hyperplasia (BPH) and prostatitis, from prostate cancer at an accuracy of 86%. Combining Fourier transform infrared spectroscopy (FTIR) with bright-field microscopy, Kwak et al. [126] improved the accuracy of automatic segmentation and demonstrated an AUC of at least 0.97 in a binary classification problem between cancer vs. non-cancer cases. It was later shown that FTIR can be used to provide a better prediction of prostate cancer recurrence, compared to two widely used tools, Kattan nomogram and CAPRA-S [127]. However, the spectroscopic information in FTIR is obtained at the expense of spatial resolution (typically above 10-15 microns) and extremely slow acquisition speed.

Recently, quantitative phase imaging (QPI) [8, 20, 21, 32, 33, 128, 129] has emerged as a new, valuable tool to render high contrast of unlabeled transparent samples. The contrast in QPI is due to the real part of the refractive index of the sample which is retrieved through interferometric settings. Therefore, the measurement is very robust to change in the illumination condition, e.g., illuminating variation, allowing high repeatability and seamless translation across measurement sites. Previously, many QPI methods utilized laser illumination due to a requirement for long coherence length in *traditional* interferometry. The laser illumination generates a random speckle pattern [36], which suppresses structural details of the biopsy. Recently, a combination of white-light illumination and *common-path* interferometry [20, 32-34] has solved this problem. This method, referred to as spatial light interference microscopy (SLIM) [32], allows the refractive index information to be captured at a diffraction-limited resolution with nanoscale accuracy and excellent temporal stability. In [18], it was reported, for the first time, that QPI has the potential to classify cancerous areas vs. benign areas in prostate biopsies, using the mean and median of the phase distribution as the feature. Furthermore, light scattering parameters measured in the prostate stroma using QPI have been used to predict the aggressiveness of intermediate grade prostate cancer [130].

Here, we introduce a combination of advanced machine learning algorithms with SLIM label-free imaging and describe the first label-free tissue scanner with automatic prostate cancer diagnosis. The SLIM system is able to image at 12.5 SLIM images per second, at 40x magnification and 4 megapixels/frame. Using a tissue micro array (TMA), containing more than 300 cores, we segmented different regions from prostatectomy samples into multiple classes (gland, stroma, and lumen) with high accuracy. Segmented label maps are further used to obtain several morphological features of the glands of the cores, e.g., distortion, variation of gland areas etc. One of our advantages over other techniques is the ability to extract physics-related features, e.g., stroma anisotropy, which characterizes the directional dependence of the

light scattering when it propagates through stromal areas of the tissue. Using these features, we were able to separate regions with Gleason grade 3 and Gleason grade 4 with an AUC of 0.87.

5.2 Tissue Micro Array (TMA) description

The TMA is provided by the Co-operative Prostate Cancer Tissue Resource (CPCTR) from the University of Illinois at Chicago – College of Medicine. The TMA consists of 368 prostates cores (one core per patient) with several diagnosis results including normal, benign prostatic hyperplasia (BPH), high-grade prostatic intraepithelial neoplasia (HGPIN) and Gleason scores varying from 2+2 to 5+5. After being deparaffinized, unstained cores were first imaged using SLIM under a 40× magnification. The phase images are stitched together to generate one high-resolution image per core. Each such image has 10,000 x 10,000 pixels with a pixel ratio of 14 pixels per micron. Afterwards, the cores were stained with hematoxylin and eosin and scanned by a bright-field tissue scanner (results of all cores can be found in Fig. 5.1).

Figure 5.2 displays three H&E 5.2(a) and SLIM 5.2(b) images of three cores in the TMA. In order to provide ground truth for automatic diagnosis, different regions of interest (ROIs) in each core are studied and color-coded by a certified pathologist for their diagnosis using H&E images. Here, green color indicates normal areas, red HGPIN, and blue tumors. Each blue region is further annotated for Gleason grade 3, 4 or 5 (see core examples in Fig. 5.3). Based on these annotations, corresponding regions in the SLIM images are extracted and further used for the automatic diagnosis.

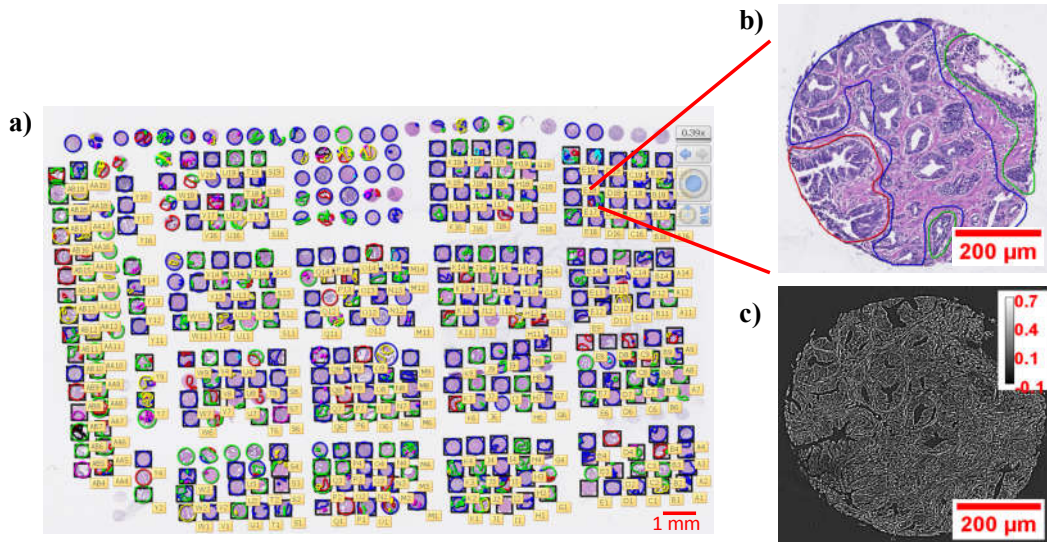


Figure 5.1 H & E image of the whole TMA with diagnosis results. (a) H&E image of the whole TMA slide consisting of 368 cores. (b) A zoomed-in H&E image of a prostate core. Annotations on the image were performed by a trained pathologist. The region highlighted in green represents normal glands, the region in blue is Gleason grade 3 prostate cancer glands, and the region in red corresponds HGPIN. (c) A zoomed-in SLIM image of the same core as in (b), obtained prior to staining. Morphological features in the H&E image are recapitulated by SLIM.

5.3 Automatic diagnosis framework

In order to obtain the automatic diagnosis from SLIM images, we use an approach summarized in Fig. 5.4. First, texture-based features are extracted for each pixel in the SLIM image and passed into a classifier to do automatic segmentation based on pixel classification. Each pixel is assigned one of three classes (gland, stroma, and lumen). Second, using the label map obtained from the previous step, morphological and phase-based features are evaluated for all glands in the current field of view and its surrounding stroma. These features are later passed into a subsequent classifier to produce diagnosis results, as described below.

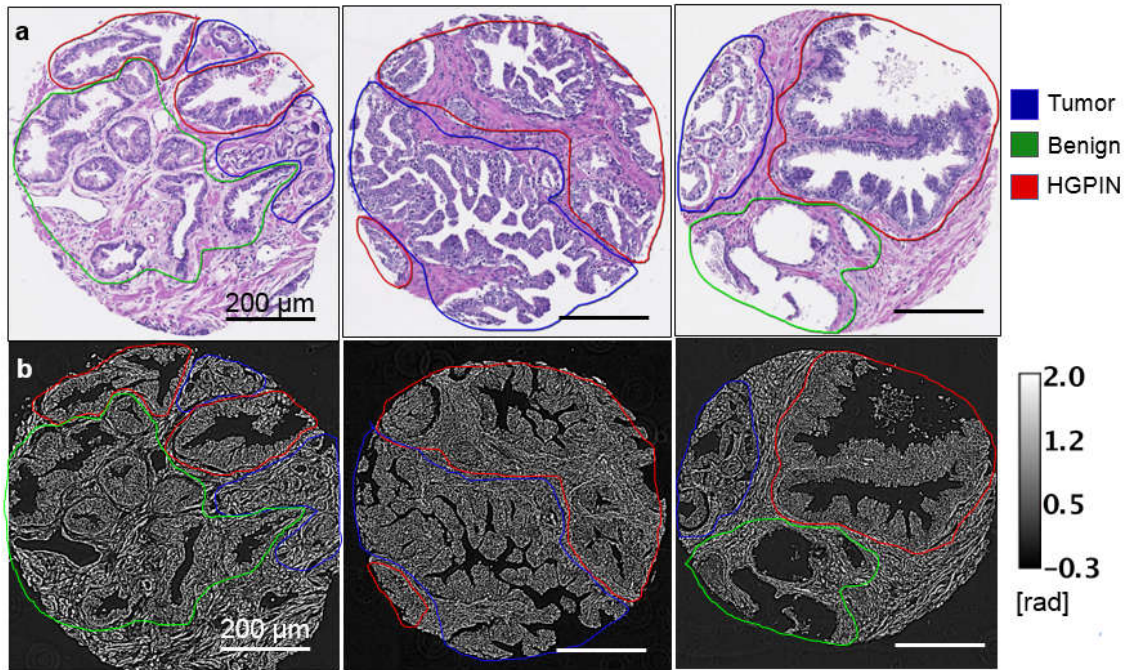


Figure 5.2 H&E images vs. SLIM images. (a) H& E images of 3 cores in the TMA. The H&E images were used by a pathologist for Gleason grading. Each core in the training data set includes an annotation of diagnosis results. (b) Corresponding SLIM images of those in (a).

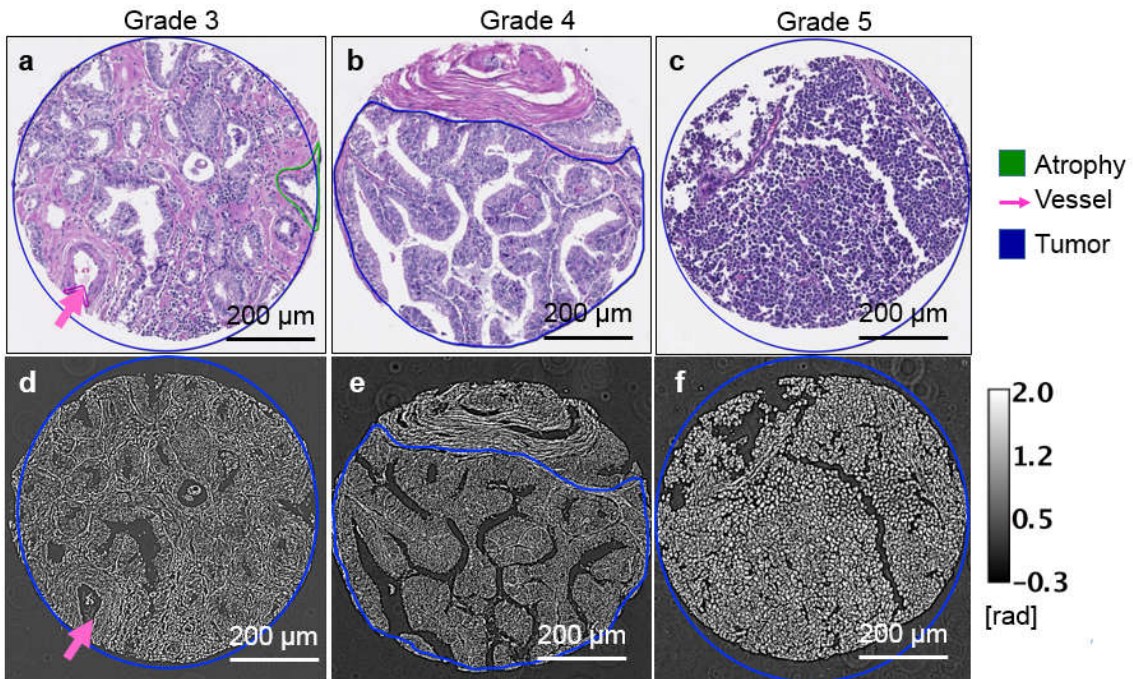


Figure 5.3 H&E vs. SLIM. (a) - (c) H&E images of 3 cores in the TMA that have Gleason grade of 3, 4, and 5.

(d) - (f) Corresponding SLIM images of these cores. Gray scale bar represents phase shift in rad.

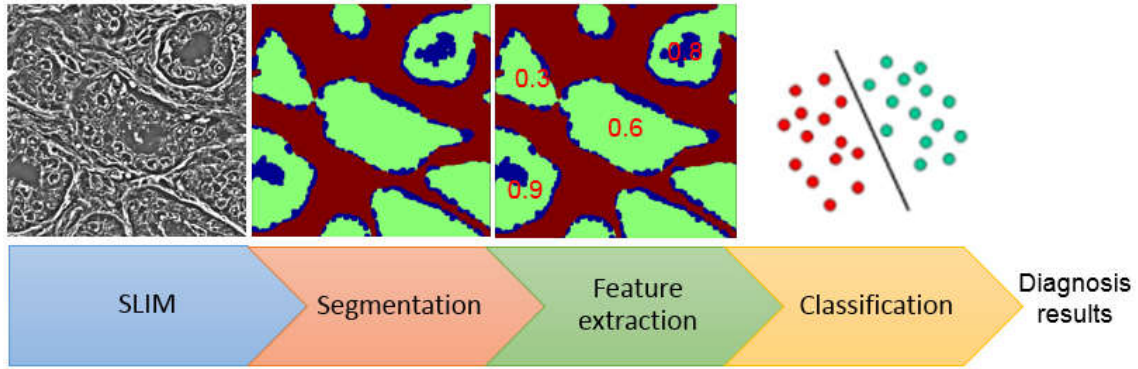


Figure 5.4 Automatic diagnosis scheme illustrating the steps from the input SLIM image to the diagnosis result.

5.3.1 Feature extraction from phase images

In order to capture the texture expression of the biopsies, we use the *texton* framework proposed by Julesz [131] and later expanded by Leung and Malik [132, 133]. The framework has demonstrated great success in solving several computer vision problems, e.g., material classification and characterization [132-135], thanks to its ability to accurately imitate the mechanism of human textural perception [131, 136, 137]. In our work, the framework is used to train a texton dictionary (Fig. 5.5(a)) from a set of training images and extract a feature vector for each pixel. More details on training the texton dictionary are given in Appendix C, Section C.1. In feature extraction, given an input image, one wants to obtain a set of pixel descriptors for the classifier. This feature extraction can be done by first calculating filter responses of the input image to all the kernels in the filter bank. Then, vector quantization is applied to associate the filter response at each pixel to the closest texton in the trained dictionary. Finally, a weighted histogram counting how many times each texton has appeared in a window, surrounding each pixel (Fig. 5.5(b)), is used as pixel descriptors.

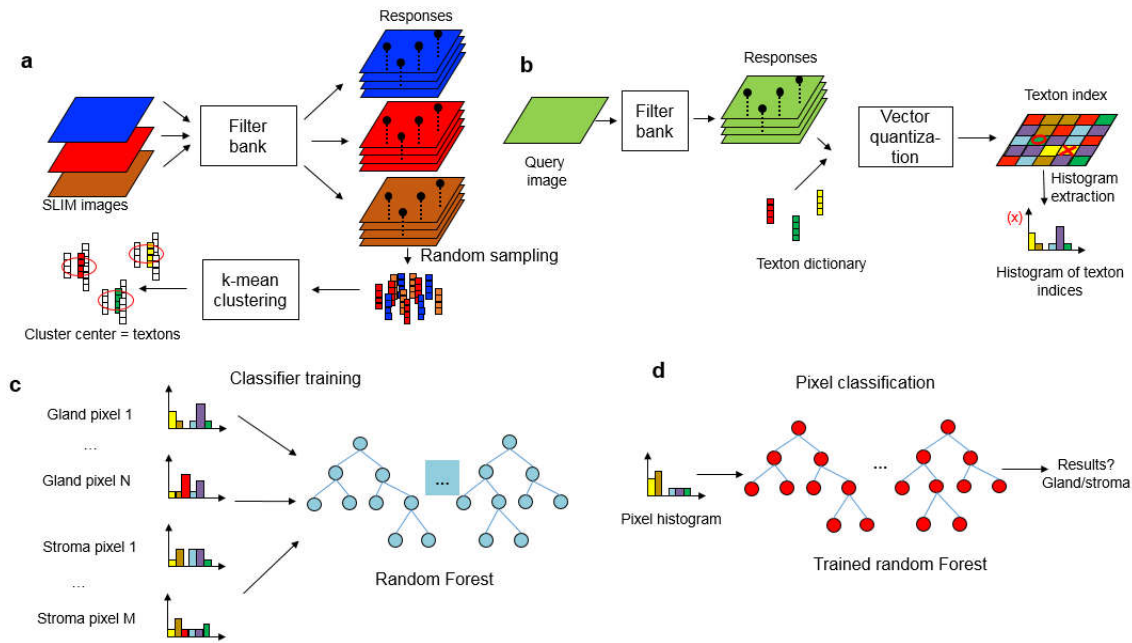


Figure 5.5 Feature extraction from SLIM images. (a) Extracting the texton dictionary from a training set of SLIM images. (b) Feature extraction using vector quantization and the trained dictionary in (a). (c) Pixel classifier training using pixel descriptor obtained in (b). (d) Pixel classification using a trained classifier in (c).

5.3.2 Random forest for automatic segmentation

In order to perform image segmentation, we use a random forest (RF) classifier, which is a method introduced by Breiman [138-140]. We use the RF to classify each pixel in the image into one of three classes, i.e., epithelial gland, connecting stroma, and lumen. Lumen pixels are classified first based on the proximity of their phase values to that of the background. Then, remaining pixels are classified into either gland or stroma. The classifier consists of an ensemble of T de-correlated decision trees, each of them independently trained on a different subset of all histograms obtained by randomly sampling the training dataset with replacement. This sampling technique is commonly known as *bootstrapping*. Also, for each tree, a technique called “feature bagging” is used, in which only a subset of indices is used instead of all indices. Therefore, the correlation of the trees and the variance of the prediction are reduced [141]. More details on training the random forest (Fig. 5.5(c)) and using it for pixel classification (Fig. 5.5(d)) are given in Appendix C, Section C.2.

Figure 5.6 shows automatic segmentation results overlaid with the SLIM images. It can be seen that the label map has very good correlation with the H & E images. Figure 5.3 shows other segmentation examples, with H & E and SLIM images of increasing Gleason grade (from 3 to 5). Their automatic segmentation results are further shown in Fig. 5.7.

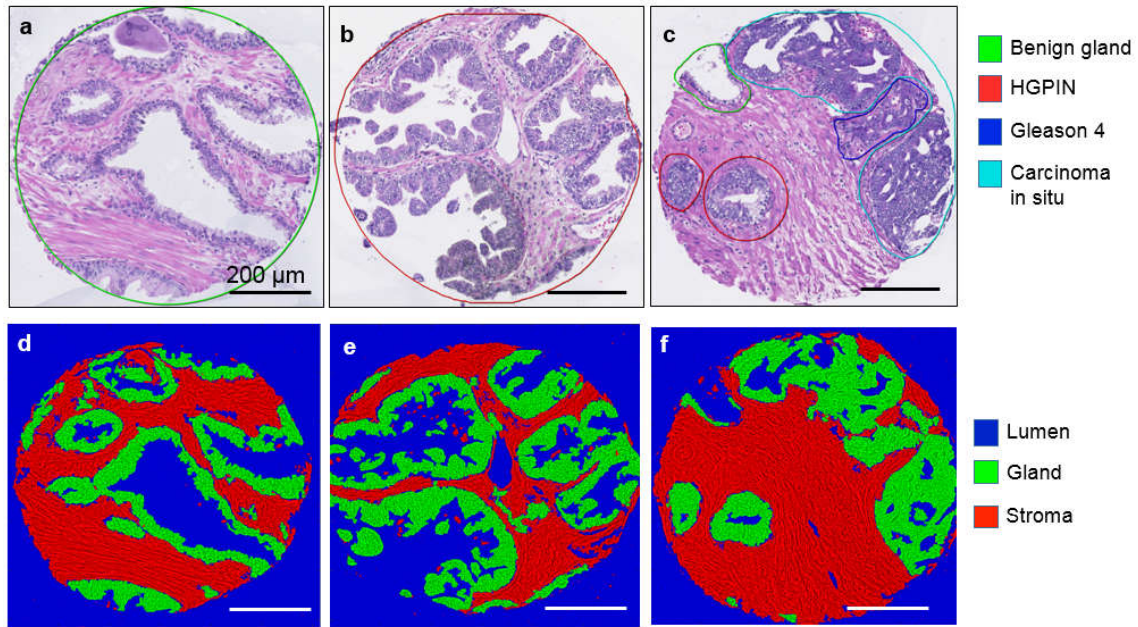


Figure 5.6 H&E vs. automatic segmentation. (a) - (c) H&E images of three cores. (d) - (f) Corresponding automatic segmentation results overlaid on the top of the SLIM images of the cores.

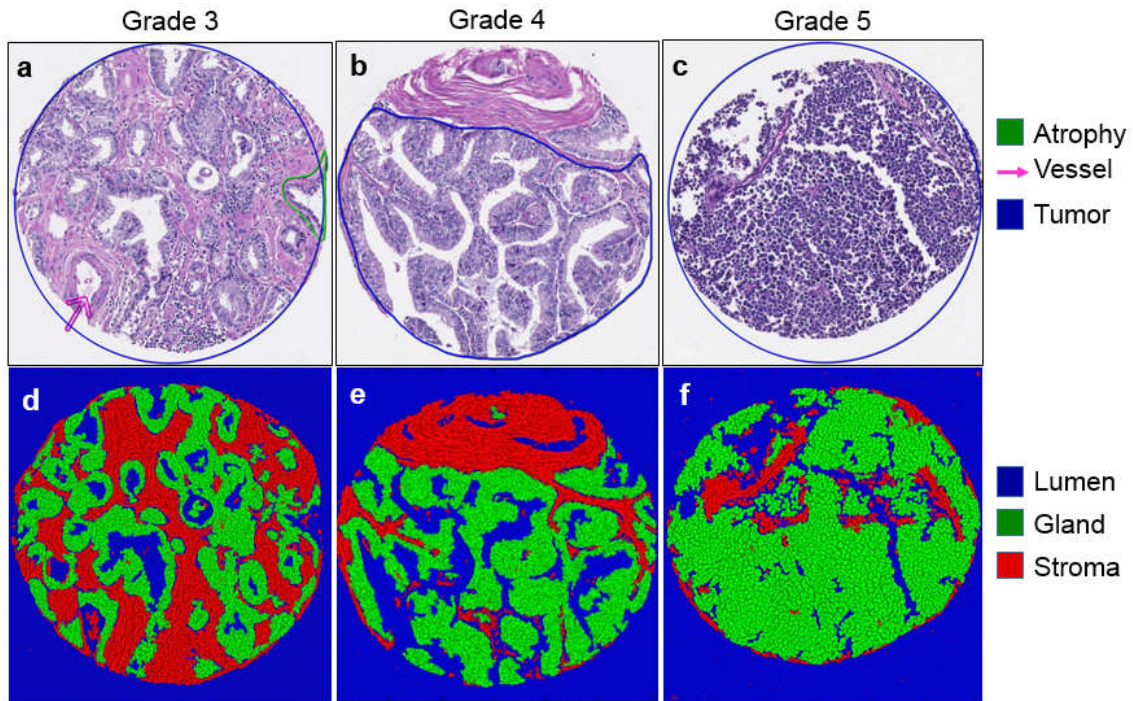


Figure 5.7 H&E images (top row) and automatic segmentation results (bottom row) of three cores in the TMA with increasing Gleason grades.

In order to quantify the performance of our segmentation, we summarize in Figure 5.8(a) all receiver operating characteristic (ROC) curves for the segmentation of different diagnosis groups. Figure 5.8(b) shows the corresponding area under the curve (AUC) values. The ground truth for ROC evaluation is created by manually labeling glandular and stromal regions directly on the SLIM images after validating them with H & E images. In the non-cancer cases, the AUC is at least 0.97, which indicates that gland and stroma pixels are classified with high accuracy. Meanwhile, in the malignant cases, as cancer progresses to higher grades, e.g., from 3+3 to 5+5, the AUC reduces from 0.98 to 0.87. This result can be explained by the fact that more glandular distortions and deformations are observed at higher grades, which leads to a reduction in the discrimination between stroma and glands. The Gleason score 5+5 tissue shows no glandular presence and has individual epithelial cells embedded in the stroma. Therefore, it is not surprising that the classifier has the smallest AUC in this group. However, these high grades are very easily diagnosed by the pathologist and,

thus, do not represent our main focus. Using these segmentation results, we solve the automatic Gleason grading problem, with particular emphasis for discriminating between grades 3 and 4.

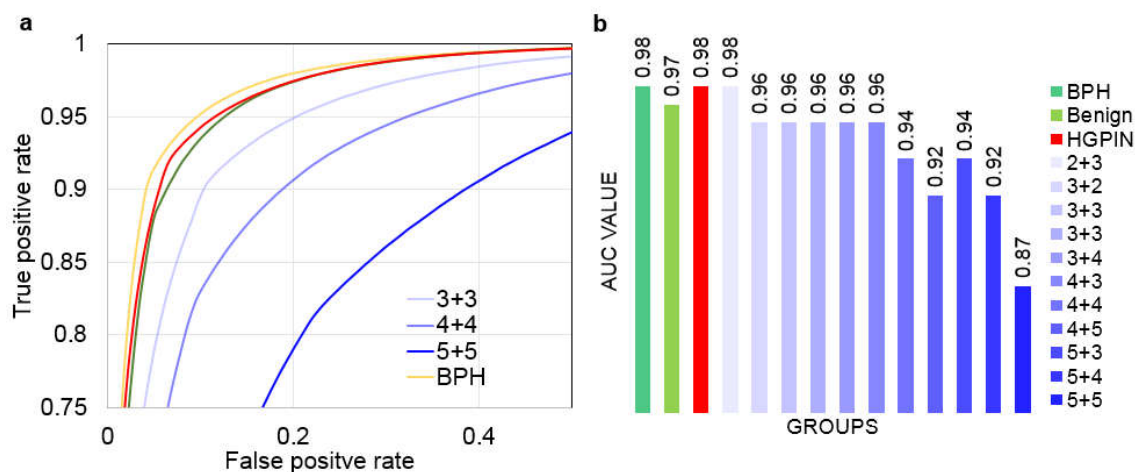


Figure 5.8 Automatic segmentation performance. (a) ROC curves for classifying gland vs. non-gland pixels for all diagnosis groups. It can be seen that the accuracy reduces when going to higher Gleason grade. However, the AUCs are still good enough to ensure reliable diagnosis results. (b) Bar plot of AUC values of the ROC curves for all diagnosis groups.

5.4 Automatic Gleason grading

In order to generate the ground truth for automatic Gleason grading, different regions inside each core were first manually marked and graded by a trained pathologist. Figure 5.1 shows an example of markup results for all cores: 129 regions with Gleason grade 3, 92 regions with grade 4 and 75 regions with grade 5. Since Gleason grades 2 and 5 are rarely diagnosed, we study the automatic diagnosis problem of differentiating Gleason grade 3 vs. Gleason grade 4. It has been shown by Allsbrook et al. [142] that grading 3 vs. 4 has a reproducibility problem due to inter-observer variation. For example, the authors report an experiment where 38 biopsies with known “consensus” Gleason grade were sent to 41 pathologists to measure inter-observer variability. The result was that Gleason grade 4 was under-graded by 21%. Furthermore, there was consistent under-grading of Gleason scores of 5-6 (47%), 7 (47%) and

8-10 (25%). Clearly, a computer-driven, unbiased procedure for grading is a potential way to tackle this challenge.

Figure 5.9 shows five different types of features extracted from each region. These features include mean glandular distortion, the fusing ratio of glands, the mean number of lumen areas per gland, coefficients of variation for gland variation, mean stroma anisotropy. Other features include the maximum number of lumen areas, the median of the glandular distortion, median of stroma anisotropy, and the mean circularity. More details on these features can be found in Appendix C, Section 0. They are designed to measure the distortion, area homogeneity of the glands, and the amount of gland fusion. These metrics are often used by pathologists for Gleason grading [111, 112, 143]. Each ROI is characterized by a feature vector of nine elements. Diagnosis grades from pathologists are used as ground truth for automatic diagnosis. After computing the feature vectors ROIs, we train a generalized linear model classifier for classifying the Grade 3 vs Grade 4 ROIs.

The performance of the classifier is shown in Fig. 5.10 in terms of the ROC. The curve has an AUC value of 0.87. Note that this error is well within that for inter-observer variability reported by Allsbrook et al. (44). It can also be seen from the curve that in order to detect Gleason grade 4 at an accuracy of 90%, the false positive rate will be approximately 50%. The inset presents a horizontal bar plot of AUC values when the classifier is trained separately on each individual feature. The two largest AUC values are obtained on the coefficient of variation for the areas of the glands and the fusing ratio. These results demonstrate that label-free imaging and machine learning can provide an objective alternative to pathology, even in the case of difficult tasks, such as classifying Gleason grade 3 and 4.

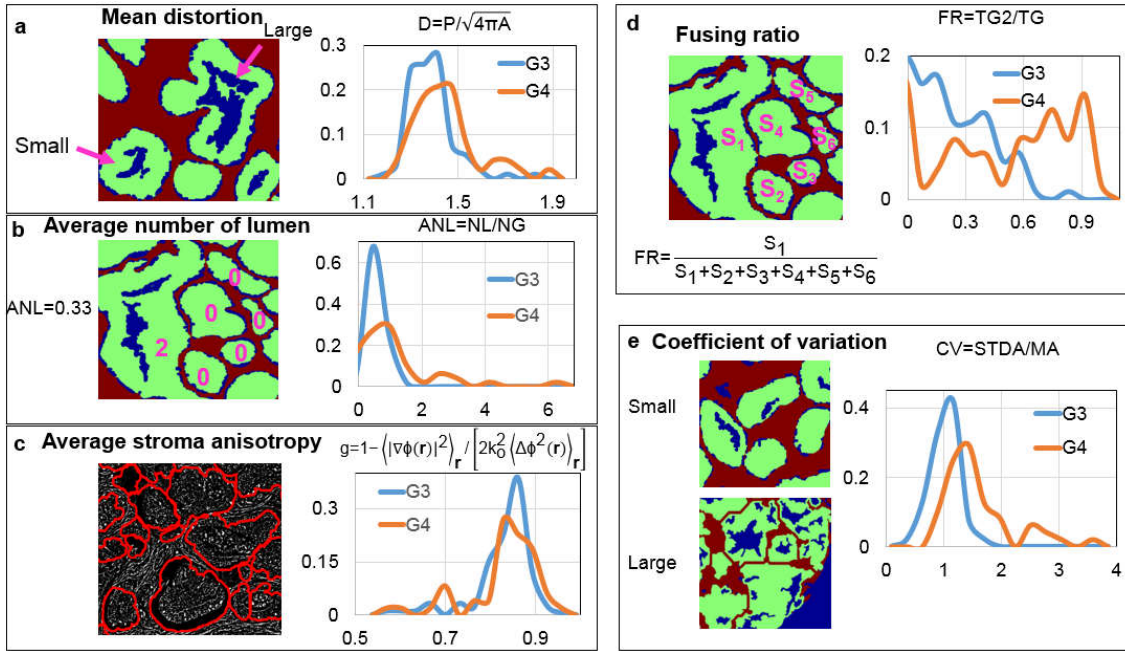


Figure 5.9 Feature extraction for automatic diagnosis. Each subfigure shows a feature, how it is calculated and the distributions of the feature values for G3 (blue) and G4 (orange). (a) Mean distortion feature: D , mean distortion of a gland, P , perimeter of a gland, A , area of a gland. (b) Average number of lumens feature: ANL , average number of lumens, NL , number of lumen, NG , number of glands. (c) Average stroma anisotropy feature. (d) Fusing ratio feature: FR , fusing ratio, $TG2$, total areas of glands with at least 2 lumens, TG , total area of all glands in current field of view. (e) Coefficient of variation feature: CV , coefficient of variation, $STDA$, standard deviation of areas of all glands, MA , mean of the areas of all glands.

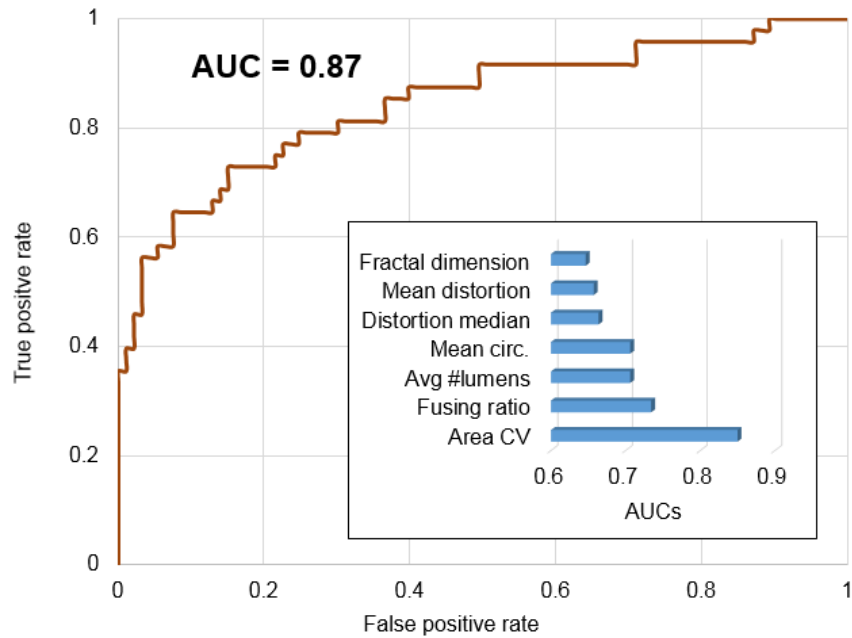


Figure 5.10 ROC curve for classifying regions with Gleason G3 vs. Gleason G4. These features are extracted from all glands within the ROIs. Diagnosis results from pathologists are used as ground truths. The inset shows AUCs for classification based on individual features.

5.5 Cancer vs. non-cancer classification

Next, we study the cancer vs. non-cancer automatic diagnosis problem. The problem is complicated by an introduction of an intermediate class named high-grade prostatic intraepithelial neoplasia (HGPIN), in which abnormal cells do not look like they are growing into other parts of the prostate. However, the risk of getting prostate cancer is higher when HGPIN is found on more than one biopsy. Figure 5.11 shows a core with three different regions. Regions 1, 2, 3 are benign, HGPIN and tumor, respectively.

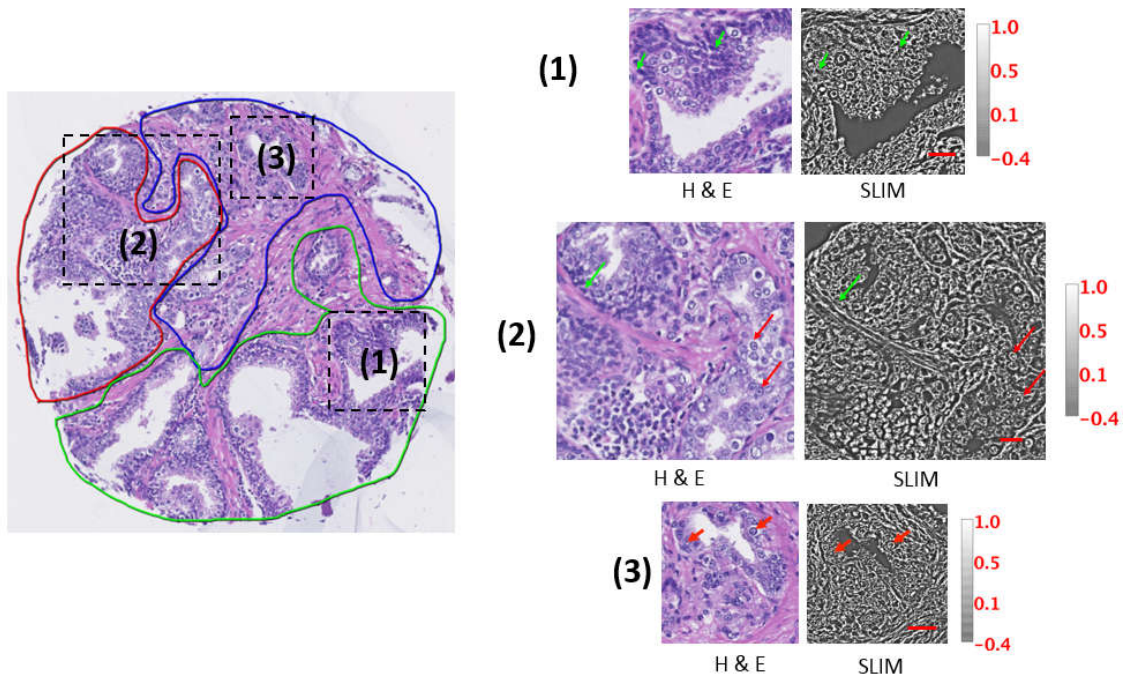


Figure 5.11 A core with three different diagnosis results for three ROIs, color-coded as HGPIN (red), tumor (blue), and normal (green). The subfigures on the right are their H&E and SLIM images. The red arrows point to prominent nucleoli. The green arrows point to basal cells. Note that these signatures can also be spotted in the SLIM images thanks to its high spatial resolution. Scale bar: 30 μ m.

To discriminate between cancer/non-cancer cases, pathologists use the existence of a thin layer of basal cells surrounding prostate glands. Glands lined by basal cells are normal. Otherwise, they are malignant. See Fig. 5.12 for an illustration.

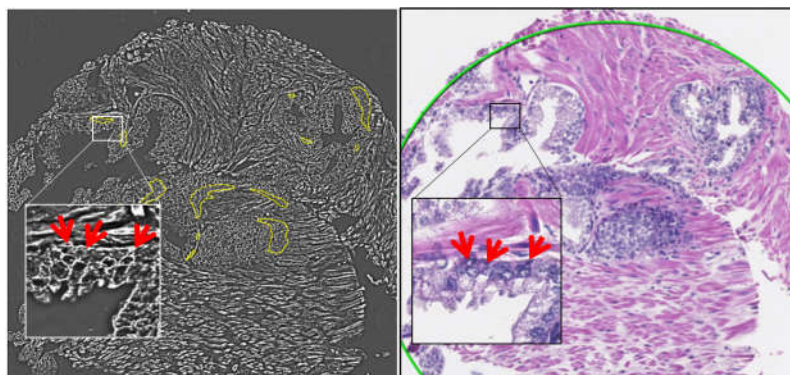


Figure 5.12 GLIM image (left) with basal cells in regions circled in yellow and H&E image (right) of a prostate core. The red arrows point to locations of the basal cells. These cells exist sparsely in the surroundings of the benign glands.

Here, we use the GLMnet [144] classifier to sort each pixel into two classes: basal and non-basal. The GLMnet is particularly suitable for this problem thanks to its ability to train a logistic regression classifier with high dimensional descriptors, i.e. thousands of features. The key benefits of GLMnet come from the use of the Lasso formulation to obtain a small set of coefficients compared to that using classic logistic regression. As a result, GLM is very good at avoiding overfitting the training data which ultimately gives poor validation performance. To obtain high dimensional pixel descriptors, we used the histogram of texton indices with the number of textons set to $K=1024$. This choice of K is expected to capture enough variation in the tissue expression for basal detection. More details on training the GLMnet are given in Appendix C, Section C.4.

Figure 5.13 shows the misclassification error as a function of the coefficient λ , the trade-off factor that controls the sparsity level and the training error. The value on the top row of the plot axis is the number of non-zero coefficients. It can be seen that the misclassification error reduces from 10% to about 14.5% when the number of non-zero coefficients reduces from 700 to approx. 20. The misclassification error saturates at around 14.5% for sufficiently big value of λ .

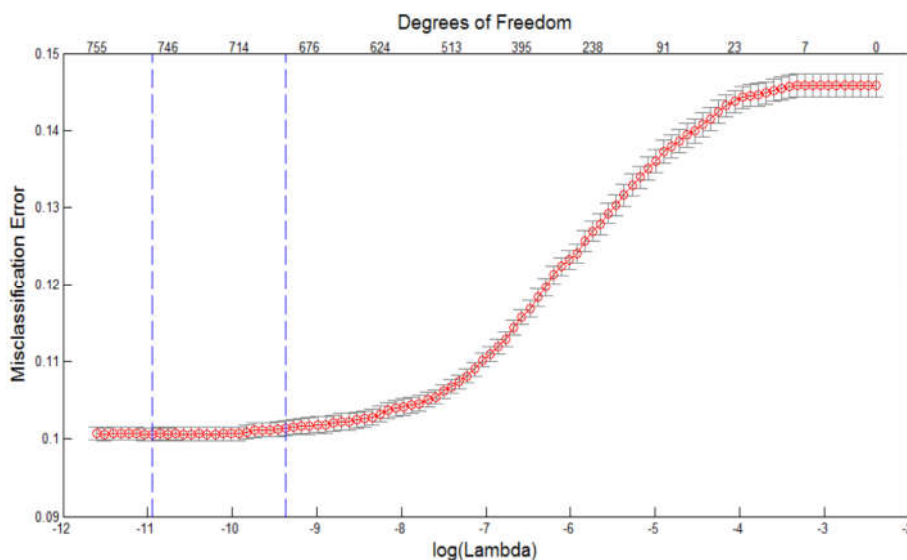


Figure 5.13 Misclassification error evaluated by the GLMnet for different values of λ .

Next, we use the coefficients vector θ^\dagger (corresponding to λ_{1se}) obtained by the GLMnet to classify the whole SLIM image of prostate cores. Figures 5.14(a)-(d) show the basal classification results for four different cores. In each figure, the left image shows the classification results overlaid on the SLIM image. Regions detected as basal are displayed in green. The right figure shows the corresponding H&E image. These H&E images are manually marked by pathologists. Regions marked in green are normal. Their glands are surrounded by a small layer of basal cells. The regions of the H&E image marked in blue are tumor. These regions is not expected to have basal cells. In Fig. 5.14(a), all glands are benign. Therefore, basal cells are expected to be seen in some peripherals of each gland. Its segmentation result (top left) shows that several locations containing basal cells are correctly classified. Figure 5.14(b) has two benign regions and a cancer region. Again, several basal locations surrounding the normal gland are detected correctly. Unfortunately, there are also some false positives in the cancer region (circled as blue in the H&E). They are generated by the inflammatory cells and nucleus of stroma due to close proximity between them and the basal cells. In Fig. 5.14(c), the false positives are generated by the inflammatory cells in stroma and glandular distortion typically obvious at high grade. The tumor region in this core has high Gleason of 4+5 with a lot of distortion. The glands are small, and single epithelial cells are also detected. Figure 5.14(d) shows another example of the false positive. This is a figure of a cancer core where no basal region is expected to exist. However, the classification shows many false positive regions as basal. The false positives are caused by densely packed epithelial cells, generating textures similar to that of the basal cells.

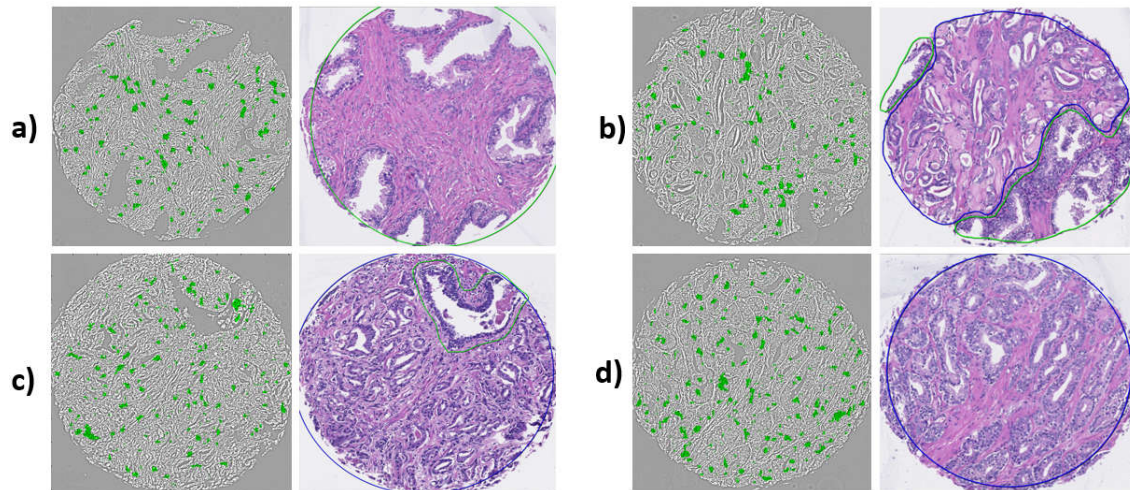


Figure 5.14 (a)-(d) Basal segmentation overlaid on the SLIM images (left) and the corresponding H&E images (right).

The AUC value for basal cell classification as a function of λ is shown in Fig. 5.15. Here, the GLMnet is used in cross-validation mode to optimize the AUC instead of the misclassification error. Clearly, an AUC value of at least 0.9 can be obtained when the number of non-zero coefficients is at least 383 corresponding to $\lambda \geq 10^{-7}$.

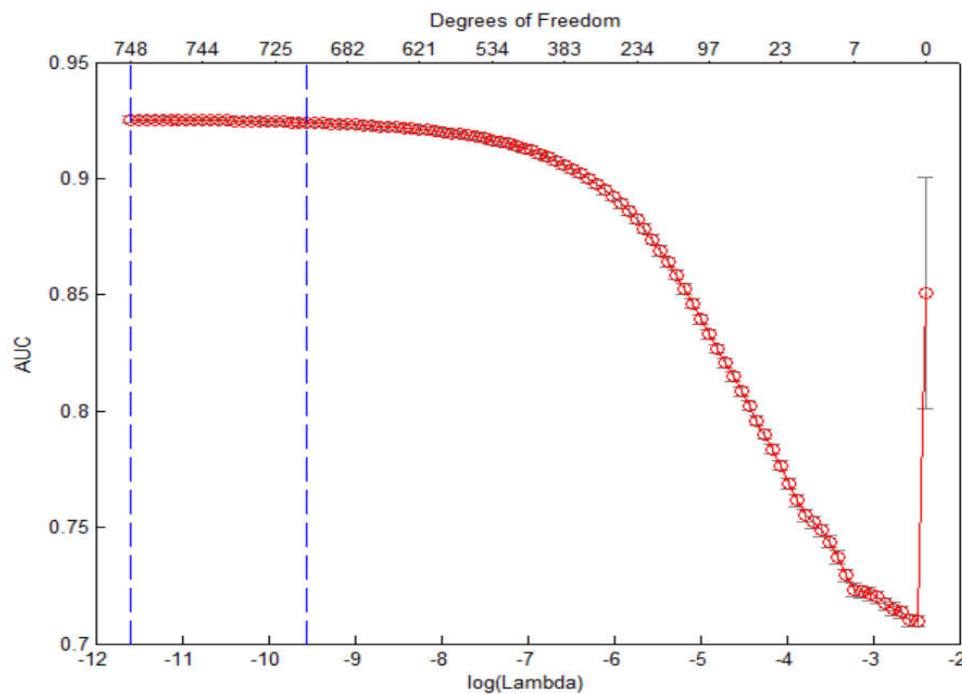


Figure 5.15 AUC values as a function of λ obtained by using the GLMnet in cross-validation mode.

5.6 Summary

In summary, we have introduced a novel approach to obtain automatic diagnosis information using quantitative phase imaging and machine learning. Our method boasts the merits of QPI, which is insensitive to variation in illumination condition, staining procedure, color balance, etc. Therefore, it allows for easy translation across different clinics. The diagnosis is done automatically, using state-of-the art computational tools to produce objective diagnosis results and avoid inter-observer variation. The work uses a dataset of 288 cores from a TMA consisting of 368 cores, with consensus diagnosis results. In the future, we aim to validate our algorithm on a larger dataset to make it more robust to sample variation and to improve the diagnosis accuracy.

CHAPTER 6: GRADIENT LIGHT INTERFERENCE MICROSCOPY (GLIM)

6.1 Introduction

It has become increasingly clear that understanding morphogenesis and disease requires three-dimensional tissue cultures and models [145]. Effective 3D imaging techniques, capable of reporting on subcellular as well as multicellular scales, in a time-resolved manner, are crucial for achieving this goal [146]. While the light microscope has been the main tool of investigation in biomedicine for four centuries, the current requirements for 3D imaging pose new, difficult challenges. Due to their insignificant absorption in the visible spectrum, most living cells exhibit very low contrast when imaged under visible light microscopy. As a result, fluorescence microscopy has become the principal tool of investigation in cell biology [85]. Due to the extraordinary progress in designing fluorescence tags, structures in the cell can be imaged with high specificity. More recently, super-resolution microscopy methods based on fluorescence have opened new directions of investigation, toward the nanoscale subcellular structure [147]. However, fluorescence imaging is subject to several limitations. Absorption of the excitation light may cause the fluorophore to irreversibly alter its molecular structure and stop fluorescing. This process, known as *photobleaching*, limits the time interval over which continuous imaging can be performed [148]. The excitation light is typically toxic to cells, a phenomenon referred to as *phototoxicity* [149]. The development of the green fluorescent protein (GFP) is a technology breakthrough that alleviates some of these limitations [150]. While GFP significantly improves the viability of the specimen under investigation, concerns regarding phototoxicity, photo-bleaching, and functional integrity of the cells upon genetic engineering still remain [151]. Overcoming these limitations becomes extremely challenging

when imaging thick objects over an extended period of time [152, 153]. Acquiring data over the time and the axial dimension increases exposure of the specimen to the excitation light, lowering its viability. Confocal [154] and two-photon fluorescence [155] microscopy have been the main tools for imaging thick 3D specimens. While these methods can provide excellent sectioning through tissue, due to the focused, short wavelength excitation, the amount of power required may be harmful. Thus, recent advances in light sheet microscopy were dedicated specifically to reducing phototoxicity and photobleaching [156-158].

Label-free microscopy provides an alternative solution to overcoming these limitations. Two classical methods are phase contrast (PC) microscopy and differential interference contrast (DIC) microscopy [159]. The contrast in these methods is generated by visualizing the modifications of the wavefront when incident light propagates through the sample. Unfortunately, both PC and DIC are *qualitative*, i.e., they do not measure the wavefront deformation quantitatively. This deformation is characterized by a spatially-dependent phase shift, defined as $\phi(\mathbf{r}) = (2\pi/\lambda_o)h(\mathbf{r})\Delta n(\mathbf{r})$, where λ_o is the central wavelength of the illumination, $h(\mathbf{r})$ and $\Delta n(\mathbf{r})$ are the sample thickness and refractive index difference, both evaluated at the transverse coordinate (\mathbf{r}), respectively. As discussed throughout this thesis, QPI is a novel tool focused precisely on quantifying this optical path length map. It has recently gained significant scientific interest, especially in the biomedical field [8]. Over the past decade, this area of research has seen several advancements in QPI technology to further extend its application boundaries. For example, *common-path* interferometry replaced traditional interferometry for better stability and sensitivity [31, 160, 161]. Low temporal coherence illumination methods surpassed those with laser illumination in image resolution thanks to their ability to suppress the speckle phenomenon [39, 42, 162, 163].

An interesting direction of study is using QPI to extract *scattering* information from extremely weakly scattering objects [164]. This approach is referred to as Fourier transform light scattering (FTLS), to suggest that it is the spatial analog to Fourier transform (infrared) spectroscopy [165]. The idea is that the knowledge of amplitude and phase of an image field allows us to numerically propagate that field and any plane, including the far field, where angular scattering measurements are typically performed. For weakly scattering objects such as live cells, it is much more signal-effective to perform the measurement at the image plane, where all scattering angles overlap at each point, rather than measuring angle by angle in the far field. As a result, QPI can be used to solve inverse scattering problems and extract the 3D structure of inhomogeneous objects [166]. Three-dimensional information of the specimen is accessible by measuring the phase across multiple angles of the illumination or axial specimen positions [167-170]. However, imaging optically thick, multiple scattering specimens is challenging for any optical method, including QPI. The fundamental obstacle is that multiple scattering generates an *incoherent* background, which ultimately degrades the image contrast. An imaging method dedicated to imaging optically thick specimens must include a mechanism to subdue the multiple scattering backgrounds and exhibit strong spatial sectioning to suppress the out of focus light.

To overcome these challenges, here, we introduce a new QPI method, referred to as Gradient Light Interference Microscopy (GLIM). GLIM combines the DIC microscopy with low coherence interferometry and holography. In GLIM, the two interfering fields are identical except for a small transverse spatial shift. This geometry ensures that the two fields suffer equal degradation due to multiple scattering. By accurately controlling the phase shift between the two waves, we acquire multiple intensity images, which have the same incoherent background, but different coherent contributions. As a result, GLIM can reject much of the multiple scattering contribution and yield remarkable contrast of thick objects. Furthermore, the

illumination condenser aperture is fully open, which lends GLIM very strong optical sectioning. GLIM can provide tomographic imaging of both thin samples, e.g., single cells, and thick specimens, such as multicellular systems. Below, we present the principle of GLIM operation, validation results on test samples, and time-resolved tomography of cells in culture, as well as embryo development.

6.2 Optical setup and imaging principle

GLIM is an add-on module to a commercial DIC microscope as shown in Fig. 6.1(a). Via a Wollaston prism, the commercial DIC microscope generates two replicas of the image field, cross-polarized, and shifted transversely by a distance smaller than the diffraction spot. We removed the analyzer polarizer that normally renders the two polarizations parallel in DIC and, instead, let the two fields enter the GLIM module. These fields are spatially Fourier transformed by the lens L_1 at its back focal plane. A spatial light modulator (SLM), placed at this plane with its active axis aligned to the polarization direction of one field, retards its phase by $\phi_n = n\pi/2$ with $n = 0, 1, 2, 3$, and leaves the other field unmodified. Both fields are inversely Fourier-transformed by lens L_2 to generate the image at the camera plane. A linear polarizer, P_1 , is aligned at 45° with respect to both polarizations to render them parallel. The resulting field at the detector is a coherent superposition of two fields, namely,

$$U_n(\mathbf{r}) = U(\mathbf{r}) + U(\mathbf{r} + \delta\mathbf{r})e^{i\phi_n}, \quad (6.1)$$

where $\delta\mathbf{r} = \delta x \hat{\mathbf{x}}$ is the spatial offset between the two fields and U is the image field. The intensity for each phase shift, $I_n(\mathbf{r}) = |U_n(\mathbf{r})|^2$, can be written as

$$I_n(\mathbf{r}) = I(\mathbf{r}) + I(\mathbf{r} + \delta\mathbf{r}) + 2|\gamma(\mathbf{r}, \delta\mathbf{r})| \cos[\phi(\mathbf{r} + \delta\mathbf{r}) - \phi(\mathbf{r}) + \phi_n], \quad (6.2)$$

where $I(\mathbf{r})$ and $\phi(\mathbf{r})$ are, respectively, the intensity and phase of the image field, and γ is the *mutual intensity*, i.e., the temporal cross-correlation function between these two fields,

evaluated at zero delay, $\gamma(\mathbf{r}, \delta\mathbf{r}) = \langle U^*(\mathbf{r})U(\mathbf{r} + \delta\mathbf{r}) \rangle_t$. The phase $\phi_n = n\pi/2$ is the modulated phase offset between the two fields, externally controlled by the SLM. From the four intensity images, $I_n, n=1, \dots, 4$, (Fig. 6.1(b)), we are able to solve for $I(\mathbf{r})$, $|\gamma(\mathbf{r}, \delta\mathbf{r})|$, and $\Delta\phi(\mathbf{r}) = \phi(\mathbf{r} + \delta\mathbf{r}) - \phi(\mathbf{r})$. These data render quantitatively the gradient of the phase along the direction of the shift (Fig. 6.1(c)), $\nabla_x \phi(\mathbf{r}) \approx \Delta\phi(\mathbf{r})/\delta x$. Detailed procedures for extracting the phase gradient and estimating δx can be found in Appendix D, Section D.1. Before image recording, we calibrated the SLM to obtain its phase modulation curve; see Appendix D, Section D.2 for more details on the calibration procedure.

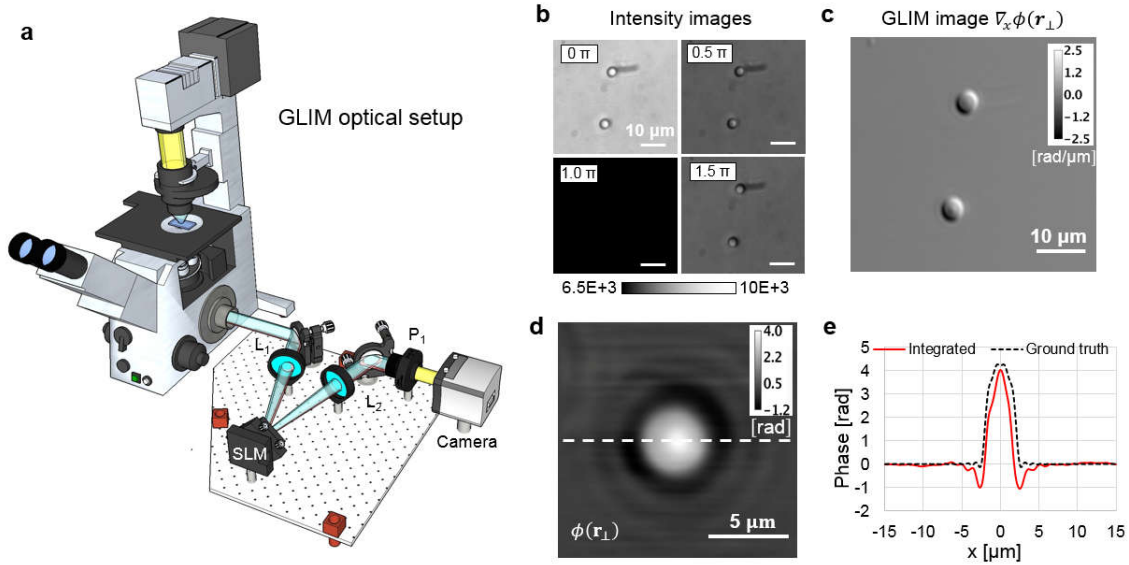


Figure 6.1 Optical setup and working principle of GLIM. (a) GLIM optical setup. (b) The four frames acquired by the GLIM module. (c) Extracted quantitative gradient map of two $3\ \mu\text{m}$ polystyrene beads immersed in oil.

(d) Integrated phase map of a $4.5\ \mu\text{m}$ polystyrene microbeads at $\text{NA}_{\text{con}}=0.09$. (e) Cross-sections of the reconstructed phase and the computed ground truth (black dashed curve) taking into account blurring due to diffraction.

6.3 QPI using GLIM

In order to demonstrate the capability of GLIM to extract quantitatively the phase gradient, we image $4.5 \pm 5\%$ μm polystyrene micro-beads (Polysciences Inc.), with a refractive index of 1.59 at the central wavelength. The beads are immersed in oil (Zeiss Inc.) with a refractive index of 1.518 to generate a total phase shift of 3.87 radians. Figure 6.1(c) shows the measured phase gradient at $\text{NA}_{\text{con}}=0.09$. Given the phase gradient, $\nabla_x\phi$, one can integrate along the gradient direction to get phase value, $\phi(\mathbf{r})$, using

$$\phi(x, y) = \int_0^x [\nabla_x\phi(x', y)] dx' + \phi(0, y), \quad (6.3)$$

where $\phi(0, y)$ is the initial value, which can be obtained with some prior knowledge on the specimen. For example, if $(0, y)$ is a background location, the phase $\phi(0, y)$ should be set to 0 radians. Figure 6.1(d) shows the quantitative phase map, $\phi(\mathbf{r})$, and Fig. 6.1(e) displays a line profile through the center of the bead. Note that our integration result matches very well the expected ground truth.

6.4 Single cell tomography using GLIM

Due to the high numerical aperture of the illumination, GLIM has excellent sectioning capabilities, which yields tomographic imaging of both thin and thick samples. Here, we apply GLIM tomography to a 30% confluence HeLa cell culture over 21 hours. Seven fields of view (FOVs) were imaged using a 63x/1.4 NA objective with a spatial sampling rate of 10.8 pixels/ μm . Each FOV was scanned every 22 minutes. For each time point, the sample is scanned over a total depth of 28 μm with a step size of $\Delta z = 0.07 \mu\text{m}$. Figure 6.2(a) & (b) show the x-y and x-z cross-sections of the GLIM measurement, i.e., the quantitative phase gradient. In order to remove the background due to weak sectioning at small scattering angles, we

perform a spatial filtering operation developed based on a model for 3D image formation in GLIM. More details on this model are presented in Appendix D, Section D.3 and D.4. The filtering operation is explained in detail in Section D.5. Figure 6.2(c) & (d) show the corresponding x-y and x-z cross-sections of the filtering, with yellow arrows pointing to the locations of the nucleus. Clearly, the x-z cross-section of the tomograms shows significant improvements in depth sectioning. Compared to the phase gradient image, $\nabla_x \phi$, this cross-section has no diffraction streaks or “shadow” artifacts and clear cell boundaries. Figure 6.2(e) – (k) show the GLIM tomograms obtained via filtering, at seven different time points. The cell nuclei were segmented and are shown in orange while the cell membranes are displayed in green using iso-surface rendering. The rendered images clearly show different 3D structures of the cells. It can be further seen that during the mitosis phase (the 110 min. and 264 min. frames), the cells assumed a spherical shape during interphase (pointed by yellow arrows in Fig. 6.2(g)). Also, at the 110-minute point, while forming a mitotic sphere, the cells appear to leave behind biomass that is adherent to the substrate, consistent with previous observations [171]. These biomasses are pinpointed by a white arrow in Fig. 6.2(g).

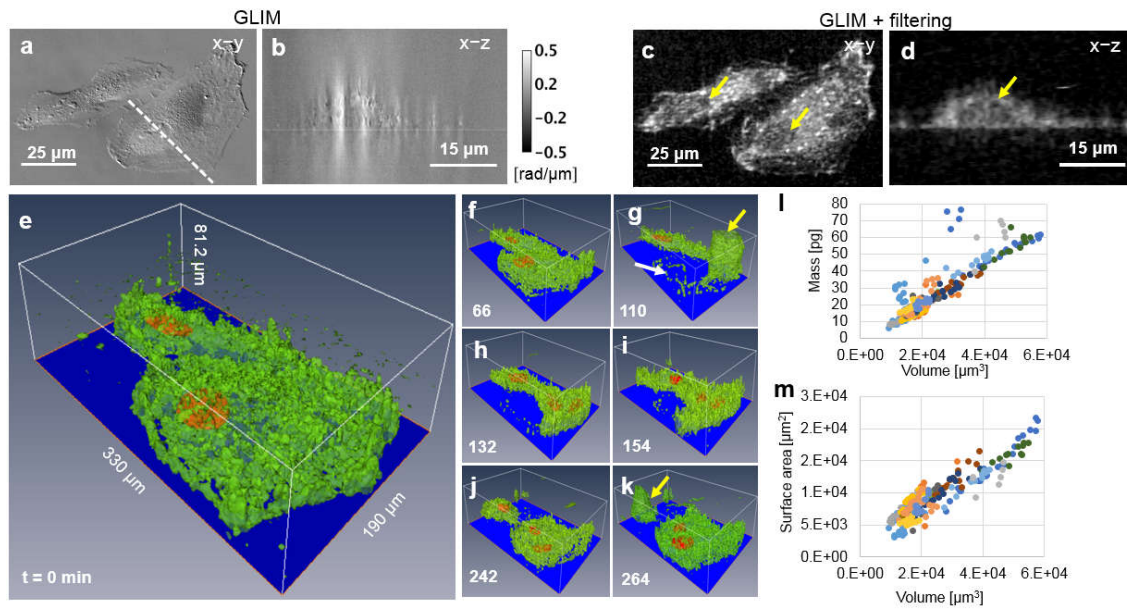


Figure 6.2 GLIM imaging of HeLa cell culture. (a) x-y cross-section and (b) x-z cross-section of the GLIM phase gradient measurement. Dashed line denotes the locations of the cross-section. (c) x-y cross-section and (d) x-z cross-section after spatial filtering. (e) – (k) Rendering of the cell tomography results at different time points, as indicated. (l) Mass vs. volume and (m) area vs. volume measurements extracted from the GLIM tomography data.

Thanks to the excellent depth sectioning of the GLIM, we can compute several parameters for each cell and study their time evolution. Figure 6.2(l) shows the dry mass vs. volume for several different cells during the 21-hour window. To obtain the cellular metrics for an individual cell, we first segment them automatically using a procedure mentioned in the Appendix, Section D.6. The dry mass is computed from the reconstructed susceptibility following a method mentioned in Section D.7, Appendix D. Each point in these plots corresponds to one cell at one time-point. These results show that, for the most part, the points align along a straight line. We found that the points deviating from this line correspond to cells going through mitosis. This result indicates that there is a significant density increase during mitosis. Meanwhile, the surface area vs. volume relation shown in Fig. 6.2(m) is essentially linear with

slightly different slopes for different cells over the whole cell cycle. More results on the time-lapse measurement are given in Appendix D, Section D.8.

6.5 GLIM for embryo tomography

The Centers for Disease Control and Prevention (CDC) report from 2014 shows that 208,768 ART cycles were performed with 57,332 live births [172]. As the numbers indicate, the percentage of live births from these procedures is still rather low. One reason is the lack of objective and accurate evaluation of the embryo quality and viability before transfer. Morphological assessment is currently the main method used to determine embryo viability during IVF cycles. However, studies have shown that the predictive power of the typical day 2 and 3 assessment of morphological parameters has remained low [173-175]. Various noninvasive analytical tools have recently been used for noninvasive prediction of embryonic potential [176-180]. One such tool has been the development of quantitative techniques for the non-invasive assessment of embryo metabolism, and its value as a predictor of embryo viability is the subject of ongoing investigations [181]. But currently, the visual observation remains the most used and reliable method. With the improvement of microscopy, it is possible to follow embryo development in real time, and it has been established that morphokinetic parameters can be used to select embryos with higher potential [182]. One of the most important microscopy techniques is transmission electronic microscopy (TEM), which is considered by many the main tool for intracellular evaluation. The main problem with using TEM for embryo evaluation is that the preparation of the sample requires non-vital fixation of the sample that kills the embryo [183]. Therefore, while this type of microscopy can be considered an important tool for research, it has little value for routine IVF procedures. The other technique commonly used to evaluate the embryo quality is confocal microscopy. In this case, the sample must be stained in order to be evaluated, which can be detrimental to embryo survival. Due to

its excellent sectioning capabilities, GLIM can be used to perform tomography on optically thick specimens such as embryos.

Here, we obtained three-dimensional GLIM stacks of bovine embryos at different development stages. We used a 63x / 1.4 NA oil immersive objective at a transverse sampling rate of 10 pixel/ μm . The condenser aperture was fully opened to $\text{NA}_{\text{con}}=0.55$ to maximize the depth sectioning and spatial resolution. The embryos were scanned in the axial dimension over an interval of $[-120 \mu\text{m}, 120 \mu\text{m}]$ with a step of $\Delta z = 0.05 \mu\text{m}$. Figure 6.3(a) & (b) show the x-y and x-z cross-sections of the raw phase gradient. The corresponding cross-sections of the GLIM tomogram are shown in Fig. 6.3(c) & (d). The GLIM tomography reveals various structures of the embryos, including their membranes, internal cells, gaps between the membrane of the cells and their internal content, lipid droplets in each cell, as indicated in Fig. 6.3(e). The x-z cross-sections further show the contact between the embryo and the underlying glass substrate (Fig. 6.3(d)), and the debris on the substrate.

Figures 6.3(f) – (h) show the rendering results of three different embryos, consisting of two cells, four cells, and five cells, as indicated. One can see clearly how different cells of the embryos stack with respect to each other in 3D. The membranes of the embryos are manually segmented and displayed as transparent surfaces.

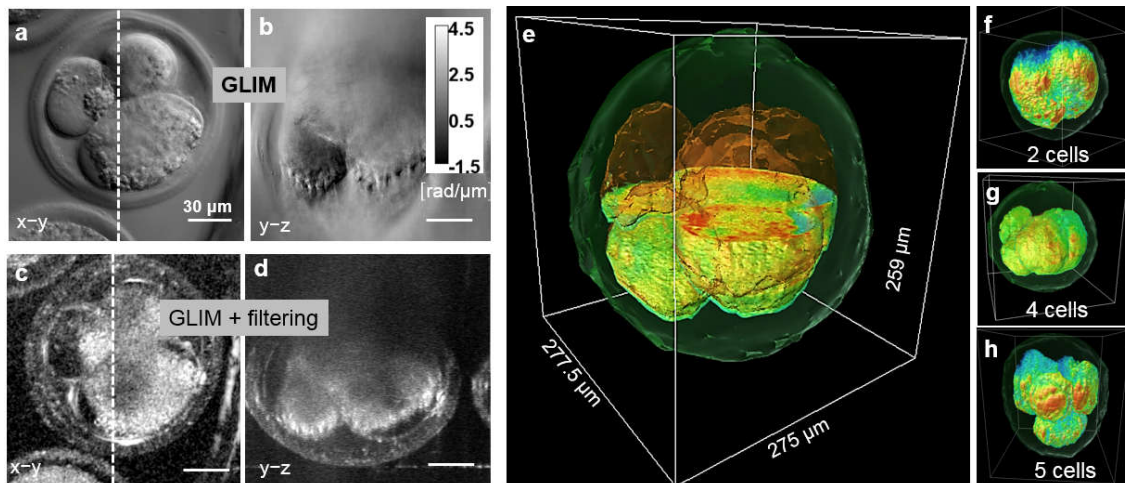


Figure 6.3 GLIM imaging for thick embryos. (a) x-y cross-section and (b), y-z cross-section of raw GLIM images in a bovine embryo. (c) x-y and (d) y-z cross-sections after spatial filtering. (e) A rendered embryo that was cut through the center to reveal internal structures. (f) – (h) Bovine embryos at different points in their development stages, as indicated.

6.6 Summary

In summary, we introduced GLIM, as a new QPI method, for 3D imaging of unlabeled specimens. GLIM has all the benefits of common-path white-light methods including nanometer path length stability, and speckle-free and diffraction-limited resolution. At the smallest condenser aperture, GLIM gives exact values of the quantitative phase for thin samples. At the largest condenser aperture, GLIM can be used as a tomography method, allowing us to obtain three-dimensional information of thick imaging samples. We demonstrated the success of GLIM on various samples, e.g., beads, HeLa cells, and bovine embryos. We believe that this method will set an excellent foundation for other research projects and high-impact applications.

As a label-free method, GLIM can be applied to imaging live cells and thick samples nondestructively over broad temporal and spatial scales. This technique is not limited by photobleaching and phototoxicity commonly associated with fluorescence microscopy. Also, it provides excellent optical sectioning and obtains three-dimensional information from

unlabeled specimens. However, similar to other label-free images, GLIM lacks specificity. Therefore, we envision that GLIM and fluorescence techniques will co-exist and corroborate the advantages of specificity and noninvasiveness. This is completely feasible since GLIM operates on the same optical path as the fluorescence channels, allowing a seamless combination of the two modalities.

CHAPTER 7: CONCLUSION

In this dissertation, we have demonstrated the use of computational tools to improve several aspects of QPI and push its application boundary further. In Chapter 2, we built a new QPI imaging system, tSLIM, that replaced the PANLC-SLM in the traditional SLIM system with a more popular, cost-effective TNLC-SLM. However, this change comes with extra complication in the image formation and phase retrieval. Thanks to the help of computational tools, especially linear algebra, these obstacles were overcome. Chapters 3 & 4 solved common issues in common-path QPI, in particular, e.g. halo artifacts and phase underestimation. By modeling the image formation using Fourier optics, we discovered that the cause of these problems was the spatial coherence of the illumination. To have halo-free QPI images and avoid phase underestimation, the illumination needs to be perfectly coherent or, at least coherent enough that its coherence area is larger than the FOV. Unfortunately, these requirements are very hard to satisfy in practice with white-light illumination. In microscopy, the use of white-light is highly expected thanks to its ability to give speckle-free images at diffraction-limit resolution. It is known that optical solution, e.g., laser illumination, can solve the problem. However, it requires pristine optics and causes the speckle phenomenon, which ultimately degrades the image quality. This dissertation introduces the computational solution to the spatial coherence problem. Using this solution, we were able to remove the halo phenomenon and obtain the correct quantitative phase value under white-light illumination. Chapter 5 combined QPI with machine learning to build the first tissue scanner for automatic diagnosis of prostate cancer. We first build a random forest classifier to classify each pixel into one of three categories: gland, lumen, and stroma. Then, from pixel label maps, we computed morphological and quantitative features and passed them to subsequent classifiers to produce diagnosis results. Two automatic diagnosis problems were studied, including automatic

Gleason grading and cancer vs. non-cancer classification. Finally, while other chapters deploy partially coherent illumination to obtain the phase information, Chapter 6 introduces an entirely new QPI method, named GLIM, which uses almost incoherent illumination. GLIM has all the benefits of common-path white-light methods including speckle-free and diffraction-limited resolution. Also, it has no halo artifact compared to SLIM or DPM. The phase underestimation from GLIM comes from the objective lens instead of the condenser lens. This fact allows us to maximize the condenser aperture in GLIM to greatly increase the depth sectioning. Again, computational modeling helped us understand the limits of GLIM. We proposed a filtering method to reduce the diffraction streaks and significantly enhance its axial sectioning. We demonstrated the use of GLIM to image optically thick samples, e.g., bovine embryo, that are hundreds of microns thick. We believe that this method will set an excellent foundation for other research projects and high-impact applications.

APPENDIX A: SUPPLEMENTAL INFORMATION FOR CHAPTER 3

A.1 Extracting the cross-correlation function from interference fringes

We used the following procedure to obtain the temporal cross-correlation function in the DPM experiment. The only difference between the 2D and 3D case is that the procedure is repeated at different z values in the latter case. The DPM intensity image captured by the camera can be written as

$$\begin{aligned} I(\mathbf{r}) &= \left\langle \left| \mathbf{U}_r(\mathbf{r}, t) + \mathbf{U}_t(\mathbf{r}, t) e^{ik_{xo}x} \right|^2 \right\rangle_t \\ &= I_r(\mathbf{r}) + I_t(\mathbf{r}) + \Gamma_{p,r}(\mathbf{r}, \mathbf{r}, 0) e^{-ik_{xo}x} + \Gamma_{p,r}^*(\mathbf{r}, \mathbf{r}, 0) e^{ik_{xo}x}, \end{aligned} \quad (\text{A.1})$$

where k_{xo} is the spatial wave vector generated by the DPM grating. Note that the first two terms in the expansion of $I(\mathbf{r})$ exist at base-band while the third term and fourth term are centered around $\mathbf{k}_\perp = [\pm k_{xo}, 0]$ in the spatial frequency domain. Therefore, $\Gamma_{p,r}(\mathbf{r}, \mathbf{r}, 0)$ can be obtained by applying a band-pass filter on $I(\mathbf{r})$ so that its bandwidth matches to that of the fourth component, followed by shifting the remaining spectrum into the baseband, which is the principle of off-axis holography suggested by D. Gabor [184].

A.2 Convergence of the 3D ideal phase to 2D ideal phase

The “ideal” phase in 3D is given by Eq. (3.8) as $\varphi(\mathbf{r}) = [\beta_o / (2\bar{n})] \left[X \oplus_r \mathfrak{F}_{\mathbf{k}_\perp}^{-1} \left(e^{i(q-\bar{n}\beta_o)z} \right) \right](\mathbf{r})$.

Let us consider a thin object, of thickness h , placed around the $z = 0$ plane, characterized by a susceptibility function $\chi(\mathbf{r}) = \Pi(z/h) \left[n(\mathbf{r}_\perp)^2 - \bar{n}^2 \right] \approx 2\bar{n}\Pi(z/h) \left[n(\mathbf{r}_\perp) - \bar{n} \right]$, where $\Pi(\cdot)$

is the rectangular function. We have also approximated $n(\mathbf{r}_\perp) + \bar{n} \approx 2\bar{n}$. For a well-focused sample, ignoring the defocusing diffraction, i.e., $\mathfrak{F}_{\mathbf{k}_\perp}^{-1}\left(e^{i(q-\bar{n}\beta)z}\right) \rightarrow \delta^{(2)}(\mathbf{r}_\perp)1(z)$, we have $\varphi(\mathbf{r}) \rightarrow h\bar{\beta}\left[n(\mathbf{r}_\perp) - \bar{n}\right]$, which is the definition of phase for the two-dimension case.

A.3 Derivation for the formula of the 3D measured phase

Recall that in DPM, the field U_r is generated by 2D spatially filtering the sample field U_p , i.e.

$$\mathbf{U}_r(z) = \int \mathbf{U}_i(\mathbf{r}_\perp, z) d^2\mathbf{r}_\perp \equiv \mathbf{U}_{io}(z),$$

where z is the axial coordinate. Here, we use the “o” subscript to denote the spatial filtering operation to generate the reference. In the Born approximation, the sample field is assumed to consist of an incident field, U_i , and a scattered field, U_s . Therefore, the reference field also consists of a “filtered” incident, U_{io} , and a “filtered” scattered field, U_{so} . Using the decomposition $U_p = U_i + U_s$, and $U_{io} = U_{io} + U_{so}$, we rewrite the cross-correlation function as

$$\begin{aligned} \Gamma_{pr}(\mathbf{r}, \mathbf{r}, 0) &= \langle \mathbf{U}_i + \mathbf{U}_s, \mathbf{U}_{io}^* + \mathbf{U}_{so}^* \rangle_i(\mathbf{r}, \mathbf{r}) \\ &= \Gamma_{i,io}(\mathbf{r}, \mathbf{r}, 0) + \Gamma_{s,io}(\mathbf{r}, \mathbf{r}, 0) + \Gamma_{i,so}(\mathbf{r}, \mathbf{r}, 0) + \Gamma_{s,so}(\mathbf{r}, \mathbf{r}, 0), \end{aligned} \quad (\text{A.2})$$

where $\Gamma_{i,io}, \Gamma_{s,io}, \Gamma_{i,so}, \Gamma_{s,so}$ are cross-correlation functions, evaluated at zero-delay $\tau=0$, between the incident field and its low-pass version, the scatter field and the incident low-pass version, the incident field & the scattering low-pass version, and the scatter field and its low-pass version, respectively. Ignoring $\Gamma_{s,so}(\mathbf{r}, \mathbf{r})$ because it is much smaller in amplitude than other terms, the following results hold (see Appendix A, Sections A.4, A.5, A.6 for more details).

$$\Gamma_{i,io}(\mathbf{r}, \mathbf{r}) = \tilde{\Gamma}_i(\mathbf{0}), \quad (\text{A.3})$$

$$\Gamma_{s,io}(\mathbf{r}, \mathbf{r}) = i\tilde{\Gamma}_i(\mathbf{0})\varphi(\mathbf{r}), \quad (\text{A.4})$$

$$\Gamma_{i,so}(\mathbf{r}, \mathbf{r}; 0) = -i\tilde{\Gamma}_i(\mathbf{0})[\varphi(\mathbf{r}) \odot_{\mathbf{r}} h_i(\mathbf{r})]. \quad (\text{A.5})$$

Here, $\tilde{\Gamma}_i(\cdot)$ is the spatial Fourier transform of the mutual intensity function $\Gamma_i(\mathbf{r}_{\perp})$. Note that, among these terms, the first one, $\Gamma_{i,io}$, only relates to the illumination. The second and third are imaginary. The fact that they have opposite signs tells that they cancel each other out, causing the halo and phase-underestimation artifact. Using these terms, Eq. (3.7) can be proven easily using

$$\begin{aligned} \arg[J_{t,r}(\mathbf{r}, \mathbf{r}, 0)] &= \arctan[\text{Im}(J_{t,r})/\text{Re}(J_{t,r})] \\ &= \arctan\left\{\frac{[J_{s,io}(\mathbf{r}, \mathbf{r}) + J_{i,so}(\mathbf{r}, \mathbf{r}; 0)]/J_{i,io}(\mathbf{r}, \mathbf{r})}{J_{i,io}(\mathbf{r}, \mathbf{r})}\right\} \\ &\approx [J_{s,io}(\mathbf{r}, \mathbf{r}) + J_{i,so}(\mathbf{r}, \mathbf{r}; 0)]/J_{i,io}(\mathbf{r}, \mathbf{r}) \\ &= \varphi(\mathbf{r}) \odot_{\mathbf{r}} [\delta^{(3)}(\mathbf{r}) - h_i(\mathbf{r})]. \end{aligned} \quad (\text{A.6})$$

A.4 Derivation for the expression of $\Gamma_{i,io}$

We have $\Gamma_{i,io}(\mathbf{r}, \mathbf{r}; 0) = \left\langle U_i(\mathbf{r}_{\perp}, z, t) \int U_i^*(\mathbf{r}'_{\perp}, z, t) d^2\mathbf{r}'_{\perp} \right\rangle_t = \int \Gamma_i(\mathbf{r}_{\perp}, z, \mathbf{r}'_{\perp}, z) d^2\mathbf{r}'_{\perp}$.

Combining this equation with Eq. (14) of [185],

$\Gamma_i(\mathbf{r}_{\perp}, z, \mathbf{r}'_{\perp}, z) = \int \tilde{\Gamma}_i(\mathbf{k}_{\perp}) \exp[i\mathbf{k}_{\perp} \cdot (\mathbf{r}_{\perp} - \mathbf{r}'_{\perp})] d^2\mathbf{k}_{\perp}$, we have

$$\Gamma_{i,io}(\mathbf{r}, \mathbf{r}; 0) = \iint \tilde{\Gamma}_i(\mathbf{k}_{\perp}) \exp[i\mathbf{k}_{\perp} \cdot (\mathbf{r}_{\perp} - \mathbf{r}'_{\perp})] d^2\mathbf{k}_{\perp} d^2\mathbf{r}'_{\perp} = \tilde{\Gamma}_i(\mathbf{0}_{\perp}) \int \delta^{(2)}(\mathbf{k}_{\perp}) d^2\mathbf{k}_{\perp} = \tilde{\Gamma}_i(\mathbf{0}_{\perp}).$$

A.5 Derivation for the expression of $\Gamma_{s,io}$

The scattered field U_s is given using the 1st-order Born approximation as [186]

$U_s(\mathbf{r}; t) \approx \beta_o^2 \int \chi(\mathbf{r}') U_i(\mathbf{r}', t) g(\mathbf{r} - \mathbf{r}') d^3\mathbf{r}'$, where $g(\cdot)$ is the Green's function of the system.

For simplicity, we have ignored dispersion of the sample, i.e., $\chi(\mathbf{r}) = n(\mathbf{r})^2 - \bar{n}^2$, independent of wavelength. Then,

$$\begin{aligned}
\Gamma_{s,io}(\mathbf{r},\mathbf{r}) &= \left\langle U_s(\mathbf{r}_\perp,z,t) \int U_i^*(\mathbf{r}''_\perp,z,t) d^2\mathbf{r}''_\perp \right\rangle_t \\
&= \beta_o^2 \left\langle \int \chi(\mathbf{r}') U_i(\mathbf{r}'_\perp,z',t) g(\mathbf{r}-\mathbf{r}') d^3\mathbf{r}' \int U_i^*(\mathbf{r}''_\perp,z,t) d^2\mathbf{r}''_\perp \right\rangle_t \quad (\text{A.7}) \\
&= \beta_o^2 \iint \chi(\mathbf{r}') \Gamma_i(\mathbf{r}'_\perp,z',\mathbf{r}''_\perp,z) g(\mathbf{r}-\mathbf{r}') d^3\mathbf{r}' d^2\mathbf{r}''_\perp.
\end{aligned}$$

Again, Eq. (14) of [185] gives

$$\Gamma_i(\mathbf{r}'_\perp,z',\mathbf{r}''_\perp,z) = \int \tilde{\Gamma}_i(\mathbf{k}_\perp) \exp[i\mathbf{k}_\perp \cdot (\mathbf{r}'_\perp - \mathbf{r}''_\perp) + iq(\mathbf{k}_\perp)(z' - z)] d^2\mathbf{k}_\perp, \text{ which transforms Eq.}$$

(A.7) into

$$\begin{aligned}
\Gamma_{s,io}(\mathbf{r},\mathbf{r}) &= \beta_o^2 \iint \chi(\mathbf{r}') \int \tilde{\Gamma}_i(\mathbf{k}_\perp) \exp[i\mathbf{k}_\perp \cdot (\mathbf{r}'_\perp - \mathbf{r}''_\perp) + iq(\mathbf{k}_\perp)(z' - z)] d^2\mathbf{k}_\perp g(\mathbf{r}-\mathbf{r}') d^3\mathbf{r}' d^2\mathbf{r}''_\perp \\
&= \tilde{\Gamma}_i(\mathbf{0}_\perp) \beta_o^2 \int \chi(\mathbf{r}') g(\mathbf{r}-\mathbf{r}') \exp[-i\bar{n}\bar{\beta}(z-z')] d^3\mathbf{r}' = \tilde{\Gamma}_i(\mathbf{0}_\perp) \beta_o^2 \left\{ \chi \odot_r \left[g \exp(-i\bar{n}\bar{\beta}z) \right] \right\}(\mathbf{r}). \quad (\text{A.8})
\end{aligned}$$

Under paraxial approximation, $g(\mathbf{r}) \approx i\mathfrak{S}_{\mathbf{k}_\perp}^{-1}(e^{iqz})/2\bar{n}\beta_o$, Eq. (A.8) becomes

$$\Gamma_{s,io}(\mathbf{r},\mathbf{r}) = i\tilde{\Gamma}_i(\mathbf{0}_\perp) \left\{ \chi \odot_r \left[\left[\bar{\beta}/(2\bar{n}) \right] \mathfrak{S}_{\mathbf{k}_\perp}^{-1} \left[e^{i(q-\bar{n}\bar{\beta})z} \right] \right] \right\}(\mathbf{r}) = i\tilde{\Gamma}_i(\mathbf{0}_\perp) \varphi(\mathbf{r}), \text{ which completes}$$

the proof.

A.6 Derivation for the expression of $\Gamma_{i,so}$

By definition,

$$\begin{aligned}
\Gamma_{i,so}(\mathbf{r},\mathbf{r}) &= \left\langle U_i(\mathbf{r}_\perp,z,t) \int U_s^*(\mathbf{r}'_\perp,z,t) d^2\mathbf{r}'_\perp \right\rangle_t \\
&= \iint \beta_o^2 \chi^*(\mathbf{r}'') \left\langle U_i(\mathbf{r}_\perp,z,t) U_i^*(\mathbf{r}''_\perp,z'',t) \right\rangle g^*(\mathbf{r}' - \mathbf{r}'') d^3\mathbf{r}'' d^2\mathbf{r}'_\perp \quad (\text{A.9}) \\
&= \iint \bar{\beta}^2 \chi^*(\mathbf{r}'') \Gamma_i(\mathbf{r}_\perp,z,\mathbf{r}''_\perp,z'') g^*(\mathbf{r}'_\perp - \mathbf{r}''_\perp, z - z'') d^3\mathbf{r}'' d^2\mathbf{r}'_\perp.
\end{aligned}$$

Using Eq. (14) of [185], dropping the conjugate notation on χ , and changing the order of integration in Eq. (A.9), we have

$$\begin{aligned}
\Gamma_{i,so}(\mathbf{r},\mathbf{r}) &= \left\langle U_i(\mathbf{r}_\perp, z, t) \int U_s^*(\mathbf{r}'_\perp, z, t) d^2\mathbf{r}'_\perp \right\rangle_i \\
&= \iint \beta_o^2 \chi^*(\mathbf{r}'') \left\langle U_i(\mathbf{r}_\perp, z, t) u_i^*(\mathbf{r}''_\perp, z'', t) \right\rangle g^*(\mathbf{r}' - \mathbf{r}'') d^3\mathbf{r}'' d^2\mathbf{r}'_\perp \quad (\text{A.10}) \\
&= \iint \beta_o^2 \chi^*(\mathbf{r}'') \Gamma_i(\mathbf{r}_\perp, z, \mathbf{r}''_\perp, z'') g^*(\mathbf{r}'_\perp - \mathbf{r}''_\perp, z - z'') d^3\mathbf{r}'' d^2\mathbf{r}'_\perp.
\end{aligned}$$

Under the paraxial approximation: $\int g^*(\mathbf{r}'_\perp - \mathbf{r}''_\perp, z - z'') d^2\mathbf{r}'_\perp \approx -i \mathfrak{S}_{\mathbf{k}_\perp}^{-1} \left[e^{-i\bar{m}\bar{\beta}(z-z'')} \right] / 2\bar{n}\bar{\beta}$, Eq. (A.10)

becomes

$$\begin{aligned}
\Gamma_{i,so}(\mathbf{r},\mathbf{r}) &= -i \int \beta_o / (2\bar{n}) \chi(\mathbf{r}'') \left\{ \int \tilde{\Gamma}_i(\mathbf{k}_\perp) \exp \left[\begin{array}{l} i\mathbf{k}_\perp \cdot (\mathbf{r}_\perp - \mathbf{r}''_\perp) + \\ i[q(\mathbf{k}_\perp) - \bar{n}\bar{\beta}](z - z'') \end{array} \right] d^2\mathbf{k}_\perp \right\} d^3\mathbf{r}'' \\
&= -i \int \beta_o / (2\bar{n}) \chi(\mathbf{r}'') \left[\mathfrak{S}_{\mathbf{k}_\perp}^{-1} \left(e^{i(q - \bar{n}\bar{\beta})(z - z'')} \right) \odot_{\mathbf{r}_\perp} \Gamma_i \right] (\mathbf{r} - \mathbf{r}'') d^3\mathbf{r}'' \\
&= -i [\beta_o / (2\bar{n})] \left\{ \chi \odot_{\mathbf{r}} \mathfrak{S}_{\mathbf{k}_\perp}^{-1} \left(e^{i(q - \bar{n}\bar{\beta})z} \right) \odot_{\mathbf{r}} [\Gamma_i(\mathbf{r}_\perp) \delta(z)] \right\} \quad (\text{A.11}) \\
&= -i \tilde{\mathcal{S}}(\mathbf{0}_\perp) \left\{ X \odot_{\mathbf{r}} \left\{ [\bar{\beta} / (2\bar{n})] \mathfrak{S}_{\mathbf{k}_\perp}^{-1} \left(e^{i(q - \bar{n}\bar{\beta})z} \right) \right\} \odot_{\mathbf{r}} \left\{ [\Gamma_i(\mathbf{r}_\perp) / \tilde{\Gamma}_i(\mathbf{0}_\perp)] \delta(z) \right\} \right\} (\mathbf{r}) \\
&= -i \tilde{\mathcal{S}}(\mathbf{0}_\perp) \left\{ X \odot_{\mathbf{r}} \left\{ [\bar{\beta} / (2\bar{n})] \mathfrak{S}_{\mathbf{k}_\perp}^{-1} \left(e^{i(q - \bar{n}\bar{\beta})z} \right) \right\} \odot_{\mathbf{r}} h_i \right\} (\mathbf{r}) = -i \tilde{\Gamma}_i(\mathbf{0}_\perp) \left\{ \varphi \odot_{\mathbf{r}} h_i \right\} (\mathbf{r}),
\end{aligned}$$

which completes the proof.

APPENDIX B: SUPPLEMENTAL INFORMATION FOR CHAPTER 4

B.1 Characterizing the functions Γ_i , h_o , and h_s

For a successful inversion to obtain halo-free images, the functions Γ_i , h_o , and h_s need to be estimated with high accuracy. These functions are characterized by the illumination wavelength, NA_{obj} , and the illumination aperture, governed by $NA_{ring,min}$, and $NA_{ring,max}$. While NA_{obj} is provided by the microscope manufacturer, other parameters are not always available. To determine them, we imaged the back aperture of the objective onto the camera plane. Thus, the inner radius, $r_{ring,in}$, outer radius, $r_{ring,out}$, of the phase ring and that of the objective's aperture, r_{obj} , were measured experimentally. With these dimensions available, we calculate $NA_{ring,min}$ and $NA_{ring,max}$ using relations $NA_{ring,min} = r_{obj} NA_{obj} / r_{ring,in}$, $NA_{ring,out} = r_{obj} NA_{obj} / r_{ring,out}$. When a PC objective is used, its attenuation factor has to be incorporated into the model by manipulating h_o . To determine this attenuation, we calculate the ratio between the average intensity over a line profile inside and outside the objective phase ring. Finally, the mutual intensity of the illumination field at the image plane is obtained by two-dimensional Fourier transforming the intensity of the condenser aperture, i.e., $\Gamma_i(\mathbf{r}_\perp) = \tilde{I}_c[2\pi\mathbf{r}_\perp/(\lambda f_c)]$. Here, \tilde{I}_c is the spatial Fourier transform of the condenser aperture intensity, f_c is the focal length of the condenser aperture, and λ is the mean wavelength of the illumination.

B.2 Extracting four terms of Eq. (4.1)

Equation (4.1) in the main text reads

$$I(\mathbf{r}; n\pi/2) = I_1 + I_2 + i^n C_3 + (-i)^n C_4, \quad (\text{B.1})$$

where four individual terms I_1, I_2, I_3, I_4 are defined by

$$\begin{aligned} I_1 &= \iint d^2\mathbf{r}_1 d^2\mathbf{r}_2 \Gamma_i(\mathbf{r}_1 - \mathbf{r}_2) t(\mathbf{r}_1) \mathcal{F}^*(\mathbf{r}_2) h_o(\mathbf{r} - \mathbf{r}_1) h_o^*(\mathbf{r} - \mathbf{r}_2), \\ I_2 &= \iint d^2\mathbf{r}_1 d^2\mathbf{r}_2 \Gamma_i(\mathbf{r}_1 - \mathbf{r}_2) t(\mathbf{r}_1) \mathcal{F}^*(\mathbf{r}_2) h_s(\mathbf{r} - \mathbf{r}_1) h_s^*(\mathbf{r} - \mathbf{r}_2), \\ C_3 &= \iint d^2\mathbf{r}_1 d^2\mathbf{r}_2 \Gamma_i(\mathbf{r}_1 - \mathbf{r}_2) t(\mathbf{r}_1) \mathcal{F}^*(\mathbf{r}_2) h_o(\mathbf{r} - \mathbf{r}_1) h_s^*(\mathbf{r} - \mathbf{r}_2), \\ C_4 &= \iint d^2\mathbf{r}_1 d^2\mathbf{r}_2 \Gamma_i(\mathbf{r}_1 - \mathbf{r}_2) t(\mathbf{r}_1) \mathcal{F}^*(\mathbf{r}_2) h_s(\mathbf{r} - \mathbf{r}_1) h_o^*(\mathbf{r} - \mathbf{r}_2). \end{aligned} \quad (\text{B.2})$$

The sub-equations in (B.2) are generally valid under partially coherent illumination, governed by the mutual intensity Γ_i . To prove them, let us start by considering that the point sources at the condenser plane are independent of each other. Each point source in the condenser aperture, which is characterized by a transverse spatial frequency of \mathbf{k} , generates a plane wave $e^{i\mathbf{k}\mathbf{r}}$ onto the sample plane, yielding a new total field of $(e^{i\mathbf{k}\mathbf{r}T})$ right after it. The unmodulated region of the back aperture, i.e. the non-ring one, with the PSF of h_s , generates a coherent response of $(e^{i\mathbf{k}\mathbf{r}T}) \circledast_{\mathbf{r}} h_s$. The modulating region with the phase modulation of $n\pi/2$ alters the PSF to $i^n h_o$ and gives a coherent response at the camera plane of $(e^{i\mathbf{k}\mathbf{r}T}) \circledast_{\mathbf{r}} (i^n h_o)$. Combining the responses with a contribution of an intensity term of $I_c(\mathbf{k})$ for different wave vectors \mathbf{k} , we have the total intensity image of [89]

$$I(\mathbf{r}; n\pi/2) = \int d^2\mathbf{k} I_c(\mathbf{k}) \left[(e^{i\mathbf{k}\mathbf{r}T}) \circledast_{\mathbf{r}} (h_s + i^n h_o) \right]^2(\mathbf{r}). \quad (\text{B.3})$$

Expanding the convolution operation, $\circledast_{\mathbf{r}}$, we further obtain

$$\begin{aligned}
I(\mathbf{r}; n\pi/2) = & \iint d^2\mathbf{r}_1 d^2\mathbf{r}_2 \left[d^2\mathbf{k} I_c(\mathbf{k}) e^{i\mathbf{k}\cdot(\mathbf{r}_1-\mathbf{r}_2)} \right] T(\mathbf{r}_1) T^*(\mathbf{r}_2) h_o(\mathbf{r}-\mathbf{r}_1) h_o^*(\mathbf{r}-\mathbf{r}_2) \\
& + \iint d^2\mathbf{r}_1 d^2\mathbf{r}_2 \left[d^2\mathbf{k} I_c(\mathbf{k}) e^{i\mathbf{k}\cdot(\mathbf{r}_1-\mathbf{r}_2)} \right] T(\mathbf{r}_1) T^*(\mathbf{r}_2) h_s(\mathbf{r}-\mathbf{r}_1) h_s^*(\mathbf{r}-\mathbf{r}_2) \\
& + (-i)^n \iint d^2\mathbf{r}_1 d^2\mathbf{r}_2 \left[d^2\mathbf{k} I_c(\mathbf{k}) e^{i\mathbf{k}\cdot(\mathbf{r}_1-\mathbf{r}_2)} \right] T(\mathbf{r}_1) T^*(\mathbf{r}_2) h_s(\mathbf{r}-\mathbf{r}_1) h_o^*(\mathbf{r}-\mathbf{r}_2) \\
& + i^n \iint d^2\mathbf{r}_1 d^2\mathbf{r}_2 \left[d^2\mathbf{k} I_c(\mathbf{k}) e^{i\mathbf{k}\cdot(\mathbf{r}_1-\mathbf{r}_2)} \right] T(\mathbf{r}_1) T^*(\mathbf{r}_2) h_o(\mathbf{r}-\mathbf{r}_1) h_s^*(\mathbf{r}-\mathbf{r}_2).
\end{aligned} \tag{B.4}$$

Finally, using the Fourier relation between $\Gamma_i(\cdot)$, the mutual intensity of the illumination, and the aperture intensity [78], i.e., $\Gamma_i(\Delta\mathbf{r}) = \Im[I_c(\mathbf{k})]$, Eq. (B.4) becomes

$$\begin{aligned}
I(\mathbf{r}; n\pi/2) = & \iint d^2\mathbf{r}_1 d^2\mathbf{r}_2 \Gamma_i(\mathbf{r}_1-\mathbf{r}_2) T(\mathbf{r}_1) T^*(\mathbf{r}_2) h_o(\mathbf{r}-\mathbf{r}_1) h_o^*(\mathbf{r}-\mathbf{r}_2) \\
& + \iint d^2\mathbf{r}_1 d^2\mathbf{r}_2 \Gamma_i(\mathbf{r}_1-\mathbf{r}_2) T(\mathbf{r}_1) T^*(\mathbf{r}_2) h_s(\mathbf{r}-\mathbf{r}_1) h_s^*(\mathbf{r}-\mathbf{r}_2) \\
& + (-i)^n \iint d^2\mathbf{r}_1 d^2\mathbf{r}_2 \Gamma_i(\mathbf{r}_1-\mathbf{r}_2) T(\mathbf{r}_1) T^*(\mathbf{r}_2) h_s(\mathbf{r}-\mathbf{r}_1) h_o^*(\mathbf{r}-\mathbf{r}_2) \\
& + i^n \iint d^2\mathbf{r}_1 d^2\mathbf{r}_2 \Gamma_i(\mathbf{r}_1-\mathbf{r}_2) T(\mathbf{r}_1) T^*(\mathbf{r}_2) h_o(\mathbf{r}-\mathbf{r}_1) h_s^*(\mathbf{r}-\mathbf{r}_2).
\end{aligned} \tag{B.5}$$

Thus, the sub-equation in (B.2) is followed by identifying the four terms with those in Eq. (B.5). Although Eq. (B.5) has been used intensively to study the image formation under partially coherent illumination [89, 187], it is rarely used in solving the inverse problem to recover the sample transmission, T , due to high computational complexity. For example, consider a transmission map T of $N \times N$ pixels and all kernels Γ_i, h_o, h_s of $P \times P$ pixels. Computing intensity I requires $O(N^2 P^4)$ operations, which would be problematic for large values of N and P .

Although we have four unknowns with four intensity measurements $I(\mathbf{r}; n\pi/2)$ with $n=0,1,2,3$, there is still an ambiguity in resolving I_1 and I_2 since the same combination $I_1 + I_2$ appears in all terms. Note that C_3 and C_4 are conjugated to one another. Solving only for one of them is sufficient. C_3 can be obtained precisely from 4 frames as

$$C_3(\mathbf{r}) = (1/2) \left\{ \left[I(\mathbf{r}; 0) - I(\mathbf{r}; \pi) \right] + i \left[I(\mathbf{r}; -\pi/2) - I(\mathbf{r}; \pi/2) \right] \right\}. \tag{B.6}$$

An extra equation is needed to resolve I_1 and I_2 . Toward this end, we assume the illumination to be close to spatially coherent, or that the field is quasi-plane wave, analog to quasi-monochromatic in the temporal domain. With this approximation, we obtain [32]

$$I_1 I_2 \approx C_3 C_4 = (1/4) \sqrt{[I(\mathbf{r}; 0) - I(\mathbf{r}; \pi)]^2 + [I(\mathbf{r}; 3\pi/2) - I(\mathbf{r}; \pi/2)]^2} \quad (\text{B.7})$$

$$\equiv P.$$

The sum S of I_1 and I_2 , which is also obtainable from four frames, is given as

$$I_1 + I_2 = [(I(\mathbf{r}; 0) + I(\mathbf{r}; \pi/2) + I(\mathbf{r}; \pi) + I(\mathbf{r}; 3\pi/2))/4] \quad (\text{B.8})$$

$$\equiv S.$$

Combining the product in Eqs. (B.7) and the sum in (B.8), we can solve for I_1 and I_2 explicitly as

$$I_1 = (S + \sqrt{S^2 - 4P})/2, \quad (\text{B.9})$$

$$I_2 = (S - \sqrt{S^2 - 4P})/2.$$

After all solutions for I_1, I_2, C_3 and C_4 are obtained, the measured phase ϕ_m is calculated using the definition as

$$\phi_m = \arg[J_1(\mathbf{r})] = \arg[I_1(\mathbf{r}) + C_4(\mathbf{r})]. \quad (\text{B.10})$$

B.3 Proof of Eq. (4.2)

Note that $J_1(\mathbf{r})$ is the sum of the intensity of the incident field, $I_1(\mathbf{r})$, and the temporal cross-correlation function at zero delays $\tau = 0$, $C_4(\mathbf{r})$, specifically,

$$J_1(\mathbf{r}) = I_1(\mathbf{r}) + C_4(\mathbf{r})$$

$$= \iint d^2\mathbf{r}_1 d^2\mathbf{r}_2 \Gamma_i(\mathbf{r}_1 - \mathbf{r}_2) T(\mathbf{r}_1) T^*(\mathbf{r}_2) [h_o(\mathbf{r} - \mathbf{r}_1) + h_s(\mathbf{r} - \mathbf{r}_1)] h_o^*(\mathbf{r} - \mathbf{r}_2). \quad (\text{B.11})$$

Note that the sum $h_o + h_s$ is a coherent PSF given by the Fourier transform of the aperture function of the objective of the microscope. This PSF is typically much narrower than Γ_i and

almost zero everywhere except around $\mathbf{r} \approx \mathbf{r}_1$. Ignoring the contribution from terms with $\mathbf{r} \neq \mathbf{r}_1$, Eq. (B.11) simplifies to

$$\begin{aligned} J_1(\mathbf{r}) &\approx \iint d^2\mathbf{r}_2 \Gamma_i(\mathbf{r}-\mathbf{r}_2) T(\mathbf{r}) T^*(\mathbf{r}_2) h_o^*(\mathbf{r}-\mathbf{r}_2) \\ &= \left\{ T \left[T \odot_{\mathbf{r}} (\Gamma_i h_o^*) \right]^* \right\}(\mathbf{r}). \end{aligned} \quad (\text{B.12})$$

As a side note, computing $J_1(\mathbf{r})$ now requires only $O[N^2 \log(N)]$ operations using the fast Fourier transform (FFT), which is much more effective than computing the intensity $I(\mathbf{r})$. Therefore, it is more efficient to solve for the transmittance $T(\mathbf{r})$ from $J_1(\mathbf{r})$ instead of from $I(\mathbf{r})$.

B.4 Solving for the optimal phase of interest

In order to solve the optimization problem in Eq. (4.5) in the main text, the limited memory Broyden–Fletcher–Goldfarb–Shanno with box constraint (L-BFGS-B)[100] algorithm was used. Our source code was developed in Matlab and the call for the L-BFGS-B subroutine was through a Matlab MEX-wrapper written by Stephen Becker (available at <https://github.com/stephenbeckr/L-BFGS-B-C>). At each iteration, only the value of the objective function $o[\phi_k(\mathbf{r})]$ and its derivative $\partial o / \partial \phi$, evaluated at the current estimation ϕ_k , are needed. The trade-off constant is fixed to $\lambda = 0.05$. The non-negative constraint is embedded inside the solver to make sure the solution does not have negative phase values with respect to the background. The algorithm is stopped when the updating error is less than a threshold, i.e. $|\phi(\phi_{k+1}) - \phi(\phi_k)| / \phi(\phi_k) \leq \varepsilon (= 10^{-8})$, or the maximum number of iterations has been reached. Here, the maximum number of iterations is set to 50. However, our experiments showed that very small improvements in reconstruction quality are made after 15-20 iterations. After finding the optimizer ϕ^* , we scale it by a scaling factor to match its dynamic range to

that of the input image ϕ_m . The dynamic range of each image is defined as the difference (in phase) between 2% and 98% percentiles of the values in the image. This normalization step makes the reconstruction more robust to modeling and approximation errors when the quasi-coherent assumption, $I_1 I_2 \approx C_3 C_4$, is made.

B.5 Halo-removal performance evaluation

Figure B.1 shows the halo-removing results for the different types of square pillars of 10, 20 and 40- μm width, under 20x and 40x magnifications. It can be seen that the correction for the halo artifacts and phase-underestimation is almost perfect up to 20- μm wide pillar at 20x and up to 10- μm wide pillar at 40x magnification. Improvement can be seen for larger pillars as well.

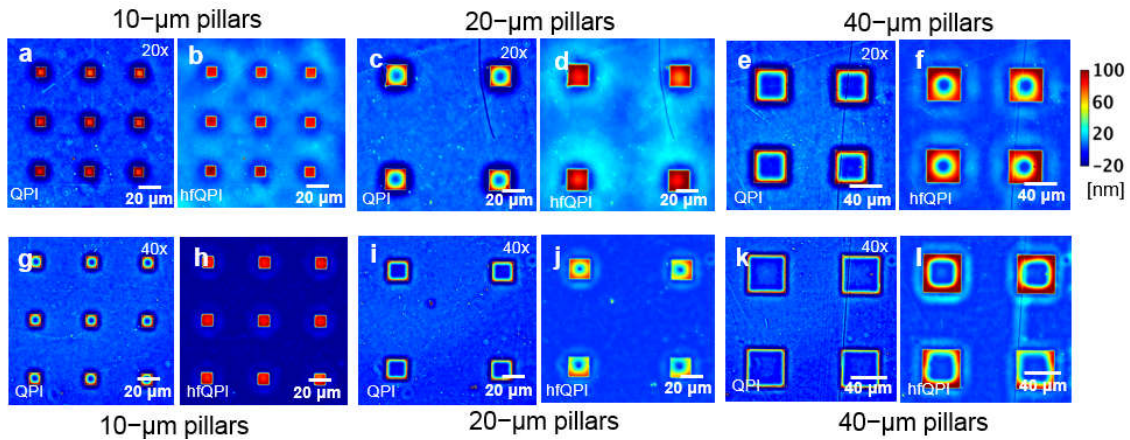


Figure B.1 (a)-(l) Raw QPI and hfQPI images of the micropillars of various sizes at different magnifications. It can be seen that the correction performance reduces when the dimension of the object get larger, or at higher magnifications. For example, at 20x magnification, 20- μm pillars can be fixed correctly. At 40x magnification, correct images of 10- μm pillars are obtained. Moderate improvement can be observed for larger pillars.

To quantify the amount of improvement, we use a metrics named “contrast ratio” (CR). Figure B.2 shows how this ratio is calculated. The ratio is calculated by dividing the area under the height profile (S_1) through the center of the pillar by the expected area under perfect reconstruction (S_2). A contrast ratio of 1.0 corresponds to a pillar with no halo. Figure B.2

shows a scatter plot for the contrast ratios before and after halo-removal. Improvement in the CR can be observed in all cases; i.e., all points lie above the $y = x$ black dash line. However, the improvement is more significant with 20x magnification compared to the 40x magnification.

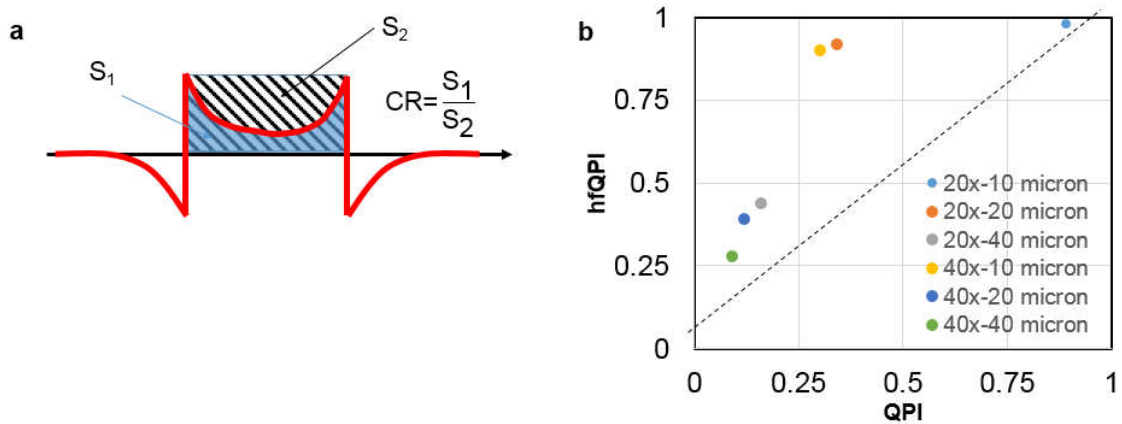


Figure B.2 (a) Calculating contrast ratio for the pillar sample. The ratio is computed by dividing the area under the central thickness profile of the pillar to the expected thickness profile. (b) Scatter plot of the contrast ratio for various sizes of the pillars at different magnifications evaluated using the original SLIM measurement and halo-corrected images.

B.6 Performance comparison between QPI, tQPI and hfQPI

Next, we compare the effects of the halo-removal process using histograms of phase value. Figure B.3(a)-(c) show an original QPI, tQPI, and hfQPI images, respectively. The tQPI image is computed by zeroing all negative phase values in the raw QPI image. Figure B.3(d) shows 256-histograms of the phase value obtained from these images. The maximum values of the histograms are obtained at the 0-phase bin for all of these images due to lots of contribution from the background. The histograms from the raw QPI and the tQPI are identical for positive phase value. The histogram of phase values from the hfQPI image are very close to those from the original QPI image and tQPI image for small positive phase value, e.g. $[0.0, 0.2]$ radians. However, more fractions of pixels are distributed towards the larger phase in the hfQPI image

than in the QPI or the tQPI image. These values are due to our correction, which boosts the underestimated values of the raw QPI image.

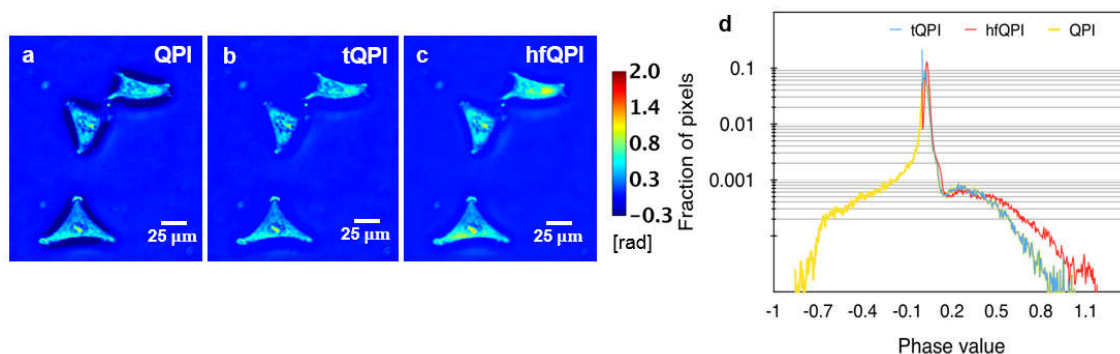


Figure B.3 (a)-(c) QPI, tQPI, and hfQPI images of HeLa cells. (d) Histogram distribution of the phase value in log 10-scale of these images.

B.7 Automatic cell segmentation for 20x HeLa cell images

The cells are automatically segmented from the phase map as follows. Here, we illustrate the process using an hfQPI image of a HeLa cell in Fig. B.4(a). First, measurement noise is removed from each image by filtering them with a Gaussian kernel and a standard deviation of 1 pixel. Second, the Sobel's edge detector is applied to find the edges of all cells (Fig. B.4(b)). Third, detected edges are dilated using line structure elements of length 4 at 0 and 90 degrees (Fig. B.4(c)). Finally, holes inside positive regions are filled and regions with less than 3000 pixels are eliminated (Fig. B.4(d)). The final segmentation result is shown in Fig. B.4(e).

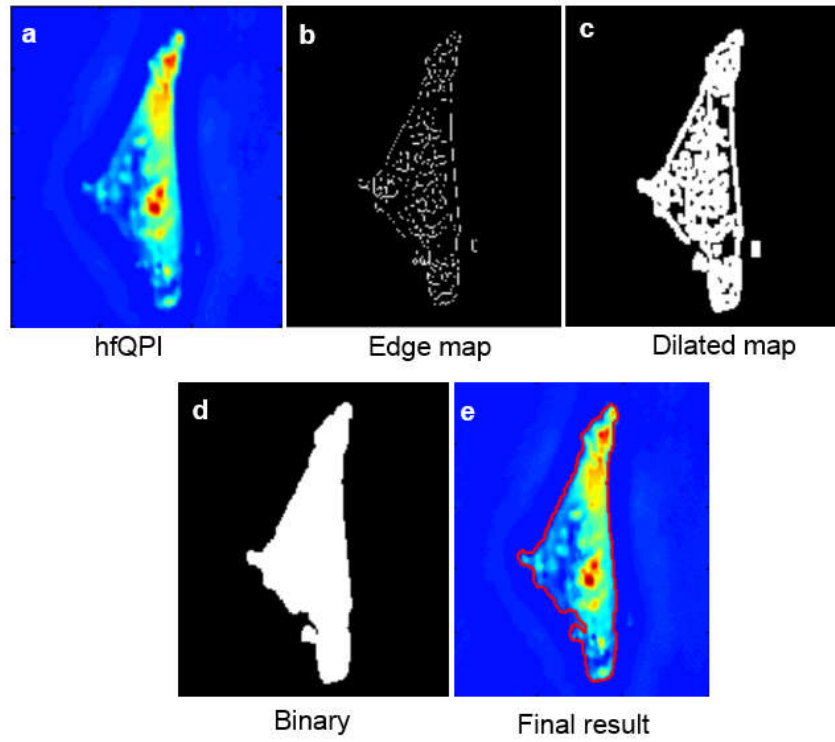


Figure B.4 Automatic segmentation diagram. (a) Input hfQPI image. (b) Edge map obtained by the Canny edge detector. (c) Dilated edge map. (d) Binary map of the cell obtained by filling all holes of (c). (e) Final segmentation results obtained by overlaying cell boundaries over the hfQPI image.

APPENDIX C: SUPPLEMENTAL INFORMATION FOR CHAPTER 5

C.1 Training the *texton* dictionary

Given a set of training SLIM images, we first obtain a *texton* dictionary that captures typical expressions of the tissue. Figure 5.4(a) shows how to retrieve this dictionary from a set of training SLIM images. First, each SLIM image ϕ is convolved with a Leung-Malik filter bank [137], consisting of L filters h_1, \dots, h_L to generate L filter responses $\phi * h_1, \dots, \phi * h_L$. The bank consists of 90 filters, $L = 90$, with 10 symmetric filters and 80 directional filters, oriented at 8 different angles over 5 scales. The directional filters are generated from the first and second-order derivative of Gaussian kernels with an elongation factor of 3. After this step, each pixel has a feature vector of dimension 90. A phase image in the training set generates totally 3072×3072 feature vectors. To reduce the size of the training set, a subset is formed from four million feature vectors randomly select from a larger pool of all feature vectors, accounting for 0.18% of the total number of feature vectors. Finally, the K -mean clustering algorithm with $K = 50$ is applied on this subset to divide it into K clusters with the centers of the clusters chosen as *textons*. Here, the value of K is chosen to balance between the complexity of the model and the estimation error, i.e., avoiding cases where there are not enough *textons* to capture texture variation or those when some *textons* come from clusters with a very few filter responses.

C.2 Random forest classifier for pixel classification

In order to do image segmentation, we classify each pixel in a query image (I) into one of three categories: gland, stroma and lumen using a random forest classifier and the pixel descriptor, i.e., feature vector. Here, the descriptor is a Gaussian weighted histogram of texton indices evaluated at the pixel location. Figure 5.5(b) shows how to calculate this descriptor. First, filter responses of I to the Leung-Malik filter bank are computed. Then, we apply vector quantization to associate the filter response at each pixel to the closest texton in the texton dictionary obtained in the previous step. For each pixel i , let us use t_i to denote the index of the closest texton in the dictionary. By definition, t_i can take one of the K following values $\{1, 2, \dots, K\}$. The output of this step is an indexing map where each pixel is assigned a number, telling the index of the closest texton. Using this indexing map, for each pixel i , we further obtain a histogram of texton indices evaluated over pixels in its neighborhood. In order to control the trade-off between the richness of texture information and locality of the descriptor, we apply a Gaussian weight to the histogram calculation where larger histogram contributions are given to pixels closer to the center of the neighborhood. By trial and error, we determine that a neighborhood radius of $\sigma = 45$ pixels is suitable to characterize the pixel. This radius corresponds to approximately $10 \mu\text{m}$ in the down-sampled image.

After obtaining descriptors for all pixels in the training set, we combine these feature vectors with their labels to train a random forest classifier to do automatic segmentation (Fig. 5.5(c)). The random forest classifier has shown success in several problems such as object segmentation [134, 188, 189], human-pose estimation [190, 191] and medical image analysis using magnetic resonant imaging [192-194] thanks to its ability to reduce the tree dependence with “feature bagging” and *bootstrap* sampling, i.e., random sampling with replacement. Here, we train an *extremely randomized* forest [195] of 50 trees. Our implementation is written in

MATLAB with the MexOpenCV wrapper that allows us to call OpenCV routines. The wrapper is obtained from <http://vision.is.tohoku.ac.jp/~kyamagu/software/mexopencv/>. The training set consists of 4.92 million histograms with two possible labels (“gland” or “stroma”). These histograms of textons are randomly sampled from a larger pool of 2.2 billion histograms. Each tree in the forests is trained on 11 randomly selected features (out of 50, the total number of textons). The number of trees is chosen to $T=50$. For each feature of interest, 100 possible thresholds are considered between the minimum and maximum of the feature values for splitting. At node n -th, the training data set of sample coming to it, S_n , is partitioned into the left set, S_l , and the right set, S_r , based on an optimal texton v_n and an optimal threshold t_n such that $S_l = \{s \in S_n | v_n < t_n\}$, and $S_r = S_n \setminus S_l$. Here, (v_n, t_n) are chosen to maximize the expected gain of information on category, i.e.

$$(v_n, t_n) = \arg \max_{v,t} [IG(v, t)] = H(S_n) - \frac{|S_l|}{|S_n|} H(S_l) - \frac{|S_r|}{|S_n|} H(S_r), \quad (C.1)$$

where $IG(v, t)$ is the information gain at the current node when the threshold t and the feature v are used. $H(S_n)$ is the entropy of set S_n , measuring its degree of class inhomogeneity. The training is recursive and terminated at leaf node when the maximum depth of 25 levels is reached or less than 20 training histograms are available. The training takes approximately 5-6 hours. After the training is completed, each leaf node l_m in the m -th tree contains two class likelihood values $p_{l_m}(gland), p_{l_m}(stroma)$ telling how many training histograms reached it that are from gland and stroma pixels, respectively. These values are used as the confidence value of the classifier produce by the m -th tree when the leaf node is reached.

After the random forest has been trained, automatic segmentation results can be obtained by classifying each pixel in the query image to either gland or stroma using its

descriptor (Fig. 5.5(d)). The optimal class g^* for the pixel is determined by summing the class likelihood values over all trees and picking the class which maximizes the summations, i.e.

$$g^* = \arg \max_g \left\{ \sum_{m=1}^T p_{l_m}(g) \right\}, \quad (\text{C.2})$$

where $g \in \{gland, stroma\}$. After an initial classification for all pixels of the input image, a post-processing step is applied to fine-tune the segmentation result, making it more stable to gland fusion, which is more popular at high grade cancer. This step is described in more detail in Section C.3.

C.3 Post-processing of the segmentation results

The output of the pixel classifier is usually noisy. The following procedure is applied to obtain good segmentation results and resolve the glandular fusion, which is more frequent in high-grade carcinoma.

- 1) Set aside all lumen pixels from the segmentation. Assign all remaining pixels with stroma likelihood less than 0.5 to gland pixels. Figure C.1(a) shows an example of the likelihood map.
- 2) Denoising gland map. First, we remove all small areas inside and between the glands that have less than 2000 pixels. Next, we perform an opening operation on the with a “disk” structure element with radius 20 pixels. Finally, we remove all glands that have less than 5000 pixels. The result of this step is shown in Fig. C.1(b). It can be seen that there are still several glandular regions detected a single gland due to small values of the stroma likelihood in connecting areas.
- 3) Watershed segmentation on denoised gland map. This step cuts small joining regions between the glands. First, the denoised gland map is inverted to obtain a non-gland map

(Fig. C.1(c)). Then, a distance transform is applied to the non-gland map to calculate the distance between each pixel in the non-gland map to the nearest non-zero pixel (Fig. C.1(d)). Next, the Watershed transform [196] is applied to the inverted distance map to obtain an over-segmentation result of the gland map into multiple regions (Fig. C.1(e)). Separating lines between neighboring regions is computed by subtracting the gland map (Fig. C.1(b)) to the watershed segmentation result. Then, a closing transform is applied to the map of separating line to make sure its width is at least 15 pixels (Fig. C.1(f)).

- 4) Evaluate the separation and recombine glands if needed. This step assesses each separating line produced by step 3. Then, the mean value of the stroma likelihood is evaluated over each separation line. Lines with a mean value of stroma likelihood more than 0.2 are kept. Otherwise, they are eliminated, and glands separated by them are rejoined to form a refined gland map (Fig. C.1(g)). Compared to Fig. C.1(b), this map has resolved several glands which have been incorrectly fused by a simple thresholding. Figure C.1(h) shows the final segmentation results.

C.4 GLM net for basal vs. non-basal classification

Training GLM net: Let $i = 1, \dots, N$ be N training samples with $x_1, \dots, x_N \in R^L$ are N training feature vectors. They are histograms of texton indices. Each histogram is an L -tuple vector in R^N with non-negative entries. The training labels of $y_i \in \{0, 1\}$ with $i = 1, \dots, N$, correspond to non-basal (0) and basal (1), respectively. Let us use Y and X to denote the random variables corresponding to the class and the feature vector. Also, $p(y|x; \theta) = p(Y = y|X = x; \theta)$ is the posterior that the class variable Y takes the label y given the observation $X = x$. The posterior is parameterized by the coefficient vector θ . Under logistic regression, we model the posterior distribution as

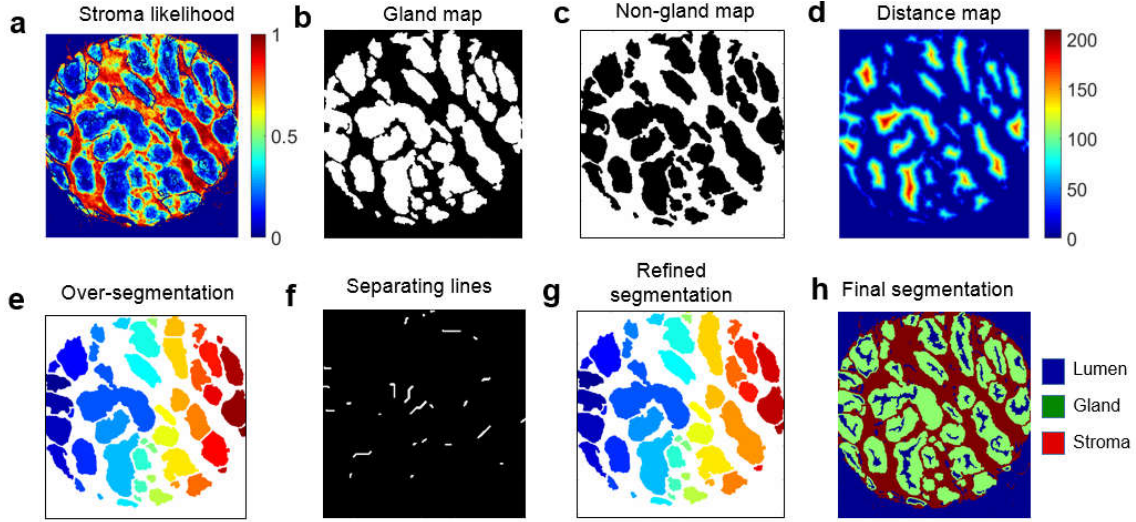


Figure C.1 Steps of image post-processing for automatic segmentation. (a) The stroma likelihood map produced by the RF classifier. (b) The raw binary gland map. (c) The raw binary non-gland map. (d) The distance map from each gland pixel to the nearest non-gland pixel. (e) The over-segmentation map produced by watershed segmentation. (f) The map of gland separating lines. (g) The refined segmentation map where some similar regions in (e) have been merged. (h) The final segmentation map.

$$\begin{aligned}
 p(1|x; \theta) &= \exp(\theta^T x) / [1 + \exp(\theta^T x)], \\
 p(0|x; \theta) &= 1 / [1 + \exp(\theta^T x)].
 \end{aligned} \tag{C.3}$$

The log-likelihood function of N observations $(x_1, y_1), \dots, (x_N, y_N)$, assuming that they are independent, can be written as

$$\begin{aligned}
 l(\theta) &= \sum_{i=1}^N \ln [p(y^i | x^i; \theta)] \\
 &= \sum_{i=1}^N \{y_i \ln [p(1|x^i; \theta)] + (1 - y_i) \ln [p(0|x^i; \theta)]\} \\
 &= \sum_{i=1}^N \{y_i \ln [p(1|x^i; \theta) / p(0|x^i; \theta)] + \ln [p(0|x^i; \theta)]\}.
 \end{aligned} \tag{C.4}$$

Replacing the definition of the posteriors in Eq. (C.3) into Eq. (C.4), we have

$$l(\theta) = \sum_{i=1}^N \{y_i \theta^T x - \ln [1 + \exp(\theta^T x)]\}. \tag{C.5}$$

To avoid overfitting caused by the high-dimensional and sparse training data, the GLMnet solves the following optimization problem with a regularizer on θ to obtain the optimal coefficient vector θ^\dagger :

$$\begin{aligned}\theta^\dagger &= \arg \min_{\theta} \left\{ -l(\theta) + \lambda \left[(1-\alpha) \|\theta\|_2^2 + \alpha \|\theta\|_1 \right] \right\} \\ &= \arg \min_{\theta} \left\{ \sum_{i=1}^N \left\{ -y_i \theta^T x + \ln \left[1 + \exp(\theta^T x) \right] \right\} + \lambda \left[(1-\alpha) \|\theta\|_2^2 + \alpha \|\theta\|_1 \right] \right\}.\end{aligned}\quad (\text{C.6})$$

See [144] for more details. Here, the coefficient λ controls the amount of regularization applied on θ compared to the negative log-likelihood. The mixing coefficient α defines the *elastic-net* penalty which bridges the gap between the *lasso* ($\alpha=1$) and ridge regression ($\alpha=0$). It is known generally that the lasso prefers a sparse small set of coefficients. It picks a few coefficient while ignoring the rest.

After all the pixel descriptors have been computed, the histogram of texton indices from pixels randomly selected from different regions manually labeled are selected to test the GLMnet. The manual labelings are shown in Fig. C.2 and C.3 and described in detail in the next section.

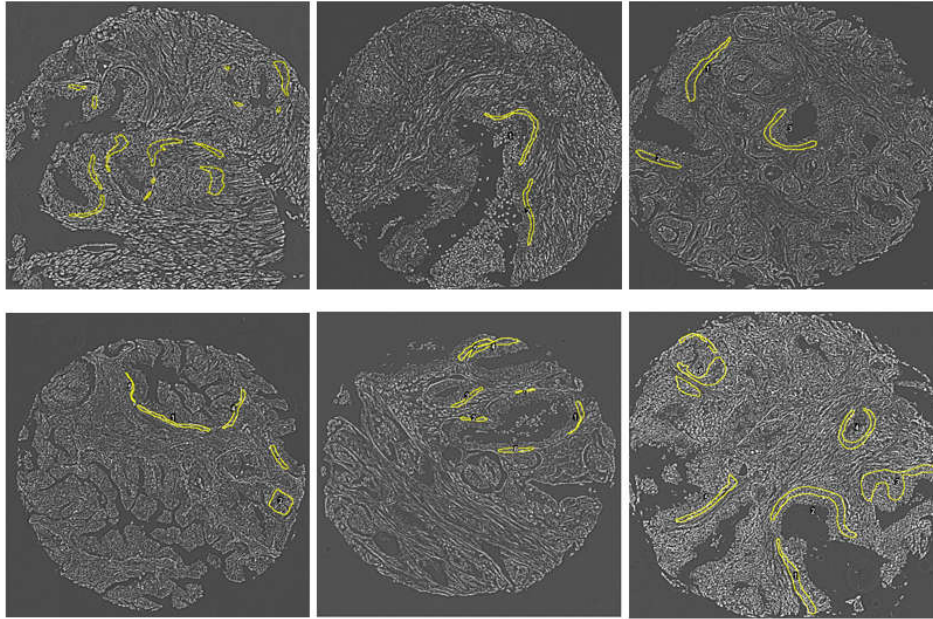


Figure C.2 Regions marked as basal.

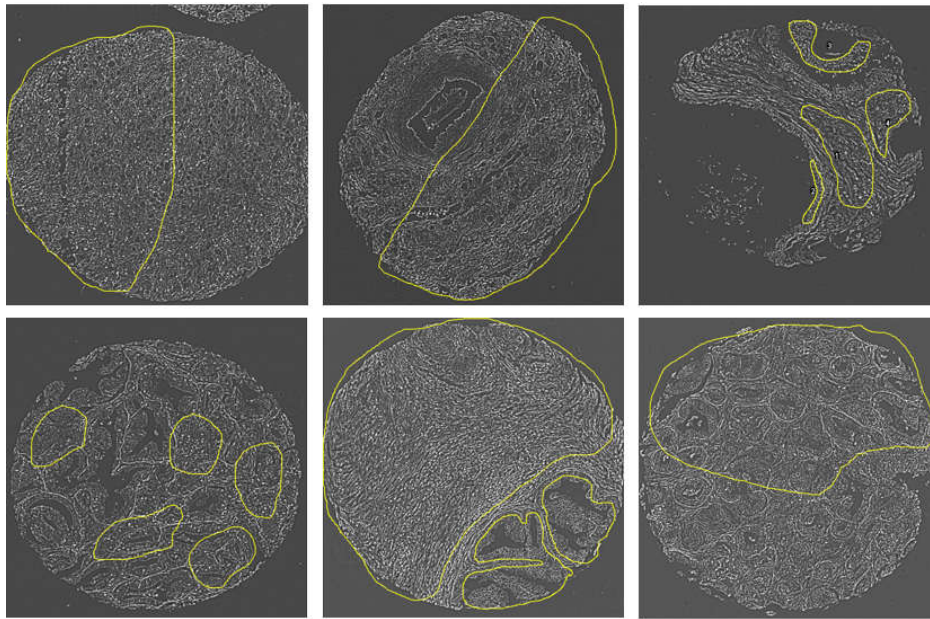


Figure C.3 Regions marked as non-basal.

Here, the manual markings are marked based on the H&E images for reliability. Totally, 96,000 pixels are used to test the GLMnet. Among them, 14,000 pixels are basal. 82,000 pixels are non-basal. Each pixel descriptor has a dimension of 1,024. When all the pixel

descriptors have been computed, the histogram of texton indices from pixels randomly selected from different regions manually labeled are used to train and test the GLMnet.

C.5 Features for Gleason grade 3 vs. Gleason grade 4 classification

The following features are extracted from each ROI and used for automatic Gleason grading.

Only some features are explained here for brevity, as follows:

- Gland distortion (Fig. 5.9(a)): the distortion of a gland is defined as the ratio between its perimeter and the square root of its area, scaled by the factor of $1/\sqrt{2\pi}$. The smaller values of the distortion correspond to more circular glands. Elongated glands have distortion values larger than 1. A distortion value of 1 is obtained for a circular gland. Average distortion value for the whole ROI is evaluated by averaging distortion values of glands inside the ROI.
- The average number of lumen (Fig. 5.9(b)): this feature is designed to capture the cribriform pattern that characterizes Grade 4. In Grade 4, glands fuse to each other, creating larger glands with multiple lumen areas contributed by those of individual gland. A value of zero is given if a gland has no area. A fractional average number of lumens is also possible.
- Average stroma anisotropy (Fig. 5.9(c)): This feature captures the potential effects of reactive stroma in the progression of tumorigenesis [197, 198]. This quantity measures the angular uniformity of forward scattering in light-tissue interaction. A lower value of g means more isotropic scattering and vice versa. The anisotropic factor is computed for all pixels in the image using the scattering-phase theorem as [199].
- The fusing ratio (Fig. 5.9(d)): this feature is the ratio of total area of all glands with at least two lumens to the total area of all glands in the region of interest. It characterizes

the cribriform pattern and gland fusion. However, it is more robust than the average number of lumen feature since fused glands with small areas have less impact than those with large areas.

$$g = 1 - \left(\frac{\langle |\nabla \phi(\mathbf{r})|^2 \rangle_{\mathbf{r}}}{2k_o^2 \langle \Delta \phi^2(\mathbf{r}) \rangle_{\mathbf{r}}} \right). \quad (\text{C.7})$$

After the anisotropic factor is obtained for all pixels in the image, the stroma anisotropy for the whole field of view is computed as an average of the quantity, evaluating over a thin layer, surrounding segmented glands, as shown in Fig. 5.9(d). The thickness of this thin layer is chosen to be around 10 μm .

- The coefficient of variation of gland area (Fig. 5.9(d)): this ratio of the standard deviation of all gland area to the mean of all gland area. The ratio is smaller for regions of interests that have more uniformity in gland areas, a criteria for Gleason grade 3.

APPENDIX D: SUPPLEMENTAL INFORMATION FOR CHAPTER 6

D.1 Extracting phase gradient from intensity image

The intensity image at modulation ϕ_m is given as

$$I_n(\mathbf{r}) = I(\mathbf{r}) + I(\mathbf{r} + \delta\mathbf{r}) + 2|\gamma(\mathbf{r}, \delta\mathbf{r})| \cos[\Delta\phi(\mathbf{r}) + \phi_n], \quad (\text{C.8})$$

where $\Delta\phi = \phi(\mathbf{r} + \delta\mathbf{r}) - \phi(\mathbf{r}) \approx \nabla_x(\phi)\delta x$ is the phase difference of interest, and $\nabla_x\phi$ is the gradient of the phase of the image field in the x-direction. The spatial shift δx is the transverse displacement introduced by the DIC prism, estimated experimentally from measurements of the test samples. The quantity $\gamma(\mathbf{r}, \delta\mathbf{r})$ is the *mutual intensity*, i.e., the temporal cross-correlation function between these two fields, evaluated at zero delay, $\gamma(\mathbf{r}, \delta\mathbf{r}) = \langle U^*(\mathbf{r})U(\mathbf{r} + \delta\mathbf{r}) \rangle_t$. Combining the four intensity frames, we obtain the phase gradient as

$$\nabla_x\phi(\mathbf{r}) = \arg\left\{ [I_4(\mathbf{r}) - I_2(\mathbf{r})], [I_3(\mathbf{r}) - I_1(\mathbf{r})] \right\} / \delta x. \quad (\text{C.9})$$

D.2 SLM calibration procedure

We calibrate the SLM gray values vs. modulating phase by imaging the sample plane without the sample, i.e., $\Delta\phi(\mathbf{r}) = 0$. First, we acquire intensity images, I_g , with g corresponding to the SLM grayscale values on an 8-bit dynamic range. As a side note, one can further extend the resolution of the SLM modulation to one more bit by mixing discrete values on the SLM using a “checkerboard” pattern on the SLM (Fig. D.1(a)). More specifically, the modulation value set to the pixel x is given as

$$S_{g+0.5}[x] = \begin{cases} g, & \text{if } x \text{ is even,} \\ g+1, & \text{if } x \text{ is odd.} \end{cases} \quad (\text{C.10})$$

The intensity image I_g (Fig. D.1(b)) recorded by the camera for the grayscale value g is

$$I_g = I_1 + I_2 + 2\sqrt{I_1 I_2} \cos[\phi(g)], \quad (\text{C.11})$$

where I_1 is the intensity of the modulated field, I_2 is the intensity of the un-modulated field,

and $\phi(g)$ is the phase modulation of interest. Using the experimentally measured $I(g)$

curve (Fig. D.1(b)) for $g \in [0, 255]$, we obtain $\cos[\phi(g)] = \{[I_g - \alpha]/\beta\}$, where

$\alpha = \{[\max_g [I_g] + \min_g [I_g]]/2\}$, and $\beta = \{[\max_g [I_g] - \min_g [I_g]]/2\}$. Next, we use a

Hilbert transform to obtain the complex analytic signal associated with the cosine signal, the

imaginary part of which is $\sin[\phi(g)] = H\{[I_g - \alpha]/\beta\}$. Here, $H(\cdot)$ denotes the operator to

compute the Hilbert transform from a real part of a complex analytic signal to get the

imaginary part. Combining the $\text{sine}(\cdot)$ and the $\text{cosine}(\cdot)$ signals, we obtain

$$\phi(g) = \arg\{[I_g - \alpha]/\beta, H\{[I_g - \alpha]/\beta\}\}. \quad (\text{C.12})$$

This $\phi(g)$ curve represents the desired SLM calibration. Note that there are many sets of four

points that we can choose for the working phase shift. Experimentally, we choose the portion

of the curve that is most linear (see Fig. D.1(b)). From this curve, the $\pi/2$ sequence is chosen

to meet two complementary criteria: maximum visibility and minimal phase error. To

maximize the visibility, we evaluate several points around each amplitude maximum and

choose the calibration where the steps are nearest to multiples of $\pi/2$. When multiple peaks are

present, we prefer the peak most closely resembling a sinusoid (Fig. D.1(b)), 2nd peak at $g =$

440), which corresponds to a linear $\phi_m(g)$ behavior. Our calibrated phase curve $\phi(g)$ is shown

as the red profile in the inset of Fig. D.1(b).

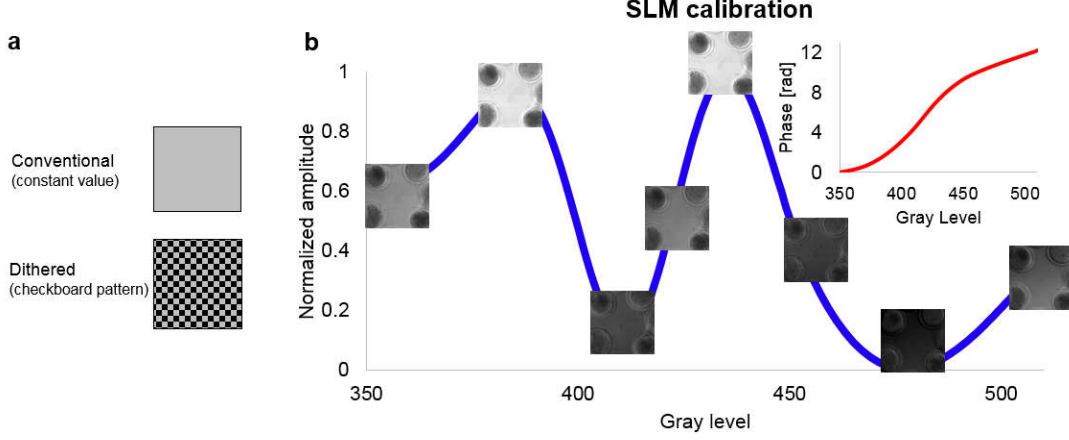


Figure D.1 SLM calibration. (a) Conventional and checkerboard pattern displayed on the SLM. (b) Measured amplitude response (blue) and the reconstructed phase modulation curves (red).

D.3 2D image formation in GLIM

Consider a thin sample with a transmission function $T(\mathbf{r}_\perp)$, and the total incident field on it consists of two cross-polarizations. They generate two sample fields on the camera plane of

$$U_1(\mathbf{r}_\perp) = \{[U_i(\mathbf{r}_\perp)T(\mathbf{r}_\perp)] \odot_{\mathbf{r}_\perp} h_o\}(\mathbf{r}_\perp), \quad \text{and} \quad U_2(\mathbf{r}_\perp) = \{[U_i(\mathbf{r}_\perp)T(\mathbf{r}_\perp - \delta\mathbf{r})] \odot_{\mathbf{r}_\perp} h_o\}(\mathbf{r}_\perp),$$

where h_o is a point-spread function characterizing the limited-aperture diffraction of the objective. The temporal cross-correlation function at zero delays, $\tau = 0$, or the mutual intensity function of these two sample fields is

$$\begin{aligned} \gamma(\mathbf{r}_\perp, \delta\mathbf{r}) &= \langle U_1(\mathbf{r}_\perp)U_2^*(\mathbf{r}_\perp) \rangle_t \\ &= \int \Gamma_i(\mathbf{r}'_\perp - \mathbf{r}''_\perp) T(\mathbf{r}'_\perp) T^*(\mathbf{r}''_\perp - \delta\mathbf{r}) h_o(\mathbf{r}_\perp - \mathbf{r}'_\perp) h_o^*(\mathbf{r}_\perp - \mathbf{r}''_\perp) d^2\mathbf{r}'_\perp d^2\mathbf{r}''_\perp. \end{aligned} \quad (\text{C.13})$$

Here, $\Gamma_i(\cdot)$ is the mutual intensity function of the illumination at the sample plane [78]. When the numerical aperture of the object, NA_o , is large enough so that the spatial resolution is finer than any structure of the interest in the sample, the PSF, h_o , can be approximated as $h_o(\mathbf{r}_\perp) \approx \delta^{(2)}(\mathbf{r}_\perp)$, simplifying Eq. (C.13) into

$$\gamma(\mathbf{r}_\perp, \delta\mathbf{r}) = \Gamma_i(\Delta\mathbf{r} = \mathbf{0})T(\mathbf{r}_\perp)T^*(\mathbf{r}_\perp - \delta\mathbf{r}). \quad (\text{C.14})$$

Consequently,

$$\Delta\phi(\mathbf{r}_\perp) = \arg[\gamma(\mathbf{r}_\perp, \delta\mathbf{r})] \approx \phi(\mathbf{r}_\perp) - \phi(\mathbf{r}_\perp - \hat{\mathbf{x}}\delta x), \quad (\text{C.15})$$

with $\phi = \arg(T)$, which means that GLIM gives the correct phase difference of the sample irrespective of the coherence of the illumination. This is different from other common-path interferometry methods where the measurement reduction is highly dependent on NA_{con} ; see [35, 81].

D.4 3D image formation in GLIM

As shown above, small values of NA_{con} give precise value of the phase gradient. In this section, we focus on the other regime of large NA_{con} , where the depth sectioning is best thanks to the maximum angular coverage. Under the 1st order Born approximation [186], two sample fields coming to the camera plane can be written as

$$\begin{aligned} U_1(\mathbf{r}) &= U_i(\mathbf{r}) - \beta_o^2 \{ [U_i\chi] \odot_{\mathbf{r}} g \}(\mathbf{r}), \\ U_2(\mathbf{r}) &= U_i(\mathbf{r}) - \beta_o^2 \{ [U_i\chi(\mathbf{r} + \delta\mathbf{r})] \odot_{\mathbf{r}} g \}(\mathbf{r}). \end{aligned} \quad (\text{C.16})$$

Here, $g(\mathbf{r})$ is the propagation kernel, defined by the microscope's objective given by [38] as

$$g(\mathbf{r}) \approx i\mathcal{F}_{\mathbf{k}_\perp}^{-1} \{ e^{iqz} \text{circ}[k_\perp / (\beta_o \text{NA}_o)] \} / (2\bar{n}\beta_o). \text{ Again, } \beta_o \text{ is the wavenumber in free-space.}$$

Next, $\mathcal{F}_{\mathbf{k}_\perp}^{-1}(\cdot)$ is the inverse two-dimensional Fourier transform operator, and $\text{circ}(x)$ is the

rectangular function, defined as $\text{circ}(x) = 1$ if $x \leq 1$ and 0, otherwise. (\mathbf{k}_\perp, q) is a 3D

wavevector constrained by the dispersion relation as $q = \sqrt{\beta_o^2 - k_\perp^2}$. Finally, “ $\odot_{\mathbf{r}}$ ” is the three-

dimensional convolution operator in the spatial domain and $\chi(\mathbf{r})$ is the susceptibility of the

sample. Hence, the temporal cross-correlation function between the two fields, at zero delay, $\tau = 0$, becomes

$$\begin{aligned}\gamma(\mathbf{r}, \delta\mathbf{r}) &= \langle U_1(\mathbf{r})U_2^*(\mathbf{r}) \rangle_t \\ &= \Gamma_i(\mathbf{r}, \mathbf{r}; 0) - \beta_o^2 \int \Gamma_i(\mathbf{r}, \mathbf{r}'; 0) \chi^*(\mathbf{r}') g^*(\mathbf{r} - \mathbf{r}') d^3\mathbf{r}' \\ &\quad - \beta_o^2 \int \Gamma_i(\mathbf{r}'', \mathbf{r}; 0) \chi(\mathbf{r}'' - \hat{\mathbf{x}}\delta x) g(\mathbf{r} - \mathbf{r}'') d^3\mathbf{r}'',\end{aligned}\quad (\text{C.17})$$

where Γ_i is the mutual intensity function of the illumination, which only depends on the coordinate difference under the statistically homogeneous assumption [38, 185], namely, $\Gamma_i(\mathbf{r}_1, \mathbf{r}_2; 0) = \Gamma_i(\mathbf{r}_1 - \mathbf{r}_2) = \int S_c(\mathbf{k}_\perp) e^{i[\mathbf{k}_\perp \cdot (\mathbf{r}_1 - \mathbf{r}_2) + q(z_1 - z_2)]} d^2\mathbf{k}_\perp$. Here, S_c is the aperture intensity of at the condenser aperture plane. Using this property of Γ_i , Eq. (C.17) can be simplified to

$$\gamma(\mathbf{r}, \delta\mathbf{r}) = \Gamma_i(\mathbf{0}; 0) - \beta_o^2 \left\{ \chi \odot_{\mathbf{r}} \left[(\Gamma_i g^*)(\mathbf{r}) + (\Gamma_i^* g)(\mathbf{r} - \hat{\mathbf{x}}\delta x) \right] \right\}. \quad (\text{C.18})$$

Assuming a non-absorbing object with a real χ , with a uniform unit-amplitude intensity distribution at the condenser aperture, with $g(\mathbf{r}) \approx i\mathcal{F}_{\mathbf{k}_\perp}^{-1} \left\{ e^{iqz} \text{circ} \left[k_\perp / (\beta_o NA_o) \right] \right\} / (2\bar{n}\beta_o)$, and $\Gamma_i(\mathbf{r}) \approx \mathcal{F}_{\mathbf{k}_\perp}^{-1} \left\{ e^{iqz} \text{circ} \left[k_\perp / (\beta_o NA_c) \right] \right\}$, it is clear that the function $(\Gamma_i g^*)$ is purely imaginary.

Therefore, $(\Gamma_i^* g) = -(\Gamma_i g^*) = \text{Im}(\Gamma_i^* g)$. As a result,

$$\begin{aligned}\nabla_x \phi(\mathbf{r}) &= \arg[\gamma(\mathbf{r}, \delta\mathbf{r})] / \delta x = \beta_o^2 \arctan \left\{ \chi \odot_{\mathbf{r}} \text{Im} \left[(\mu_i g^*)(\mathbf{r}) - (\mu_i g^*)(\mathbf{r} - \hat{\mathbf{x}}\delta x) \right] \right\} / \delta x \\ &\approx \beta_o^2 \left(\chi \odot_{\mathbf{r}} \text{Im} \left[(\mu_i g^*)(\mathbf{r}) - (\mu_i g^*)(\mathbf{r} - \hat{\mathbf{x}}\delta x) \right] \right) / \delta x,\end{aligned}\quad (\text{C.19})$$

where $\mu_i(\mathbf{r}) = \Gamma_i(\mathbf{r}; 0) / \Gamma_i(\mathbf{0}; 0)$, the complex degree of spatial coherence of the incident field.

Figure D.2(a) shows a $k_x - k_z$ cross-section of the imaginary part of the computed transfer function (TF) of the GLIM system for different values of the NA_{con} . This TF is obtained by

3D Fourier transforming the Point Spread Function (PSF),

$h(\mathbf{r}) = \text{Im} \left[(\mu_i g^*)(\mathbf{r}) - (\mu_i g^*)(\mathbf{r} - \hat{\mathbf{x}}\delta x) \right]$, whose cross-sections are shown in Fig. D.2(b) &

(c), respectively. Since the PSF is odd, the TF is purely imaginary. The absolute value of the TF vanishes at $k_x = 0$, since a constant signal in the x-direction is filtered out by the gradient operator. Therefore, there is a missing area around $k_x = 0$ not covered by the TF. This region of missing frequencies is similar to the “missing cone” problem known in diffraction tomography [200]. Resolving this area requires rotating the sample [16] or using additional priors, e.g., smoothness constraint [201], [202]. Larger NA_{con} reduces the size of the missing cone, allowing the system to record more frequency components. The dashed red lines in Fig. D.2(a) show the limiting numerical aperture of the objective. The larger the NA_{con} , the more transverse frequencies are captured by the TF. More importantly, around $\text{NA}_{\text{con}}/2$, more k_z frequency bandwidth is captured with $\text{NA}_{\text{con}}=0.55$ compared to those with $\text{NA}_{\text{con}}=0.09$, which essentially means that depth sectioning improves when NA_{con} increases. Figure D.2(b) shows multiple $x - z$ cross-sections of the PSF for different values of NA_{con} . Clearly, the axial elongation of the PSF decreases for larger NA_{con} . The improvement in depth sectioning for increasing NA_{con} also reduces the ringing effects since less non-specific information from one z-plane is propagated into neighboring planes, as shown by the x-y cross-section in Fig. D.2(c). Clearly, the diffraction ringing phenomenon is suppressed when NA_{con} increases.

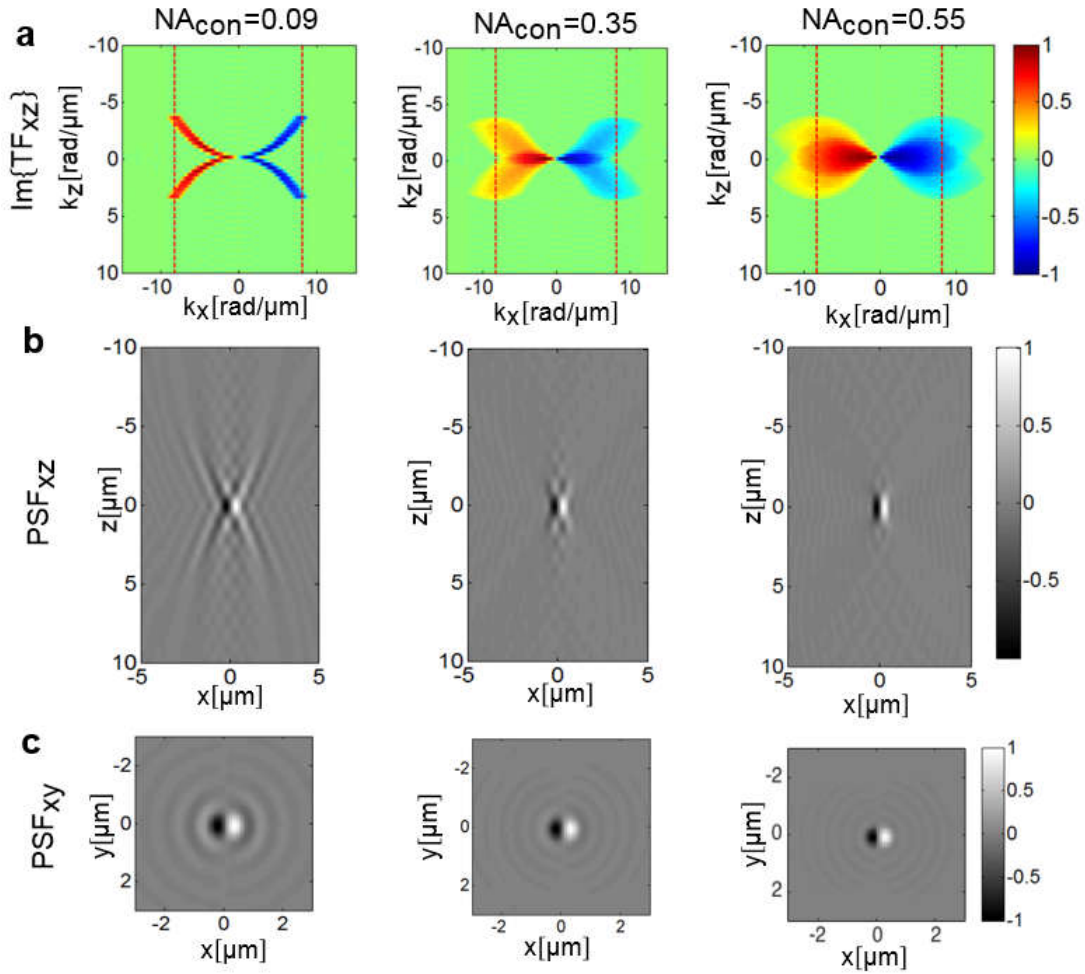


Figure D.2 Transfer function (TF) and point spread function (PSF) of GLIM. (a) The k_x - k_z cross-sections of the TF. The dashed vertical lines denote the limiting numerical aperture of the microscope objective. (b) x - z and (c) x - y cross-sections of the PSF at different values of NA_{con} .

Figure D.3(a) shows x - z cross-sections of GLIM measurements of 4.5- μm beads vs. NA_{con} . The microscope scanned the beads in the axial direction over an interval of $[-100 \mu\text{m}, 100 \mu\text{m}]$ with a step size of $\Delta z = 0.05 \mu\text{m}$. Here, the same dynamic range is applied to all images to study the change in contrast vs. NA_{con} . Figure D.3(b) has all images' contrasts normalized to assess depth sectioning better. Clearly, reducing the coherence of the illumination by increasing NA_{con} improves the depth sectioning of the GLIM measurement at

the cost of contrast reduction. Such improvement in depth sectioning is crucial when measuring optically thick samples.

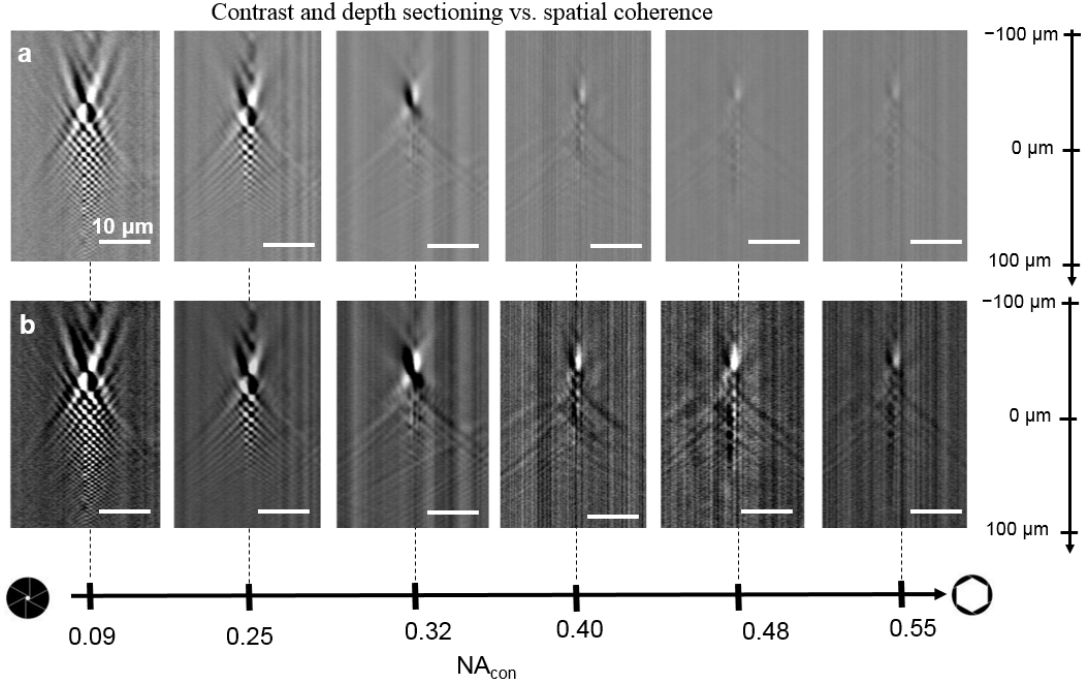


Figure D.3 Contrast and depth sectioning vs. spatial coherence. (a) Raw x - z cross-sections of the GLIM images of 4.5- μm beads immersed in oil for different values of NA_{con} with the same dynamic range applied. It can be seen that the contrast reduces in accordance with the spatial coherence of the illumination. (b) Contrast-enhance images of the images in (a). Clearly, the depth sectioning improves when the spatial coherence is smaller.

D.5 Depth sectioning improvement of GLIM with spatial filtering

In order to improve the optical sectioning, we removed the low-frequency components from our data using a high-pass filter. Steps of our methods are summarized in Fig. D.4. First, we removed the shading artifact using Wiener deconvolution [203]. Since

$h(\mathbf{r}) = \text{Im}[(\mu_i g^*)(\mathbf{r}) - (\mu_i g^*)(\mathbf{r} - \hat{\mathbf{x}}\delta x)]$, the transfer function is

$\tilde{h}(\mathbf{k}) = 2i \sin(k_x \delta x / 2) \mathcal{F}\{\text{Im}(\mu_i g^*)\}(\mathbf{k})$. The Wiener deconvolution result of the

susceptibility can be obtained in the frequency domain as

$$\tilde{\chi}_{\text{weiner}}(\mathbf{k}) = \frac{-2i \sin(k_x \delta x / 2) \delta x}{\beta_o^2 [4 \sin^2(k_x \delta x / 2) + \varepsilon]} \mathcal{F}[\nabla_x \phi](\mathbf{k}), \quad (\text{C.20})$$

where ε is a small number, set to be 10^{-4} to avoid amplifying frequency components with small SNRs. To further improve the axial resolution, it is necessary to significantly suppress the low-frequency components in $\chi_{weiner}(\mathbf{r})$. We achieve this by applying high-pass filtering in the x - y domain for each recorded z -image. In each dimension (x and y), a convolution with a finite-length impulse response (FIR), chosen as $h_{hp}(x) = [0.25, -0.25, 0, -0.25, 0.25]$, is applied. The result of this high pass filtering, $\chi_{hp}(\mathbf{r})$, has most of the small transverse frequencies suppressed and, as a result, yields very good depth sectioning. Note that this high-pass filtering step can be combined with the Wiener deconvolution step since both are linear operators. Also, there is no need to perform any z -processing in our proposed method. This allows the processing to be done effectively by interlacing with image acquisition. After filtering, we applied a $\log[\text{abs}(\cdot)]$ transform to increase the contrast of the retained high-frequency components in the output image. To further suppress the background noise, we keep signals with amplitude within $[-5.0, 0.0]$ only. Finally, to smooth the image and remove high-frequency oscillations in the image due to missing small transverse frequencies, we further apply bilateral filtering [204] on the transformed results. Figure D.4 summarizes these steps with illustration on the impacts of the processing. Clearly, the output of the post-processing has better depth sectioning compared to the input image. Different structures and materials, which are not visible in the raw input, appear nicely in the output.

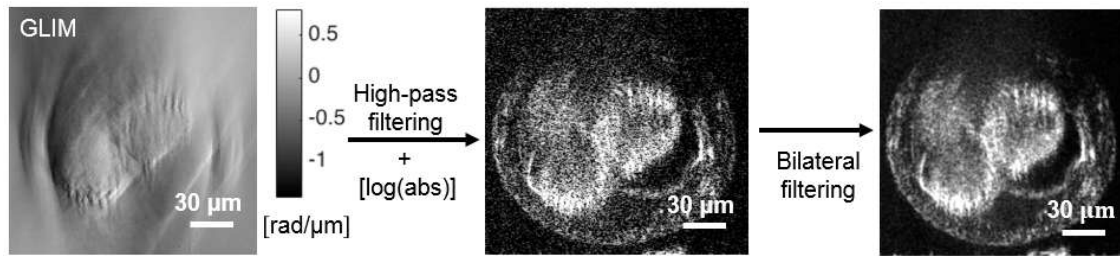
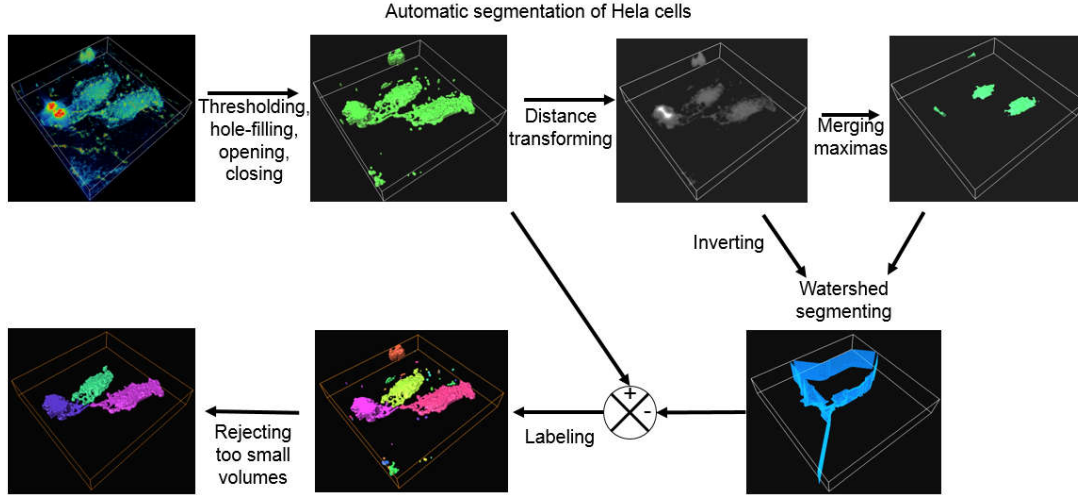


Figure D.4 Filtering scheme to improve depth sectioning. The raw GLIM data is filtered to suppress the low-frequency components before bilateral filtering to reduce the high-frequency oscillations due to the missing low-frequency and recover structures of the object.

D.6 3D automatic segmentation of the HeLa cell with GLIM

Automatic segmentation is crucial to obtain high-throughput, consistent, objective metrics on the cells during their development cycle. We describe our automatic segmentation procedure in Fig. D.5. An input stack of the raw GLIM data consists of three cells with one of them in mitosis. First, the input is thresholded, hole-filtered, and morphologically transformed with the *opening* and *closing* with a $3 \times 3 \times 3$ structure element. These steps eliminate spurious background noise, reduce the surface roughness, fill out gaps due to internal structures of the cells, and most importantly, generate a 3D binary map where a value of 1 is assigned to voxels inside the cells, and 0, otherwise. Then, the watershed algorithm [196] is used to produce separating barriers, splitting the binary map into multiple regions corresponding to different cells. The watershed algorithm uses an inverted distance map and some seeds generated as local maxima of the distance map. Here, the distance map is a scalar field where the value at each voxel is 0 if its value of the binary map is 0. On the other hand, when the binary is 1, the value at the voxel corresponds to the closest distance between it and the nearest boundary voxel. Next, the separating barriers are subtracted from the binary map and labels are given to connecting volumes in the resulting map. Finally, we eliminate regions with volume measurement smaller than $900 \mu\text{m}^3$ or 300,000 voxels, equivalently.



D.7 Drymass measurement using GLIM

R. Barer [106] showed that in two cases of serum albumin and serum globulin, the following relation holds with good accuracy: $\alpha = \Delta n / C = [(n_p - n_s) / C]$. Here, α is the refractive index increment, C is the number of grams of dry protein per 100 ml, and n_p, n_s are the refractive indices of the protein and the solvent, respectively. Note that this relation holds in the 3D settings where these quantities are functions of the 3D coordinate \mathbf{r} . The quantity C is the mass density of dry protein, calculated as $(dm/dV)(\mathbf{r})$, where m is the total dry mass of the cell, and V is its volume. Therefore,

$$m = \int_{\mathbf{r} \in V} dm(\mathbf{r}) = \int_{\mathbf{r} \in V} \frac{\Delta n(\mathbf{r}) dV(\mathbf{r})}{\alpha(\mathbf{r})} = \int_{\mathbf{r} \in V} \frac{\Delta n(\mathbf{r}) d^3 \mathbf{r}}{\alpha(\mathbf{r})}, \quad (\text{C.21})$$

where the variation of $\alpha(\mathbf{r})$ is relatively small, $\alpha \approx 0.18 - 0.21 \text{ ml/g}$, with a common value of $\bar{\alpha} = 0.20 \text{ ml/g}$. However, the accurate determination of volume V is very challenging, which prevents Eq. (C.21) from being widely use. A workaround was suggested by Barer by assuming that the refractive index is integrated along the axial dimension during imaging, i.e., $\Delta n(\mathbf{r}) = \Delta n(\mathbf{r}_\perp)$ to convert Eq. (C.21) into

$$m = \int_{\mathbf{r}_\perp \in S} \frac{\Delta n(\mathbf{r}_\perp) h(\mathbf{r}_\perp) d^2 \mathbf{r}_\perp}{\bar{\alpha}} = \int_{\mathbf{r}_\perp \in S} \frac{\varphi(\mathbf{r}_\perp) d^2 \mathbf{r}_\perp}{\bar{\alpha} \beta_o}, \quad (\text{C.22})$$

where $\varphi(\mathbf{r}_\perp) = \beta_o \Delta n(\mathbf{r}_\perp) h(\mathbf{r}_\perp)$, and S is the effective projected area of the cell. Unfortunately, this assumption is not applicable to optically thick samples. Here, we show how to obtain the total dry mass directly from Eq. (C.21) given that V is accurately provided by GLIM. First, we write this equation in terms of the susceptibility using the approximation $\Delta n(\mathbf{r}) \approx [(n_p^2(\mathbf{r}) - n_s^2)/(2n_s)] = [\chi(\mathbf{r})/(2n_s)]$. Eq. (C.21) yields

$$m = \frac{1}{2n_s \bar{\alpha}} \int_{\mathbf{r} \in V} \chi(\mathbf{r}) d^3 \mathbf{r} \approx \frac{\bar{\chi} V}{2n_s \bar{\alpha}}. \quad (\text{C.23})$$

In Eq. (C.23), the refractive index of the surrounding media n_s can be approximated to 1.33 [8]. To obtain the average susceptibility $\bar{\chi} = (\int \chi(\mathbf{r}) d^3 \mathbf{r} / V) \approx \tilde{\chi}^{(3)}(\mathbf{k} = 0)$, we assume that the spatial spectrum of the object is preserved through time so that $\bar{\chi}$ can be estimated using the absolute value of the filtered data, i.e. $\bar{\chi} = \gamma (\int |\chi_{hp}(\mathbf{r})| d^3 \mathbf{r} / V)$ up to a constant γ . The relative dry mass can be estimated without knowing this constant.

D.8 Time-lapse measuring results for dry mass, surface area, volume and sphericity of HeLa cells

Figure D.6 shows time-lapse rendering results of the HeLa cells in the selected FOV mentioned in the main text. Combining this FOV and others, we obtained several metrics over the cells during their development cycles.

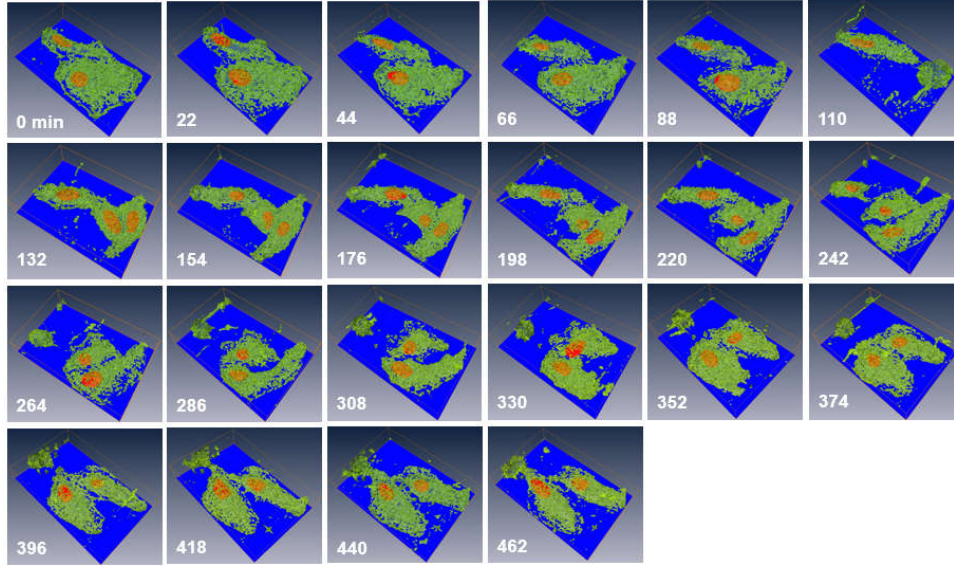


Figure D.6 Time-lapse GLIM imaging. Rendering results of the HeLa cells over time, as indicated.

Figure D.7(a) shows time-lapse measurements for absolute total dry mass (m), surface area (A), volume (V) and dry mass density (DMD= m/V) for two different FOVs. Each FOV has one parent cell and two daughter cells. The filtered data are used for automatic segmentation and dry mass extraction using procedures outlined above. The relative quantities of these metrics are computed by dividing their absolute values by those at the first time point, $t=0$ minute, and shown in Fig. D.7(b). We further display the sphericity (S), defined as $S = \pi^{1/3} (6V)^{2/3} / A$, over time. Here, we show relative metrics obtained from 17 different cells randomly selected over all FOVs. Each curve corresponds to one individual cell. Our results show that the total dry mass, volume, and surface area of all cells increase over the time during interphase. Meanwhile, the DMD is almost constant. However, when the cells enter mitosis, confirmed by maxima of the sphericity (Fig. D.7(b)), the surface area and volume reduce since the cells ball up, forming spheroids. This fact results in an increase of the dry mass density during mitosis.

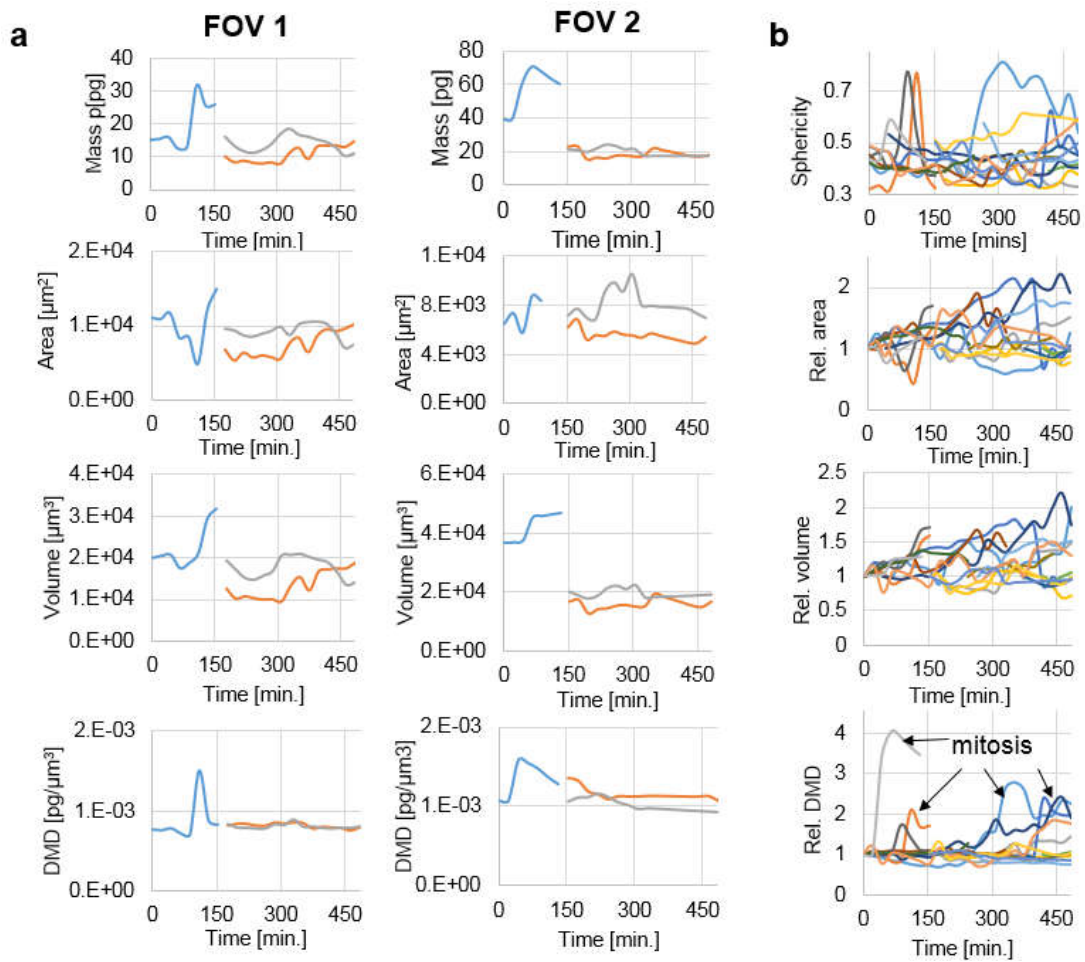


Figure D.7 Cell time-lapse measurement using GLIM. (a) Measurements of the dry mass, surface area, volume and dry mass density of 17 HeLa cells from two different FOVs. (b) Measurements of the relative dry mass, relative surface area, relative volume, sphericity and relative dry mass density of 17 HeLa cells. It can be seen that the dry mass density and sphericity increase significantly during mitosis. These time points are specified by the black arrows.

REFERENCES

- [1] J. v. Zuylen, "The microscopes of Antoni van Leeuwenhoek," *Journal of Microscopy*, vol. 121, pp. 309-328, 1981.
- [2] R. Hooke, *Micrographia or Some Physiological Descriptions of Minute Bodies*. Cosimo, Inc., 2007.
- [3] E. Abbe, "Beiträge zur Theorie des Mikroskops und der mikroskopischen Wahrnehmung," *Archiv für Mikroskopische Anatomie*, vol. 9, pp. 413-418, 1873.
- [4] F. Zernike, "Phase contrast, a new method for the microscopic observation of transparent objects," *Physica*, vol. 9, pp. 686-698, 1942.
- [5] A. Lasslett, "Principles and applications of differential interference contrast light microscopy," *Microscopy and Analysis*, vol. 20, pp. S9-S11, 2006.
- [6] D. Gabor, "A new microscopic principle," *Nature*, vol. 161, pp. 777-778, 1948.
- [7] J. W. Goodman, *Introduction to Fourier Optics*, 3rd ed. Roberts & Company Publishers, 2004.
- [8] G. Popescu, *Quantitative Phase Imaging of Cells and Tissues*. Mcgraw-Hill, 2011.
- [9] Z. Wang, L. Millet, V. Chan, H. F. Ding, M. U. Gillette, and R. Bashir, "Label-free intracellular transport measured by spatial light interference microscopy," *J. Biomed. Opt.*, vol. 16, 2011.
- [10] R. Wang, Z. Wang, J. Leigh, N. Sobh, L. Millet, and M. U. Gillette, et al., "One-dimensional deterministic transport in neurons measured by dispersion-relation phase spectroscopy," *J. Phys.: Condens. Matter*, vol. 23, 2011.
- [11] G. Popescu, Y. Park, N. Lue, C. Best-Popescu, L. Deflores, and R. R. Dasari, "Optical imaging of cell mass and growth dynamics," *Am J. Physiol. - Cell Ph.*, vol. 295, pp. 538-544, 2008.
- [12] M. Mir, Z. Wang, Z. Shen, M. Bednarz, R. Bashir, and I. Golding, et al., "Optical measurement of cycle-dependent cell growth," *Proc. Nat. Acad. Sci. U.S.A.*, vol. 108, pp. 13124-13129, 2011.
- [13] Y. Park, C. A. Best, K. Badizadegan, R. R. Dasari, M. S. Feld, T. Kuriabova, et al., "Measurement of red blood cell mechanics during morphological changes," *Proc. Natl. Acad. Sci. USA*, vol. 107, pp. 6731-6736, 2010.
- [14] G. Popescu, L. P. Deflores, J. C. Vaughan, K. Badizadegan, H. Iwai, and R. R. Dasari, et al., "Fourier phase microscopy for investigation of biological structures and dynamics," *Opt. Lett.*, vol. 29, pp. 2503-2505, 2004.
- [15] Z. Wang, D. L. Marks, P. S. Carney, L. J. Millet, M. U. Gillette, A. Mihi, et al., "Spatial light interference tomography (SLIT)," *Opt. Express*, vol. 19, pp. 19907-19918, 2011.
- [16] W. Choi, C. Fang-Yen, K. Badizadegan, S. Oh, N. Lue, R. R. Dasari, et al., "Tomographic phase microscopy," *Nat. Methods.*, vol. 4, pp. 717-719, 2007.
- [17] Z. Wang, I. S. Chun, X. Li, Z.-Y. Ong, E. Pop, L. Millet, et al., "Topography and refractometry of nanostructures using spatial light interference microscopy," *Opt. Lett.*, vol. 35, pp. 208-210, 2010.
- [18] Z. Wang, K. Tangella, A. Balla, and G. Popescu, "Tissue refractive index as marker of disease," *J. Biomed. Opt.*, vol. 16, 2011.
- [19] S. Sridharan, V. Macias, K. Tangella, A. Kajdacsy-Balla, and G. Popescu, "Prediction of Prostate Cancer Recurrence Using Quantitative Phase Imaging," *Scientific Reports*, vol. 5, 2015.
- [20] B. Bhaduri, C. Edwards, H. Pham, R. J. Zhou, T. H. Nguyen, L. L. Goddard, et al., "Diffraction phase microscopy: principles and applications in materials and life sciences," *Adv. Opt. Photonics*, vol. 6, pp. 57-119, Mar 2014.

- [21] P. Bon, G. Maucort, B. Wattellier, and S. Monneret, "Quadriwave lateral shearing interferometry for quantitative phase microscopy of living cells," *Opt. Express*, vol. 17, pp. 13080-13094, 2009.
- [22] J. Primot and N. Guérineau, "Extended Hartmann test based on the pseudoguiding property of a Hartmann mask completed by a phase chessboard," *Applied Optics*, vol. 39, pp. 5715-5720, 2000.
- [23] T. E. Gureyev and K. A. Nugent, "Rapid quantitative phase imaging using the transport of intensity equation," *Opt. Commun.*, vol. 133, pp. 339-346, 1997.
- [24] A. M. Zysk, R. W. Schoonover, P. S. Carney, and M. A. Anastasio, "Transport of intensity and spectrum for partially coherent fields," *Optics Letters*, vol. 35, pp. 2239-2241, 2010.
- [25] E. Shaffer and C. Depeursinge, "Digital holographic microscopy at fundamental and second harmonic wavelengths," in *European Conference on Biomedical Optics*, 2009.
- [26] S. Etienne, P. Nicolas, K. Jonas, and D. Christian, "Digital holographic microscopy investigation of second harmonic generated at a glass/air interface," *Optics Letters*, vol. 34, pp. 2450-2452, 2009.
- [27] P. Marquet, B. Rappaz, and N. Pavillon, "Quantitative phase - digital holographic microscopy: A new modality for live cell imaging," *New Techniques in Digital Holography*, pp. 169-217, 2015.
- [28] T. Ikeda, G. Popescu, R. R. Dasari, and M. S. Feld, "Hilbert phase microscopy for investigating fast dynamics in transparent systems," *Opt. Lett.*, vol. 30, pp. 1165-1167, 2005.
- [29] D. Zicha and G. A. Dunn, "An image-processing system for cell behavior studies in subconfluent cultures," *J. Microsc.*, vol. 179, pp. 11-21, 1995.
- [30] D. Hogenboom, C. A. DiMarzio, T. J. Gaudette, A. J. Devaney, and S. C. Lindberg, "Three-dimensional images generated by quadrature interferometry," *Opt. Lett.*, vol. 23, pp. 783-785, 1998.
- [31] G. Popescu, L. P. Deflores, J. C. Vaughan, K. Badizadegan, H. Iwai, R. R. Dasari, *et al.*, "Fourier phase microscopy for investigation of biological structures and dynamics," *Opt. Lett.*, vol. 29, pp. 2503-2505, 2004.
- [32] Z. Wang, L. J. Millet, M. Mir, H. Ding, S. Unarunotai, J. A. Rogers, *et al.*, "Spatial light interference microscopy (SLIM)," *Opt. Exp.*, vol. 19, 2011.
- [33] T. H. Nguyen and G. Popescu, "Spatial light interference microscopy (SLIM) using twisted-nematic liquid-crystal modulation," *Biomedical Optics Express*, vol. 4, pp. 1571-1583, 2013.
- [34] C. Edwards, B. Bhaduri, B. G. Griffin, L. L. Goddard, and G. Popescu, "Epi-illumination diffraction phase microscopy with white light," *Opt. Lett.*, vol. 39, pp. 6162-6165, 2014/11/01 2014.
- [35] T. H. Nguyen, C. Edwards, L. L. Goddard, and G. Popescu, "Quantitative phase imaging with partially coherent illumination," *Opt. Lett.*, vol. 39, pp. 5511-5514, 2014.
- [36] J. W. Goodman, *Speckle Phenomena in Optics: Theory and Applications*. Roberts & Co, 2007.
- [37] B. Bhaduri, H. Pham, M. Mir, and G. Popescu, "Diffraction phase microscopy with white light," *Opt. Lett.*, vol. 37, 2012.
- [38] T. H. Nguyen, C. Edwards, L. L. Goddard, and G. Popescu, "Quantitative phase imaging of weakly scattering objects using partially coherent illumination," *Optics Express*, vol. 24, pp. 11683-11693, 2016.
- [39] B. Bhaduri, H. Pham, M. Mir, and G. Popescu, "Diffraction phase microscopy with white light," *Opt. Lett.*, vol. 37, pp. 1094-1096, 2012.

- [40] B. Bhaduri, C. Edwards, H. Pham, R. Zhou, T. Nguyen, L. Goddard, *et al.*, "Diffraction phase microscopy: principles and applications in materials and life sciences," *Advances in Optics and Photonics*, 2014.
- [41] M. Young, B. Faulkner, and J. Cole, "Resolution in optical systems using coherent illumination," *JOSA*, vol. 60, pp. 137-139, 1970.
- [42] B. Bhaduri, K. Tangella, and G. Popescu, "Fourier phase microscopy with white light," *Biomed. Opt. Express*, vol. 4, pp. 1434-1441, 08/01 2013.
- [43] T. Kim, R. Zhou, M. Mir, S. D. Babacan, P. S. Carney, L. L. Goddard, *et al.*, "White-light diffraction tomography of unlabelled live cells," *Nature Photonics*, 2014.
- [44] S. Sridharan, M. Mir, and G. Popescu, "Simultaneous optical measurements of cell motility and growth," *Biomedical Optics Express*, vol. 2, pp. 2815-2820, 2011.
- [45] S. Aknoun, J. Savatier, P. Bon, F. Galland, L. Abdeladim, B. Wattellier, *et al.*, "Living cell dry mass measurement using quantitative phase imaging with quadriwave lateral shearing interferometry: an accuracy and sensitivity discussion," *Journal of Biomedical Optics*, vol. 20, pp. 126009-126009, 2015.
- [46] G. Popescu, K. Park, M. Mir, and R. Bashir, "New technologies for measuring single cell mass," *Lab on a Chip*, vol. 14, pp. 646-652, 2014.
- [47] M. Mir, A. Bergamaschi, B. S. Katzenellenbogen, and G. Popescu, "Highly sensitive quantitative imaging for monitoring single cancer cell growth kinetics and drug response," *PloS one*, vol. 9, p. e89000, 2014.
- [48] E. Ben-Isaac, Y. Park, G. Popescu, F. L. H. Brown, N. S. Gov, and Y. Shokef, "Effective temperature of red-blood-cell membrane fluctuations," *Physical Review Letters*, vol. 106, p. 238103, 2011.
- [49] Y. Park, C. A. Best, T. Kuriabova, M. L. Henle, M. S. Feld, A. J. Levine, *et al.*, "Measurement of the nonlinear elasticity of red blood cell membranes," *Physical Review E*, vol. 83, p. 051925, 2011.
- [50] Y. Park, M. Diez-Silva, G. Popescu, G. Lykotrafitis, W. Choi, M. S. Feld, *et al.*, "Refractive index maps and membrane dynamics of human red blood cells parasitized by Plasmodium falciparum," *Proceedings of the National Academy of Sciences*, vol. 105, pp. 13730-13735, 2008.
- [51] G. Popescu, Y. Park, W. Choi, R. R. Dasari, M. S. Feld, and K. Badizadegan, "Imaging red blood cell dynamics by quantitative phase microscopy," *Blood Cells, Molecules, and Diseases*, vol. 41, pp. 10-16, 2008.
- [52] H. V. Pham, B. Bhaduri, K. Tangella, C. Best-Popescu, and G. Popescu, "Real time blood testing using quantitative phase imaging," *PLoS One*, vol. 8, p. e55676, 2013.
- [53] M. Mir, K. Tangella, and G. Popescu, "Blood testing at the single cell level using quantitative phase and amplitude microscopy," *Biomedical Optics Express*, vol. 2, pp. 3259-3266, 2011.
- [54] M. Mir, T. Kim, A. Majumder, M. Xiang, R. Wang, S. C. Liu, *et al.*, "Label-free characterization of emerging human neuronal networks," *Scientific Reports*, vol. 4, 2014.
- [55] S. Ceballos, M. Kandel, S. Sridharan, H. Majeed, F. Monroy, and G. Popescu, "Active intracellular transport in metastatic cells studied by spatial light interference microscopy," *Journal of Biomedical Optics*, vol. 20, pp. 111209-111209, 2015.
- [56] R. Wang, Z. Wang, L. Millet, M. U. Gillette, A. J. Levine, and G. Popescu, "Dispersion-relation phase spectroscopy of intracellular transport," *Optics Express*, vol. 19, pp. 20571-20579, 2011.
- [57] R. Wang, L. Lei, S. Sridharan, Y. Wang, A. J. Levine, and G. Popescu, "Dispersion relations of cytoskeleton dynamics," *Cell Health and Cytoskeleton*, vol. 8, pp. 1-7, 2016.

- [58] M. Mir, S. D. Babacan, M. Bednarz, M. N. Do, I. Golding, and G. Popescu, "Visualizing Escherichia coli sub-cellular structure using sparse deconvolution spatial light interference tomography," *PLoS One*, vol. 7, p. e39816, 2012.
- [59] S. Sridharan, A. Katz, F. Soto-Adames, and G. Popescu, "Quantitative phase imaging of arthropods," *Journal of biomedical optics*, vol. 20, pp. 111212-111212, 2015.
- [60] H. Ding, F. Nguyen, S. A. Boppart, and G. Popescu, "Optical properties of tissues quantified by Fourier-transform light scattering," *Optics Letters*, vol. 34, pp. 1372-1374, 2009.
- [61] C. Edwards, S. J. McKeown, J. Zhou, G. Popescu, and L. L. Goddard, "In situ measurements of the axial expansion of palladium microdisks during hydrogen exposure using diffraction phase microscopy," *Optical Materials Express*, vol. 4, pp. 2559-2564, 2014.
- [62] C. Edwards, K. Wang, R. Zhou, B. Bhaduri, G. Popescu, and L. L. Goddard, "Digital projection photochemical etching defines gray-scale features," *Optics Express*, vol. 21, pp. 13547-13554, 2013.
- [63] C. Edwards, A. Arbabi, G. Popescu, and L. L. Goddard, "Optically monitoring and controlling nanoscale topography during semiconductor etching," *Light: Science & Applications*, vol. 1, p. e30, 2012.
- [64] C. Edwards, A. Arbabi, B. Bhaduri, X. Wang, R. Ganti, P. J. Yunker, *et al.*, "Measuring the nonuniform evaporation dynamics of sprayed sessile microdroplets with quantitative phase imaging," *Langmuir*, vol. 31, pp. 11020-11032, 2015.
- [65] R. Zhou, C. Edwards, A. Arbabi, G. Popescu, and L. L. Goddard, "Detecting 20 nm wide defects in large area nanopatterns using optical interferometric microscopy," *Nano Letters*, vol. 13, pp. 3716-3721, 2013.
- [66] H. Majeed, M. E. Kandel, K. Han, Z. Luo, V. Macias, K. Tangella, *et al.*, "Breast cancer diagnosis using spatial light interference microscopy," *Journal of Biomedical Optics*, vol. 20, pp. 111210-111210, 2015.
- [67] Y. Park, C. A. Best, and G. Popescu, "Optical sensing of red blood cell dynamics," in *Mechanobiology of Cell-cell and Cell-matrix Interactions*, ed: Springer, 2011, pp. 279-309.
- [68] H. Park, S. Lee, M. Ji, K. Kim, Y. Son, S. Jang, *et al.*, "Measuring cell surface area and deformability of individual human red blood cells over blood storage using quantitative phase imaging," *Scientific Reports*, vol. 6, 2016.
- [69] K. Kim, K. Choe, I. Park, P. Kim, and Y. Park, "Holographic intravital microscopy for 2-D and 3-D imaging intact circulating blood cells in microcapillaries of live mice," *Scientific Reports*, vol. 6, 2016.
- [70] Y. Kim, H. Shim, K. Kim, H. Park, S. Jang, and Y. Park, "Profiling individual human red blood cells using common-path diffraction optical tomography," *Scientific Reports*, vol. 4, p. 6659, 2014.
- [71] H. Byun, T. R. Hillman, J. M. Higgins, M. Diez-Silva, Z. Peng, M. Dao, *et al.*, "Optical measurement of biomechanical properties of individual erythrocytes from a sickle cell patient," *Acta Biomaterialia*, vol. 8, pp. 4130-4138, 2012.
- [72] J. Yoon, K. Lee, and Y. Park, "A simple and rapid method for detecting living microorganisms in food using laser speckle decorrelation," *arXiv preprint arXiv:1603.07343*, 2016.
- [73] L. Tian, N. Loomis, J. A. Domínguez-Caballero, and G. Barbastathis, "Quantitative measurement of size and three-dimensional position of fast-moving bubbles in air-water mixture flows using digital holography," *Applied Optics*, vol. 49, pp. 1549-1554, 2010.

- [74] S. Sridharan, V. Macias, K. Tangella, J. Melamed, E. Dube, M. X. Kong, *et al.*, "Prediction of prostate cancer recurrence using quantitative phase imaging: Validation on a general population," *Scientific Reports*, vol. 6, 2016.
- [75] D. J. Lee and A. M. Weiner, "Optical phase imaging using a synthetic aperture phase retrieval technique," *Optics Express*, vol. 22, pp. 9380-9394, 2014.
- [76] G. Dardikman, M. Habaza, L. Waller, and N. T. Shaked, "Video-rate processing in tomographic phase microscopy of biological cells using CUDA," *Optics Express*, vol. 24, pp. 11839-11854, 2016.
- [77] X. Ou, R. Horstmeyer, C. Yang, and G. Zheng, "Quantitative phase imaging via Fourier ptychographic microscopy," *Opt. Lett.*, vol. 38, pp. 4845-4848, 2013.
- [78] J. W. Goodman, "Statistical Optics," *New York, Wiley-Interscience*, vol. 1., 1985.
- [79] J. C. Petrucci, L. Tian, and G. Barbastathis, "The transport of intensity equation for optical path length recovery using partially coherent illumination," *Opt. Express*, vol. 21, pp. 14430-14441, 2013.
- [80] C. Zuo, Q. Chen, L. Tian, L. Waller, and A. Asundi, "Transport of intensity phase retrieval and computational imaging for partially coherent fields: The phase space perspective," *Opt. Laser. Eng.*, vol. 71, pp. 20-32, 2015.
- [81] C. Edwards, B. Bhaduri, T. Nguyen, B. G. Griffin, H. Pham, T. Kim, *et al.*, "Effects of spatial coherence in diffraction phase microscopy," *Opt. Express*, vol. 22, pp. 5133-5146, 2014.
- [82] D. Evanko, A. Heinrichs, and C. K. Rosenthal, "Milestones in Light Microscopy," *Nature*, May, 2011.
- [83] S. W. Hell and J. Wichmann, "Breaking the diffraction resolution limit by stimulated emission: stimulated-emission-depletion fluorescence microscopy," *Optics letters*, vol. 19, pp. 780-782, 1994.
- [84] M. Pluta, *Advanced light microscopy*. Warszawa. Polish Scientific Publishers, 1988.
- [85] A. Diaspro, *Optical Fluorescence Microscopy*. Berlin: Springer, 2011.
- [86] M. R. Eftink and C. A. Ghiron, "Fluorescence quenching studies with proteins," *Analytical Biochemistry*, vol. 114, pp. 199-227, 1981.
- [87] F. Zernike, "How I discovered phase contrast," *Science*, vol. 121, pp. 345-349, 1955.
- [88] M. Born and E. Wolf, *Principles of optics: Electromagnetic Theory of Propagation, Interference and Diffraction of Light*, 7th expanded ed. Cambridge, New York: Cambridge University Press, 1999.
- [89] S. B. Mehta and C. J. Sheppard, "Using the phase-space imager to analyze partially coherent imaging systems: bright-field, phase contrast, differential interference contrast, differential phase contrast, and spiral phase contrast," *J. Mod. Opt.*, vol. 57, pp. 718-739, 2010.
- [90] L. Mandel and E. Wolf, *Optical Coherence and Quantum Optics*. Cambridge University, 1995.
- [91] K. Li, E. D. Miller, L. E. Weiss, P. G. Campbell, and T. Kanade, "Online tracking of migrating and proliferating cells imaged with phase-contrast microscopy," in *Computer Vision and Pattern Recognition Workshop, 2006*.
- [92] K. Wu, D. Gauthier, and M. D. Levine, "Live cell image segmentation," *Biomedical Engineering, IEEE Transactions on*, vol. 42, pp. 1-12, 1995.
- [93] S. Huh, D. F. E. Ker, R. Bise, M. Chen, and T. Kanade, "Automated mitosis detection of stem cell populations in phase-contrast microscopy images," *Medical Imaging, IEEE Transactions on*, vol. 30, pp. 586-596, 2011.
- [94] T. Otaki, "Artifact halo reduction in phase contrast microscopy using apodization," *Optical Review*, vol. 7, pp. 119-122, 2000.

- [95] Z. Yin, T. Kanade, and M. Chen, "Understanding the phase contrast optics to restore artifact-free microscopy images for segmentation," *Medical Image Analysis*, vol. 16, pp. 1047-1062, 2012.
- [96] Z. Yin, K. Li, T. Kanade, and M. Chen, "Understanding the optics to aid microscopy image segmentation," in *Medical Image Computing and Computer-Assisted Intervention—MICCAI 2010*, Springer, 2010, pp. 209-217.
- [97] R. Molina, J. Mateos, and A. Katsaggelos, "Blind deconvolution using a variational approach to parameter, image, and blur Estimation," *IEEE Trans. Image Proc.*, vol. 15, 2006.
- [98] D. Babacan, M. Rafael, and K. Katsaggelos, "Variational Bayesian blind deconvolution using a total variation prior," *IEEE Trans. Image Proc.*, vol. 18, 2009.
- [99] R. H. Byrd, P. Lu, J. Nocedal, and C. Zhu, "A limited memory algorithm for bound constrained optimization," *SIAM Journal on Scientific Computing*, vol. 16, pp. 1190-1208, 1995.
- [100] C. Zhu, R. H. Byrd, P. Lu, and J. Nocedal, "Algorithm 778: L-BFGS-B: Fortran subroutines for large-scale bound-constrained optimization," *ACM Transactions on Mathematical Software (TOMS)*, vol. 23, pp. 550-560, 1997.
- [101] J. L. Morales and J. Nocedal, "Remark on Algorithm 778: L-BFGS-B: Fortran subroutines for large-scale bound constrained optimization," *ACM Transactions on Mathematical Software (TOMS)*, vol. 38, p. 7, 2011.
- [102] M. Hammer, D. Schweitzer, B. Michel, E. Thamm, and A. Kolb, "Single scattering by red blood cells," *Applied Optics*, vol. 37, pp. 7410-7418, 1998.
- [103] M. A. Lichtman, *Williams Hematology*. McGraw-Hill, Medical Pub. Division, 2006.
- [104] N. Otsu, "A threshold selection method from gray-level histograms," *Automatica*, vol. 11, pp. 23-27, 1975.
- [105] *Detecting a Cell Using Image Segmentation*. Available: <http://www.mathworks.com/help/images/examples/detecting-a-cell-using-image-segmentation.html>
- [106] R. Barer, "Interference microscopy and mass determination," *Nature*, vol. 169, pp. 366-367, 1952.
- [107] US Cancer Statistics Working Group, "United States cancer statistics: 1999–2010 incidence and mortality web-based report," Atlanta, GA, 2013.
- [108] R. L. Siegel, K. D. Miller, and A. Jemal, "Cancer statistics, 2015," *CA: A Cancer Journal for Clinicians*, vol. 65, pp. 5-29, 2015.
- [109] S. Frankel, G. D. Smith, J. Donovan, and D. Neal, "Screening for prostate cancer," *The Lancet*, vol. 361, pp. 1122-1128, 2003.
- [110] D. F. Gleason and E. M. Tannenbaum, "The veteran's administration cooperative urologic research group: Histologic grading and clinical staging of prostatic carcinoma," *Urologic Pathology: The Prostate*, pp. 171-198, 1977.
- [111] J. I. Epstein, "An update of the Gleason grading system," *The Journal of Urology*, vol. 183, pp. 433-440, 2010.
- [112] P. A. Humphrey, "Gleason grading and prognostic factors in carcinoma of the prostate," *Modern Pathology*, vol. 17, pp. 292-306, 2004.
- [113] M. S. Cookson, N. E. Fleshner, S. M. Soloway, and W. R. Fair, "Correlation between Gleason score of needle biopsy and radical prostatectomy specimen: accuracy and clinical implications," *The Journal of Urology*, vol. 157, pp. 559-562, 1997.
- [114] H. B. Carter, A. W. Partin, P. C. Walsh, B. J. Trock, R. W. Veltri, W. G. Nelson, *et al.*, "Gleason score 6 adenocarcinoma: should it be labeled as cancer?" *Journal of Clinical Oncology*, vol. 30, pp. 4294-4296, 2012.

- [115] S. Signoretti, D. Waltregny, J. Dilks, B. Isaac, D. Lin, L. Garraway, *et al.*, "p63 is a prostate basal cell marker and is required for prostate development," *The American Journal of Pathology*, vol. 157, pp. 1769-1775, 2000.
- [116] Z. Jiang, C.-L. Wu, B. A. Woda, K. Dresser, J. Xu, G. R. Fanger, *et al.*, "P504S/ α -methylacyl-CoA racemase: a useful marker for diagnosis of small foci of prostatic carcinoma on needle biopsy," *The American Journal of Surgical Pathology*, vol. 26, pp. 1169-1174, 2002.
- [117] I. L. Deras, S. M. Aubin, A. Blase, J. R. Day, S. Koo, A. W. Partin, *et al.*, "PCA3: a molecular urine assay for predicting prostate biopsy outcome," *The Journal of Urology*, vol. 179, pp. 1587-1592, 2008.
- [118] J. Diamond, N. H. Anderson, P. H. Bartels, R. Montironi, and P. W. Hamilton, "The use of morphological characteristics and texture analysis in the identification of tissue composition in prostatic neoplasia," *Human Pathology*, vol. 35, pp. 1121-1131, 2004.
- [119] R. Farjam, H. Soltanian-Zadeh, R. A. Zoroofi, and K. Jafari-Khouzani, "Tree-structured grading of pathological images of prostate," in *Medical Imaging*, 2005, pp. 840-851.
- [120] S. Naik, S. Doyle, M. Feldman, J. Tomaszewski, and A. Madabhushi, "Gland segmentation and computerized gleason grading of prostate histology by integrating low-, high-level and domain specific information," in *MIAAB Workshop*, 2007.
- [121] K. Nguyen, B. Sabata, and A. K. Jain, "Prostate cancer grading: Gland segmentation and structural features," *Pattern Recognition Letters*, vol. 33, pp. 951-961, 2012.
- [122] M. N. Gurcan, L. E. Boucheron, A. Can, A. Madabhushi, N. M. Rajpoot, and B. Yener, "Histopathological image analysis: a review," *Biomedical Engineering, IEEE Reviews in*, vol. 2, pp. 147-171, 2009.
- [123] B. G. Muller, D. M. Bruin, M. J. Brandt, W. Bos, S. Huystee, D. Faber, *et al.*, "Prostate cancer diagnosis by optical coherence tomography: First results from a needle based optical platform for tissue sampling," *Journal of biophotonics*, 2016.
- [124] S. Uttam, H. V. Pham, J. LaFace, B. Leibowitz, J. Yu, R. E. Brand, *et al.*, "Early prediction of cancer progression by depth-resolved nanoscale mapping of nuclear architecture from unstained tissue specimens," *Cancer Research*, vol. 75, pp. 4718-4727, 2015.
- [125] P. Crow, N. Stone, C. Kendall, J. Uff, J. Farmer, H. Barr, *et al.*, "The use of Raman spectroscopy to identify and grade prostatic adenocarcinoma in vitro," *British Journal of Cancer*, vol. 89, pp. 106-108, 2003.
- [126] J. T. Kwak, S. M. Hewitt, S. Sinha, and R. Bhargava, "Multimodal microscopy for automated histologic analysis of prostate cancer," *BMC Cancer*, vol. 11, p. 62, 2011.
- [127] J. T. Kwak, A. Kajdacsy-Balla, V. Macias, M. Walsh, S. Sinha, and R. Bhargava, "Improving Prediction of Prostate Cancer Recurrence using Chemical Imaging," *Scientific Reports*, vol. 5, 2015.
- [128] G. Popescu, T. Ikeda, R. R. Dasari, and M. S. Feld, "Diffraction phase microscopy for quantifying cell structure and dynamics," *Opt. Lett.*, vol. 31, pp. 775-777, 2006.
- [129] E. Cuche, F. Bevilacqua, and C. Depeursinge, "Digital holography for quantitative phase-contrast imaging," *Opt. Lett.*, vol. 24, pp. 291-293, 1999.
- [130] S. Sridharan, V. Macias, K. Tangella, A. Kajdacsy-Balla, and G. Popescu, "Prediction of prostate cancer recurrence using quantitative phase imaging," *Sci Rep*, vol. 5, p. 9976, 2015.
- [131] B. Julesz, "Textons, the elements of texture perception, and their interactions," *Nature*, 1981.
- [132] T. Leung and J. Malik, "Recognizing surfaces using three-dimensional textons," presented at the Seventh IEEE International Conference on Computer Vision, 1999.

- [133] T. Leung and J. Malik, "Representing and recognizing the visual appearance of materials using three-dimensional textons," *International Journal of Computer Vision*, vol. 43, pp. 29-44, 2001.
- [134] J. Shotton, M. Johnson, and R. Cipolla, "Semantic texton forests for image categorization and segmentation," presented at the IEEE Conference on Computer Vision and Pattern Recognition, 2008.
- [135] J. Shotton, J. Winn, C. Rother, and A. Criminisi, "TextonBoost for image understanding: multi-class object recognition and segmentation by jointly modeling texture, layout, and context," *International Journal of Computer Vision*, vol. 81, pp. 2-23, 2009.
- [136] J. Malik and P. Perona, "Preattentive texture discrimination with early vision mechanisms," *JOSA A*, vol. 7, pp. 923-932, 1990.
- [137] J. Malik, S. Belongie, T. Leung, and J. Shi, "Contour and texture analysis for image segmentation," *International Journal of Computer Vision*, vol. 43, pp. 7-27, 2001.
- [138] L. Breiman, "Random forests," *Machine Learning*, vol. 45, pp. 5-32, 2001.
- [139] J. Shotton, A. Fitzgibbon, M. Cook, T. Sharp, M. Finocchio, R. Moore, *et al.*, "Real-time human pose recognition in parts from single depth images," presented at the IEEE Computer Vision and Pattern Recognition (CVPR), 2011.
- [140] L. Breiman, "Bagging Predictors," *Machine Learning*, vol. 24, pp. 123-140, 1996.
- [141] T. Hastie, R. Tibshirani, and J. Friedman, *The Elements of Statistical Learning: Data Mining, Inference, and Prediction*, Second ed. Springer, 2009.
- [142] W. C. Allsbrook, K. A. Mangold, M. H. Johnson, R. B. Lane, C. G. Lane, and J. I. Epstein, "Interobserver reproducibility of Gleason grading of prostatic carcinoma: general pathologist," *Human Pathology*, vol. 32, pp. 81-88, 2001.
- [143] M. B. Amin, D. Grignon, P. A. Humphrey, and J. R. Srigley, *Gleason Grading of Prostate Cancer: A Contemporary Approach*. New York. Lippincott Williams & Wilkins, 2003.
- [144] J. Friedman, T. Hastie, and R. Tibshirani, "Regularization paths for generalized linear models via coordinate descent," *Journal of Statistical Software*, vol. 33, p. 1, 2010.
- [145] K. M. Yamada and E. Cukierman, "Modeling tissue morphogenesis and cancer in 3D," *Cell*, vol. 130, pp. 601-610, 2007.
- [146] F. Pampaloni, E. G. Reynaud, and E. H. Stelzer, "The third dimension bridges the gap between cell culture and live tissue," *Nature Reviews Molecular Cell Biology*, vol. 8, pp. 839-845, 2007.
- [147] S. W. Hell, "Far-field optical nanoscopy," *Science*, vol. 316, pp. 1153-1158, May 25 2007.
- [148] J. Lippincott-Schwartz, N. Altan-Bonnet, and G. H. Patterson, "Photobleaching and photoactivation: following protein dynamics in living cells," *Nature Cell Biology*, p. S7, 2003.
- [149] R. A. Hoebe, C. H. Van Oven, T. W. Gadella, Jr., P. B. Dhonukshe, C. J. F. Van Noorden, and E. M. M. Manders, "Controlled light-exposure microscopy reduces photobleaching and phototoxicity in fluorescence live-cell imaging," *Nature Biotechnology*, vol. 25, pp. 249-253, 2007.
- [150] R. Y. Tsien, "The green fluorescent protein," *Annual Review of Biochemistry*, vol. 67, pp. 509-544, 1998.
- [151] G. Crivat and J. W. Taraska, "Imaging proteins inside cells with fluorescent tags," *Trends in biotechnology*, vol. 30, pp. 8-16, 2012.
- [152] B. W. Graf and S. A. Boppart, "Imaging and analysis of three-dimensional cell culture models," *Live Cell Imaging: Methods and Protocols*, pp. 211-227, 2010.

- [153] A. J. North, "Seeing is believing? A beginners' guide to practical pitfalls in image acquisition," *The Journal of Cell Biology*, vol. 172, pp. 9-18, 2006.
- [154] J. B. Pawley, *Handbook of Biological Confocal Microscopy*, 3rd ed. New York. Springer, 2006.
- [155] B. R. Masters and P. T. C. So, *Handbook of Biomedical Nonlinear Optical Microscopy*. New York. Oxford University Press, 2008.
- [156] T. A. Planchon, L. Gao, D. E. Milkie, M. W. Davidson, J. A. Galbraith, C. G. Galbraith, *et al.*, "Rapid three-dimensional isotropic imaging of living cells using Bessel beam plane illumination," *Nature Methods*, vol. 8, pp. 417-423, 2011.
- [157] B. C. Chen, W. R. Legant, K. Wang, L. Shao, D. E. Milkie, M. W. Davidson, *et al.*, "Lattice light-sheet microscopy: Imaging molecules to embryos at high spatiotemporal resolution," *Science*, vol. 346, pp. 439-+, Oct 24 2014.
- [158] P. J. Keller, A. D. Schmidt, J. Wittbrodt, and E. H. K. Stelzer, "Reconstruction of zebrafish early embryonic development by scanned light sheet microscopy," *Science*, vol. 322, pp. 1065-1069, Nov 14 2008.
- [159] D. Way, "Principles and applications of differential interference contrast light microscopy," *Microscopy and Analysis; Light Microscopy Supplement*, vol. 20, pp. 9-11, 2006.
- [160] B. Bhaduri, C. Edwards, H. Pham, R. Zhou, T. H. Nguyen, L. L. Goddard, *et al.*, "Diffraction phase microscopy: principles and applications in materials and life sciences," *Advances in Optics and Photonics*, vol. 6, pp. 57-119, 2014/03/31 2014.
- [161] G. Popescu, T. Ikeda, R. R. Dasari, and M. S. Feld, "Diffraction phase microscopy for quantifying cell structure and dynamics," *Opt Lett*, vol. 31, pp. 775-777, 2006.
- [162] Z. Wang, L. J. Millet, M. Mir, H. Ding, S. Unarunotai, J. A. Rogers, *et al.*, "Spatial light interference microscopy (SLIM)," *Optics Express*, vol. 19, p. 1016, 2011.
- [163] Z. Wang, D. L. Marks, P. S. Carney, L. J. Millet, M. U. Gillette, A. Mihi, *et al.*, "Spatial light interference tomography (SLIT)," *Optics Express*, vol. 19, pp. 19907-19918, 2011.
- [164] H. F. Ding, Z. Wang, F. Nguyen, S. A. Boppart, and G. Popescu, "Fourier transform light scattering of inhomogeneous and dynamic structures," *Physical Review Letters*, vol. 101, p. 238102, Dec 5 2008.
- [165] S. P. Davis, M. C. Abrams, and J. W. Brault, *Fourier Transform Spectrometry*. San Diego. Academic Press, 2001.
- [166] T. Kim, R. Zhou, L. L. Goddard, and G. Popescu, "Solving inverse scattering problems in biological samples by quantitative phase imaging," *Laser & Photonics Reviews*, vol. 10, pp. 13-39, 2016.
- [167] W. Choi, C. Fang-Yen, K. Badizadegan, S. Oh, N. Lue, R. R. Dasari, *et al.*, "Tomographic phase microscopy," *Nature Methods*, vol. 4, pp. 717-719, Sep 2007.
- [168] F. Charriere, N. Pavillon, T. Colomb, C. Depeursinge, T. J. Heger, E. A. D. Mitchell, *et al.*, "Living specimen tomography by digital holographic microscopy: morphometry of testate amoeba," *Optics Express*, vol. 14, pp. 7005-7013, Aug 7 2006.
- [169] T. Kim, R. J. Zhou, M. Mir, S. D. Babacan, P. S. Carney, L. L. Goddard, *et al.*, "White-light diffraction tomography of unlabeled live cells," *Nature Photonics*, vol. 8, pp. 256-263, Mar 2014.
- [170] T. S. Ralston, D. L. Marks, P. S. Carney, and S. A. Boppart, "Interferometric synthetic aperture microscopy," *Nature Physics*, vol. 3, pp. 129-134, Feb 2007.
- [171] Y.-W. Heng and C.-G. Koh, "Actin cytoskeleton dynamics and the cell division cycle," *The international journal of biochemistry & cell biology*, vol. 42, pp. 1622-1633, 2010.

- [172] Centers for Disease Control and Prevention. (2013). *ART Success Rates*. Available: <http://www.cdc.gov/art/reports/index.html>
- [173] J. Graham, T. Han, R. Porter, M. Levy, R. Stillman, and M. J. Tucker, "Day 3 morphology is a poor predictor of blastocyst quality in extended culture," *Fertil Steril*, vol. 74, pp. 495-7, Sep 2000.
- [174] F. Guerif, A. Le Gouge, B. Giraudeau, J. Poindron, R. Bidault, O. Gasnier, *et al.*, "Limited value of morphological assessment at days 1 and 2 to predict blastocyst development potential: a prospective study based on 4042 embryos," *Human Reproduction* vol. 22, pp. 1973-81, Jul 2007.
- [175] P. M. Rijnders and C. A. Jansen, "The predictive value of day 3 embryo morphology regarding blastocyst formation, pregnancy and implantation rate after day 5 transfer following in-vitro fertilization or intracytoplasmic sperm injection," *Hum Reprod*, vol. 13, pp. 2869-73, Oct 1998.
- [176] F. C. Marhuenda-Egea, E. Martinez-Sabater, R. Gonsalvez-Alvarez, B. Lledo, J. Ten, and R. Bernabeu, "A crucial step in assisted reproduction technology: human embryo selection using metabolomic evaluation," *Fertil Steril*, vol. 94, pp. 772-4, Jul 2010.
- [177] D. Sakkas and D. K. Gardner, "Noninvasive methods to assess embryo quality," *Curr Opin Obstet Gynecol*, vol. 17, pp. 283-8, Jun 2005.
- [178] R. Scott, E. Seli, K. Miller, D. Sakkas, K. Scott, and D. H. Burns, "Noninvasive metabolomic profiling of human embryo culture media using Raman spectroscopy predicts embryonic reproductive potential: a prospective blinded pilot study," *Fertil Steril*, vol. 90, pp. 77-83, Jul 2008.
- [179] E. Seli, L. Botros, D. Sakkas, and D. H. Burns, "Noninvasive metabolomic profiling of embryo culture media using proton nuclear magnetic resonance correlates with reproductive potential of embryos in women undergoing in vitro fertilization," *Fertil Steril*, vol. 90, pp. 2183-9, Dec 2008.
- [180] C. G. Vergouw, L. L. Botros, P. Roos, J. W. Lens, R. Schats, P. G. Hompes, *et al.*, "Metabolomic profiling by near-infrared spectroscopy as a tool to assess embryo viability: a novel, non-invasive method for embryo selection," *Hum Reprod*, vol. 23, pp. 1499-504, Jul 2008.
- [181] M. G. Katz-Jaffe, S. McReynolds, D. K. Gardner, and W. B. Schoolcraft, "The role of proteomics in defining the human embryonic secretome," *Mol Hum Reprod*, vol. 15, pp. 271-7, May 2009.
- [182] R. Weinerman, R. Feng, T. S. Ord, R. M. Schultz, M. S. Bartolomei, C. Coutifaris, *et al.*, "Morphokinetic evaluation of embryo development in a mouse model: functional and molecular correlates," *Biology of Reproduction*, Feb 24 2016.
- [183] I. Halvaei, M. A. Khalili, and S. A. Nottola, "A novel method for transmission electron microscopy study of cytoplasmic fragments from preimplantation human embryos," *Microscopy Research and Technique*, Mar 26 2016.
- [184] D. Gabor, "Microscopy by reconstructed wave-fronts," in *Proceedings of the Royal Society of London A: Mathematical, Physical and Engineering Sciences*, 1949, pp. 454-487.
- [185] N. Streibl, "Three-dimensional imaging by a microscope," *JOSA A*, vol. 2, pp. 121-127, 1985.
- [186] M. Born and E. Wolf, *Principles of Optics: Electromagnetic Theory of Propagation, Interference and Diffraction of light*. CUP Archive, 1999.
- [187] C. J. Sheppard and S. B. Mehta, "Phase space analysis of partially coherent imaging in a microscope," in *Frontiers in Optics*, 2012, p. FTu2E. 1.
- [188] F. Schroff, A. Criminisi, and A. Zisserman, "Object class segmentation using random forests," presented at the BMVC, 2008.

- [189] B. Glocker, O. Pauly, E. Konukoglu, and A. Criminisi, "Joint classification-regression forests for spatially structured multi-object segmentation," in *Computer Vision–ECCV 2012*, ed: Springer, 2012, pp. 870-881.
- [190] J. Shotton, A. Fitzgibbon, M. Cook, T. Sharp, M. Finocchio, R. Moore, *et al.*, "Real-time human pose recognition in parts from single depth images," *IEEE Computer Vision and Pattern Recognition (CVPR)*, 2011.
- [191] M. Sun, P. Kohli, and J. Shotton, "Conditional regression forests for human pose estimation," in *Computer Vision and Pattern Recognition (CVPR), 2012 IEEE Conference on*, 2012, pp. 3394-3401.
- [192] A. Criminisi, D. Robertson, E. Konukoglu, J. Shotton, S. Pathak, S. White, *et al.*, "Regression forests for efficient anatomy detection and localization in computed tomography scans," *Medical Image Analysis*, vol. 17, pp. 1293-1303, 2013.
- [193] D. Zikic, B. Glocker, E. Konukoglu, A. Criminisi, C. Demiralp, J. Shotton, *et al.*, "Decision forests for tissue-specific segmentation of high-grade gliomas in multi-channel MR," in *Medical Image Computing and Computer-Assisted Intervention–MICCAI 2012*, ed: Springer, 2012, pp. 369-376.
- [194] A. Criminisi and J. Shotton, *Decision Forests for Computer Vision and Medical Image Analysis*. Springer, 2013.
- [195] P. Geurts, D. Ernst, and L. Wehenkel, "Extremely randomized trees," *Machine Learning*, vol. 63, pp. 3-42, 2006.
- [196] L. Vincent and P. Soille, "Watersheds in digital spaces: an efficient algorithm based on immersion simulations," *IEEE Transactions on Pattern Analysis & Machine Intelligence*, pp. 583-598, 1991.
- [197] J. A. Tuxhorn, G. E. Ayala, M. J. Smith, V. C. Smith, T. D. Dang, and D. R. Rowley, "Reactive stroma in human prostate cancer induction of myofibroblast phenotype and extracellular matrix remodeling," *Clinical Cancer Research*, vol. 8, pp. 2912-2923, 2002.
- [198] D. A. Barron and D. R. Rowley, "The reactive stroma microenvironment and prostate cancer progression," *Endocrine-Related Cancer*, vol. 19, pp. R187-R204, 2012.
- [199] Z. Wang, H. Ding, and G. Popescu, "Scattering-phase theorem," *Optics Letters*, vol. 36, pp. 1215-1217, 2011.
- [200] Y. Sung, W. Choi, C. Fang-Yen, K. Badizadegan, R. R. Dasari, and M. S. Feld, "Optical diffraction tomography for high resolution live cell imaging," *Optics Express*, vol. 17, pp. 266-277, 2009.
- [201] J. W. Su, W. C. Hsu, C. Y. Chou, C. H. Chang, and K. B. Sung, "Digital holographic microtomography for high - resolution refractive index mapping of live cells," *Journal of Biophotonics*, vol. 6, pp. 416-424, 2013.
- [202] Y. Sung and R. R. Dasari, "Deterministic regularization of three-dimensional optical diffraction tomography," *JOSA A*, vol. 28, pp. 1554-1561, 2011.
- [203] R. C. Gonzalez, R. E. Woods, and S. L. Eddins, *Digital image processing using MATLAB*. 2004.
- [204] C. Tomasi and R. Manduchi, "Bilateral filtering for gray and color images," in *Computer Vision, 1998. Sixth International Conference on*, 1998, pp. 839-846.